Unearthing the Antibacterial Activity of a Natural Clay Deposit

by

Keith D. Morrison

A Dissertation Presented in Partial Fulfillment
of the Requirements for the Degree
Doctor of Philosophy

Approved June 2015 by the
Graduate Supervisory Committee:

Lynda Williams, Co-Chair
Stanley Williams, Co-Chair
Rajeev Misra
Everett Shock
Ariel Anbar

ARIZONA STATE UNIVERSITY

December 2015

ABSTRACT

The discovery and development of novel antibacterial agents is essential to address the rising health concern over antibiotic resistant bacteria. This research investigated the antibacterial activity of a natural clay deposit near Crater Lake, Oregon, that is effective at killing antibiotic resistant human pathogens. The primary rock types in the deposit are andesitic pyroclastic materials, which have been hydrothermally altered into argillic clay zones. High-sulfidation (acidic) alteration produced clay zones with elevated pyrite (18%), illite-smectite (I-S) (70% illite), elemental sulfur, kaolinite and carbonates. Low-sulfidation alteration at neutral pH generated clay zones with lower pyrite concentrations pyrite (4-6%), the mixed-layered I-S clay rectorite (R1, I-S) and quartz.

Antibacterial susceptibility testing reveals that hydrated clays containing pyrite and I-S are effective at killing (100%) of the model pathogens tested (*E. coli* and *S. epidermidis*) when pH (< 4.2) and Eh (> 450 mV) promote pyrite oxidation and mineral dissolution, releasing > 1 mM concentrations of Fe^{2+}, Fe^{3+} and Al^{3+}. However, certain oxidized clay zones containing no pyrite still inhibited bacterial growth. These clays buffered solutions to low pH (< 4.7) and oxidizing Eh (> 400 mV) conditions, releasing lower amounts (< 1 mM) of Fe and Al. The presence of carbonate in the clays eliminated antibacterial activity due to increases in pH, which lower pyrite oxidation and mineral dissolution rates.

The antibacterial mechanism of these natural clays was explored using metal toxicity and genetic assays, along with advanced bioimaging techniques. Antibacterial clays provide a continuous reservoir of Fe^{2+}, Fe^{3+} and Al^{3+} that synergistically attack

pathogens while generating hydrogen peroxide (H_2O_2). Results show that dissolved Fe^{2+} and Al^{3+} are adsorbed to bacterial envelopes, causing protein misfolding and oxidation in the outer membrane. Only Fe^{2+} is taken up by the cells, generating oxidative stress that damages DNA and proteins. Excess Fe^{2+} oxidizes inside the cell and precipitates Fe^{3+}-oxides, marking the sites of hydroxyl radical (•OH) generation. Recognition of this novel geochemical antibacterial process should inform designs of new mineral based antibacterial agents and could provide a new economic industry for such clays.

ACKNOWLEDGMENTS

The work that I have presented in my dissertation all stems from Dr. Lynda Williams pioneering work on antibacterial clays that truly embraces interdisciplinary research. I met with Lynda at a Clay Minerals Society conference and instantly knew I wanted to be a part of her research. Throughout my Ph.D. experience Lynda has focused my uncultivated research interests, while giving me the freedom and confidence to pursue my own research endeavors. Lynda always took time out of her schedule to help work through problems in my research and writing, helping me truly understand the ramifications scientific research can have. I will be forever grateful for the skills I have gained working with Lynda, and like her, I hope to pursue ground breaking interdisciplinary research throughout my career.

Field work represented a significant portion of my research, where I was challenged with the task of characterizing antibacterial mineral zones in a complex hydrothermal setting. Dr. Stan Williams worked with me in the field, patiently helping me characterize the alteration settings that formed the antibacterial clay zones. Stan's advice and expertise in the field were fundamental to my success. I would also like to thank Doug Hamilton, Laurel Hamilton and Ray Huckaba for supporting my field work and allowing me to access the deposit.

A pivotal transition in my Ph.D. studies occurred when I began working in Dr. Rajeev Misra's microbiology lab. Rajeev has greatly improved my work ethic and provides a constant source of enthusiasm for research. He freely opened his lab to facilitate much of my work and truly embraced the interdisciplinary nature of this research. Rajeev takes time to help his students on a daily basis, giving them invaluable

research training and skills. My experience was no different, with Rajeev guiding me through many complex analytical challenges. The skills I have learned in Rajeev's lab have been invaluable to my Ph.D. and I truly thank him for this.

The other faculty members on my Ph.D. committee (Everett Shock and Ariel Anbar) have provided valuable input that has helped me communicate my research to a broad audience. I would like to thank Everett Shock for taking the time to walk me through many thermodynamic calculations that have provided context to my findings. I appreciate Ariel Anbar's help in communicating my research ideas, which will help me concisely explain ideas to a broad audience.

Others who enriched my experiences during my Ph.D. include; Steven Romaniello, Greg Brennecka, Gwyneth Gordon, Amisha Poret-Peterson, Rick Hervig, David Lowry, Robert Roberson, Denis Eberl, Jennifer Underwood, David Metge, Carolina Londono, Ryan and Krista Hutchison, Danny Foley, Sarah Robinson, Cameron Mercer, Andy Ryan and Caren Burgermeister. My experiences with each of these people have been invaluable to my success as a graduate student. I am very grateful for the instruction I received from Tolek Tyliszczak at the Advanced Light Source Synchrotron, Berkeley, CA and STXM sample preparation advice/spectra from Adam Hitchcock. I would especially like to thank Gwyneth Gordon for participating in my Ph.D. defense and providing me with excellent ICP-MS data. Additionally, I would like to thank The Clay Minerals Society, The Geological Society of America and Achievement Rewards for College Scientists for their recognition and funding of my research.

My family has been a constant source of support through my academic endeavors. My parents Dave and Colleen Morrison never doubted my abilities throughout this

journey and I will be forever grateful for this. They have watched me transition through many phases in my life and I am glad that I continue to make them proud. My trips home to visit my sister Madeline's family have always brought me joy and eased my stress. My brother in law Ernie and his family have always welcomed me into their homes with open arms and I am grateful they are part of my family. I have always looked up to my sister Madeline and her strength and determination have definitely rubbed off on me. My niece's and nephew (Gwen, Emiko and Ronin) have allowed me to be a kid at heart and place many of life's challenges into perspective during my Ph.D. I am very thankful to have such a great family and friends who have helped me in this achievement.

TABLE OF CONTENTS

Page

CHAPTER Page

CHAPTER Page

APPENDIX Page

LIST OF TABLES

Table Page

LIST OF FIGURES

Figure Page

Chapter 1

THE DISCOVERY OF ANTIBACTERIAL CLAYS

1.1 Introduction to the Study of Antibacterial Minerals

Emergence of antibiotic-resistant strains of bacteria presents a global human health crisis. Traditional antibiotics are organic molecules that inhibit DNA replication, protein and cell wall synthesis (Walsh, 2000) and many pathogens (e.g., Methicillin-resistant *Staphylococcus aureus*; MRSA) subsequently develop robust antibacterial resistance mechanisms. As a result, alternative therapies against bacterial infections have gained attention. Clay minerals, although used for medicinal purposes throughout millennia, have remained largely unstudied for their applications and reported medical benefits (Carretaro, 2002; Ferrell, 2008). Recent evidence reveals that certain clay mineral deposits that release soluble transition metals (when applied hydrated) have the ability to kill pathogenic bacteria growing in chronic skin infections (Brunet de Courrsou, 2002, Williams et al., 2004; 2008). The use of metals as antimicrobial agents is growing in popularity (Lemire et al., 2013), however antibacterial mechanisms involving minerals and metal release have only recently been studied (Williams and Haydel, 2010; Williams et al., 2011). Understanding the geochemical processes that drive antibacterial clays is key to discovering new antibacterial mineral and metal compounds. All known antibacterial clays are from altered volcanic sources (volcanic ash and hydrothermally altered pyroclastics) and include an assemblage of minerals that vary depending on the geologic environment.

Clays are defined as the < 2 μm size fraction of minerals in a rock or sediment (Moore and Reynolds, 1997). Many non-clay minerals are found in this size range, but

clay minerals that are alteration or weathering products of igneous and metamorphic rocks often dominate. The most commonly used minerals for healing are in the smectite group of phyllosilicates (Fig. 1.1). Smectite can form by alteration of volcanic ash (glass that forms as magma is rapidly quenched), and many varieties of smectite form as hydrothermal fluids percolate through volcanic rock, dissolving unstable phases (e.g., feldspars) and precipitating new, stable clay minerals. Smectite has a sheet-like structure with expandable regions between the silicate sheets (interlayers) where water, organics and cations are held by weak Van der Waals forces (Moore and Reynolds, 1997). The phyllosilicate surfaces provide a vast surface area for uptake of chemical compounds from the hydrothermal fluids responsible for the clay formation. Because of this, we have examined the elements in the antibacterial clays that are easily 'exchangeable' due to relatively weak bonds that hold them in the clay interlayer, compared to elements that are in the silicate framework and only released when the mineral dissolves.

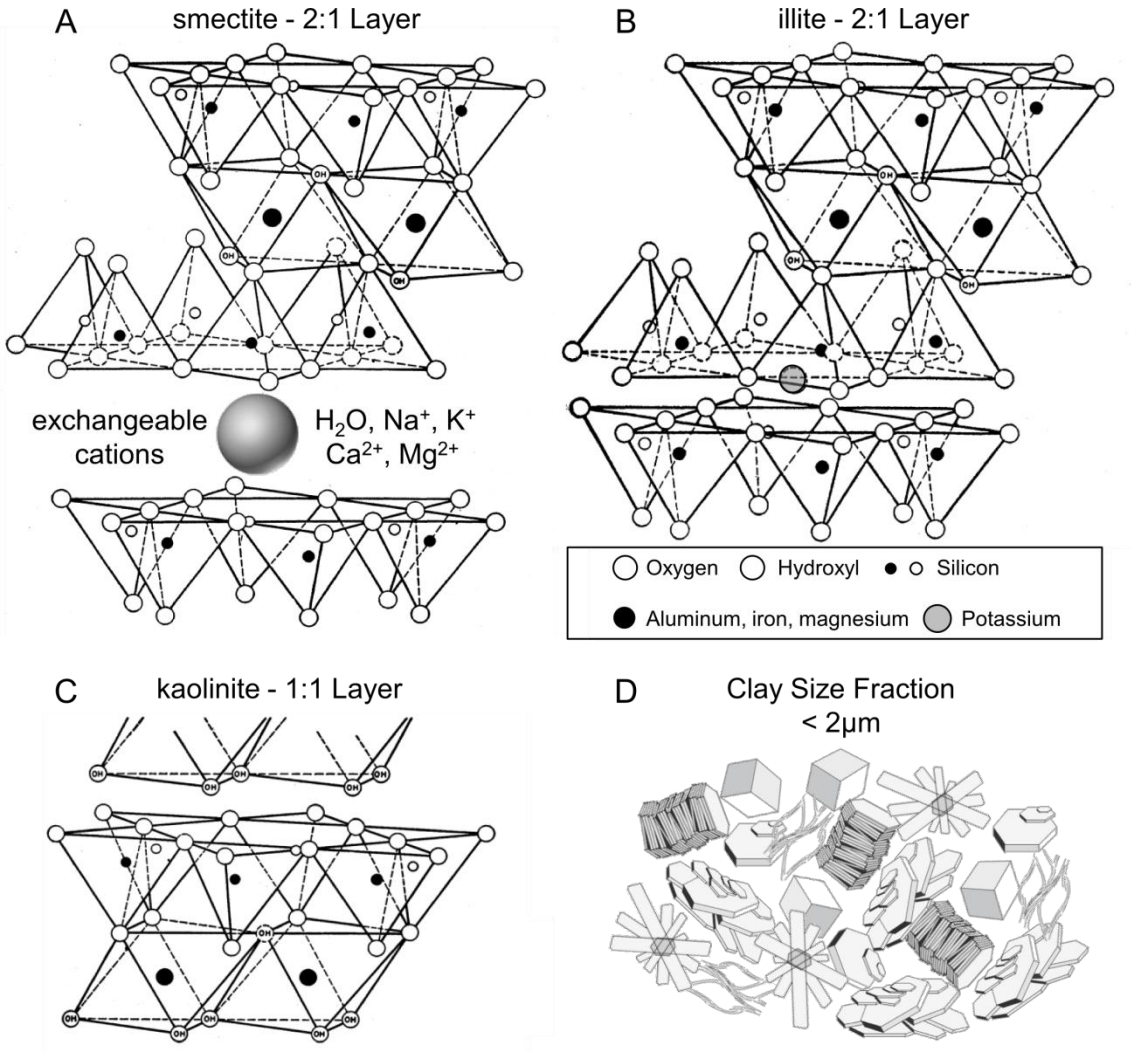

Figure 1.1 Clay mineral structures. Illustrations of common clay mineral crystal lattice structures, showing the alternating tetrahedral and octahedral layers of clay minerals (2:1 or 1:1 tetrahedral to octahedral layers). (A) 2:1 smectites with expandable interlayer spaces that exchange cations, water and organics. (B) 2:1 illite structure showing the interlayer collapsed around a potassium cation. (C) Non-expandable 1:1 kaolinite. (D) Representation of the clay size fraction (< 2 μm) in geologic samples, which contains a complex mixture of mineral phases, in addition to discrete clay minerals.

During the past 25 years, approximately 70% of newly discovered drugs introduced in the U.S. have been derived from natural products (Newman and Cragg, 2007). Medicinal and therapeutic uses of clay minerals have been documented for thousands of years (Carretaro, 2002). Early research focused on the extraordinary absorptive and adsorptive properties of clay minerals and the health benefits recognized in aiding digestive processes and cleansing and protecting the skin (Carretaro, 2002). Despite the clear beneficial effects on human health related to ridding the body of infectious agents, few studies have investigated the antibacterial properties of clay minerals (Williams et al., 2004; 2008; 2011).

1.2 French Green Clays and Mycobacterium

Previous studies of French green clays demonstrated highly effective antibacterial properties that were successfully used in treating *Mycobacterium ulcerans*, the causative pathogen of Buruli ulcers (Williams et al., 2004, 2008). Treatment with daily applications of hydrated clay poultices healed infection over the course of 3 months or more, by daily applications (Brunet de Courssou, 2002). These clays demonstrated a unique capacity to kill bacteria while promoting skin cell growth (Brunet de Courssou, 2002; Williams et al., 2004; 2008). Aqueous leachates of French green clays (deionized water shaken with minerals for 24 hours) were also antibacterial. The leachate exhibited alkaline pH $\geq$ 9.8 when prepared at a ratio of 50 mg clay/ml water then centrifuged to remove minerals. Unfortunately, the source of the French green clay minerals became depleted and subsequent testing of newer samples showed no bactericidal effect.

The supplier of the French green clay, which Brunet de Courssou used to treat Buruli ulcer patients (Williams et al., 2004), disclosed its source near the Massif Central in France, a volcanic center that produced extensive deposits of altered volcanic ash (bentonite). However, their subsequent samples showed no antibacterial effect when tested in our laboratory. This suggested that the deposit is either chemically inhomogeneous or the pH, Eh conditions are variable, affecting the antibacterial susceptibility (Williams et al., 2008). The variable degree of antibacterial effectiveness of the French clays against *M. ulcerans* highlights the need for a better understanding of the environmental controls on the mineralogy and geochemistry of natural antibacterial clays. Antibacterial testing of clays from around the world led to the identification of an antibacterial clay deposit in the United States that was relatively undisturbed by mining and therefore representative of the original geologic environment.

1.3 Oregon Hydrothermal Clay Deposit

Research on the French green clays garnered the pursuit of new antibacterial deposits, and identification of several clays that displayed antibacterial properties against a broad spectrum of human pathogens, including antibiotic resistant strains (Cunningham et al., 2010; Williams and Haydel, 2010; Williams et al., 2011). To date, the most effective antibacterial clays studied originate from hydrothermally-altered regions near Crater Lake, Oregon, USA; marketed by Oregon Mineral Technologies (OMT). Antibacterial clays from the OMT deposit killed a broad spectrum of bacteria, including methicillin resistant *S. aureus* (MRSA) and extended spectrum beta lactamase resistant *E. coli* (ESBL) (Cunningham et al., 2010; sample CB07). Unlike the previously studied

French green clays, all the antibacterial mineral suspensions examined from OMT have low pH (< 5). Williams et al., (2011) indicated iron uptake by *E. coli* cells upon reaction with OMT leachates. They first proposed that the chemical interaction between the clay leachates and the bacteria led to bactericide. Bacterial iron assimilation occurred along with the formation of large cytoplasmic voids and hypothesized intracellular Fe^{3+} precipitation upon cell death (Williams et al., 2011). Additionally, they proposed that the clay minerals buffer the pH and oxidation state to promote Fe^{2+} solubility thereby initiating a chemical attack, while generating reactive oxygen species (ROS) via the Fenton reaction. However, the redox state of the Fe and ROS production were never directly measured. Following this study, it was clear that more work was needed to evaluate how clays that differed in mineralogy, leachate chemistry, pH buffering capacity and redox state affected the bactericide.

1.4 Research Objectives

The primary goal of this research is to delineate the scientific basis by which natural clay minerals are able to kill pathogenic bacteria. By examining the mineralogical variables that correlate with the antibacterial effectiveness, we identify which mineral phase(s), out of the many minerals contained in each clay sample, control(s) the antibacterial process. Furthermore, understanding the environmental factors that created the antibacterial clays will allow recognition of new resources worldwide, where similar geologic settings exist.

This research focuses on identification of the specific bactericidal mineral reactants, evaluation of the antibacterial mechanism of action, and imaging the chemical

exchange between minerals and microbes. The combined microbial, geochemical and mineralogical approaches allow us to evaluate the biological functions that are affected by antibacterial clays, perhaps leading to new mineral based antimicrobial compounds for controlling antibiotic-resistant infections for which there are no known therapeutic agents. The results could have broad-reaching applications in topical antimicrobial dressings, wound care management, personal care, and animal care markets.

Chapter 2

FIELD AREA

2.1 Geologic Setting

Understanding the geological environments that produce antibacterial minerals is important for identifying other promising reserves and for evaluating the geochemical diversity within specific deposits that coincide with bactericidal activity. The Oregon Mineral Technologies (OMT) clay deposit is located in the Cascade Mountains, (Douglas Co., OR) near Crater Lake. The deposit is part of the larger Cascade volcanic arc system that formed from the subduction of the Juan de Fuca plate beneath North America (Hammond, 1979; Sherrod and Smith, 2000; Bacon, 2008). The deposit lies at the eastern edge of the Western cascades which formed over the last 45 Ma (Walker and MacLeod, 1991; Sherrod and Smith, 2000). The majority of the western Cascades formed from 45-18 Ma with intermittent activity until 8 Ma (Hammond, 1979). The High Cascades to the east of the deposit began to form at 7 Ma, with Mt. Mazama forming around 1-2 Ma (Priest, 1990; Bacon, 2008) (Fig. 2.1).

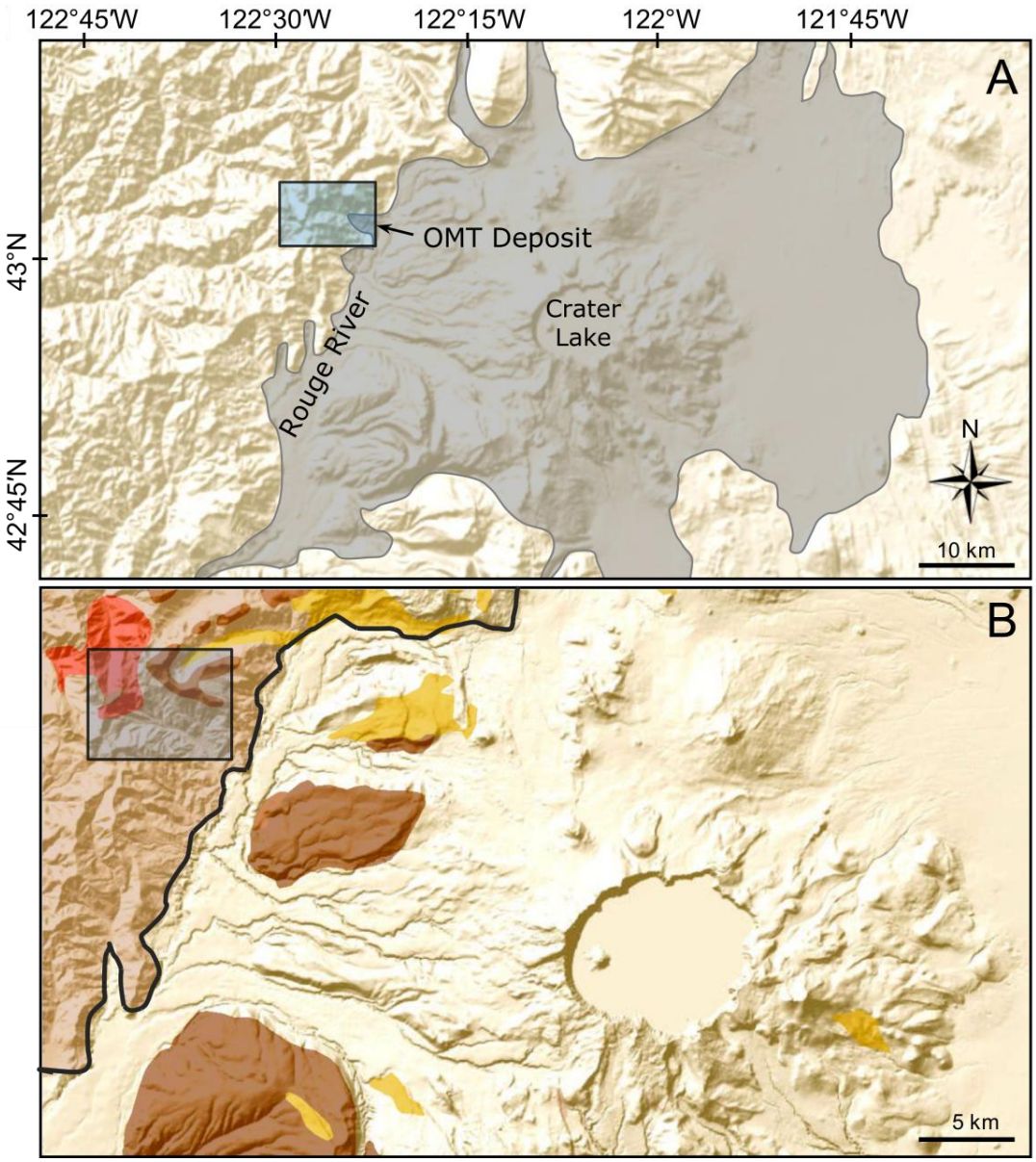

Figure 2.1. Location of the OMT deposit. (A) The OMT deposit (blue box) is located ~ 25 km NW of Crater Lake. The outlined area represents the maximum extent of pyroclastic flows remaining from the Mount Mazama eruption ~ 7,700 years ago (Bacon, 2008). (B) Color coded outlines of the geologic units associated with the deposit (Walker and MacLeod, 1991; Sherrod and Smith, 2000). Andesite lava flows (dark tan) ranging in age from 17-25 Ma make up the majority of the deposit. Hypabyssal intrusive diorite (red) range in age from 8-22 Ma. Capping basalts (brown) crown the deposit (10-17 Ma) and younger glacial deposits (yellow, 10-30 Ka) are found in the valley north of the pit. The light tan regions are Mt. Mazama pyroclastics.

Reconnaissance geologic mapping of the deposit (Ferrero, 1992) showed that regionally, dacite and andesite altered to pyrophyllite, pyrite and quartz along a major NW-SE trending fault. To the west, the OMT clay is covered by younger capping basalt, and to the east the deposit is bound by a NW-SE trending fault zone aligned with the Rogue River drainage (Fig. 2.3 A). This region is blanketed with volcanically-derived pyroclastic and ash deposits. Andesite lava flows make up the bulk of the deposit, ranging in age from 17-25 Ma (Walker and MacLeod, 1991; Sherrod and Smith, 2000). Zones of elemental sulfur are associated with hypabyssal intrusive rock (8-22Ma). The deposit is capped by basalts, which were deposited from 10-17 Ma. Recent glaciation (10-30 Ka) exposed the hydrothermally altered clay zones (Walker and MacLeod, 1991; Sherrod and Smith, 2000) (Fig. 2.1). The hydrothermally altered pyroclastics in the OMT deposit are much older (up to 25Ma) than the deposits of Mt. Mazama, which erupted only 7,700 years ago to form the Crater Lake caldera (Bacon et al., 1996). However, regional volcanic eruptions over the last ~70,000 years produced silica-rich magmas and generated hydrothermal waters that may have contributed to the alteration of the OMT deposit.

2.2 Mineral Sampling

The goal of the field work for this study was to identify and map the clay alteration zones in the OMT deposit, and sample for mineralogical and antibacterial analysis. Parent rock from each clay zone was sampled to determine the source of pyroclastic material that altered into clay. A series of roads used for logging provided access to four clay alteration zones that were identified for sampling (Fig. 2.2). These

will be referred to as the Open Pit Mine, Sulfur Mine, Foster Creek and Road Cut sites. An open pit mining site from the OMT prospecting was characterized by red and white oxidized zones overlying the more reduced blue clays (Fig. 2.3). Elemental sulfur, NW of the Open Pit (stratigraphically below), is found in lenses where sulfur mining occurred in the early 1900's (Fig. 2.3). Zones of blue clay exposed by Foster Creek were sampled, along with a large clay zone along a road cut (Forrest Service Road FS road 6520) associated with the Foster Creek drainage (Fig. 2.2 and 2.4). Outcrops of unaltered parent rock associated with each clay zone were collected to determine the pyroclastic material associated with the hydrothermal alteration (Fig. 2.2).

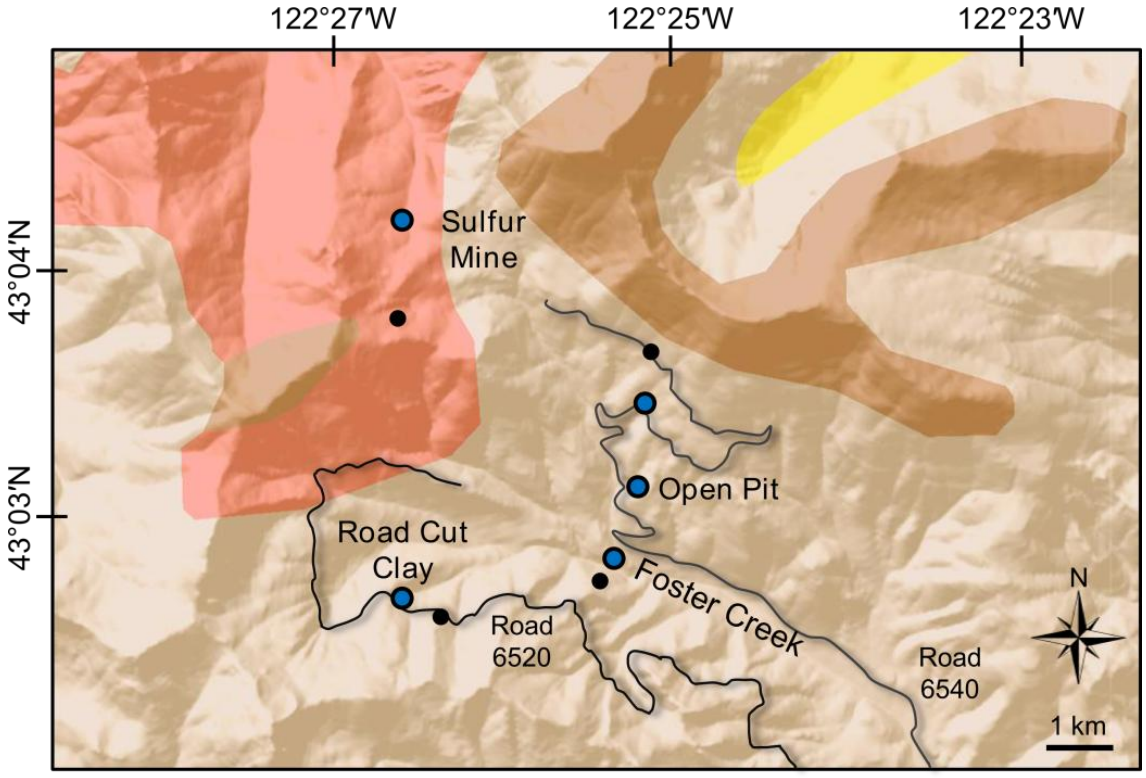

Figure 2.2. Sampling sites. Parent rock (black dots) and clay samplings sites (blue circles) from the OMT deposit. See Fig. 2.1 for descriptions of color shaded geologic units.

Hydrothermal alteration and weathering of the Open Pit resulted in three major clay zones representing variations in oxidation conditions (Fig. 2.3). Oxidized red and white zones found throughout the surface of the Open Pit and range in thickness from 3 to 9 meters. Post alteration minerals (gypsum, iron-oxides) occur in these zones, likely from meteoric waters oxidizing pyrite. Reduced blue clays zones are stratigraphically below the oxidized zones and in some regions reach a thickness of 600m (Ferrero, 1992).

Figure 2.3 A.

Figure 2.3. Open pit mine sampling site. (A and B) Open pit field area showing red-white oxidized clay zones above the un-oxidized blue clays. Solid white lines indicate the upper limit of the red and white oxidized zones, which are covered by glacial till. A series of NW-SE faults are present throughout the deposit, and exposed in the pit. (B) Image of the white-red oxidized zone with reduced blue clay zone beneath.

Blue clay zones in the Sulfur Mine were collected after removing the oxidized surface layers (Fig. 2.4 A). The Sulfur Mine sampling site contained veins of elemental S^0 surrounded by black sulfide-rich clay that grades out to blue clay (Fig. 2.4 B and C). Samples of the black and blue clay zones that graded out to less altered material were collected along with crystals of S^0 (Fig. 2.4 B).

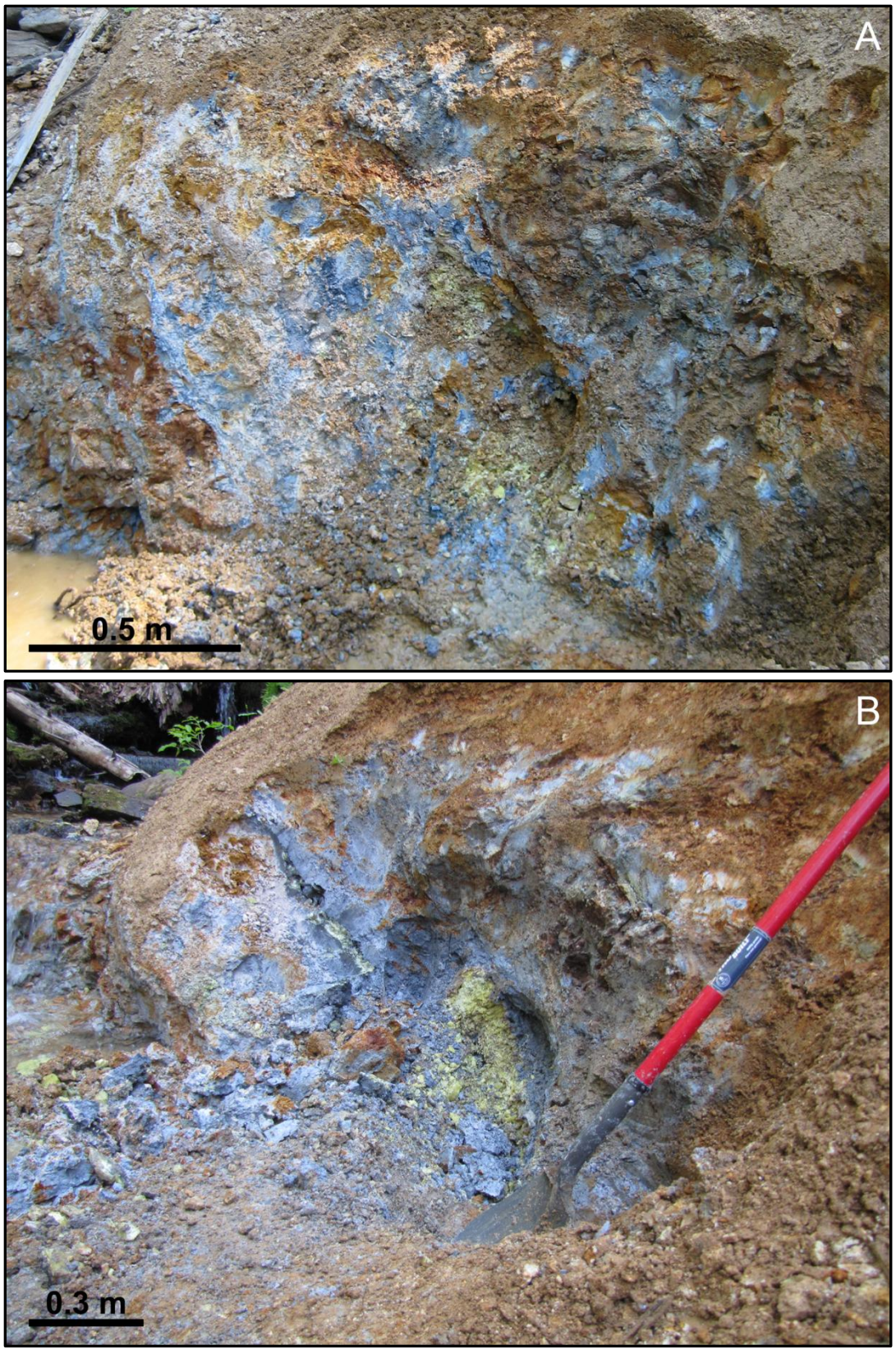

Figure 2.4 A and B.

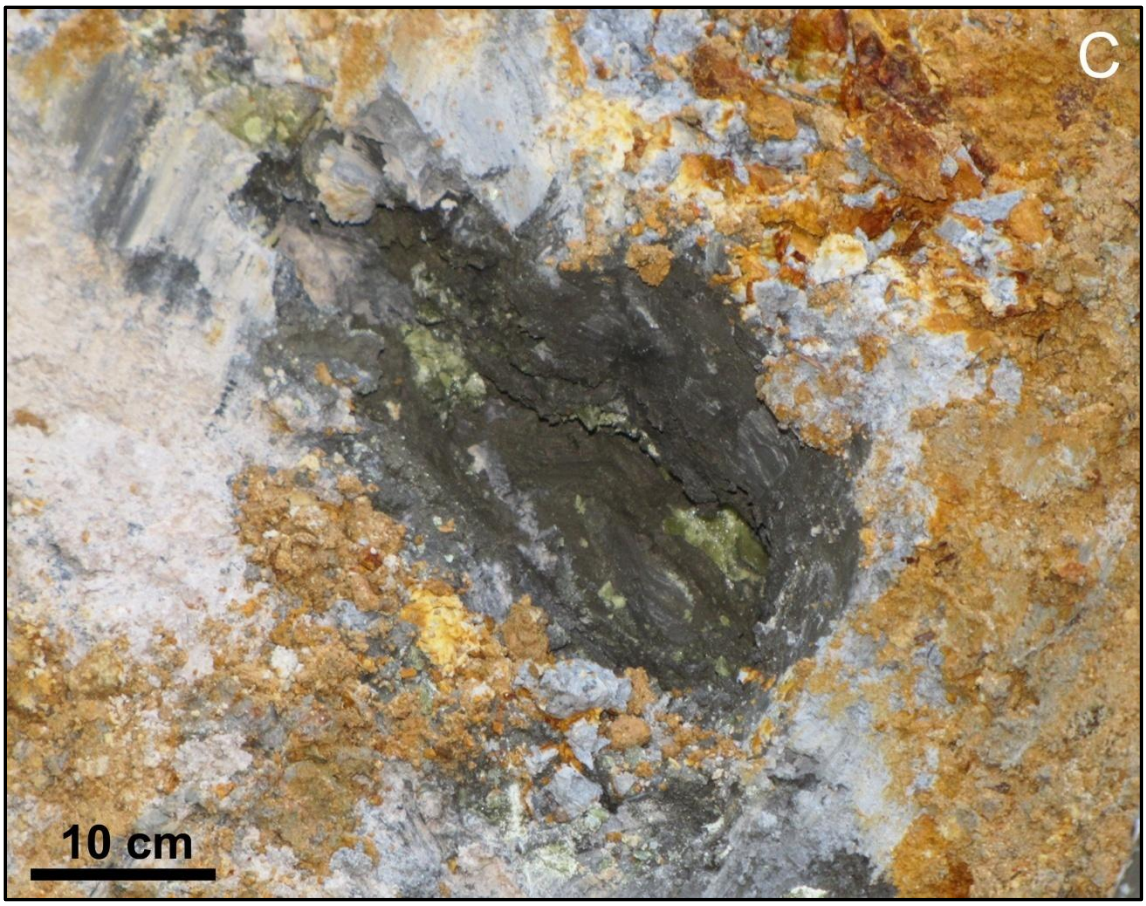

Figure 2.4. Sulfur mine sampling site. (A) Initial removal of oxidized surface layers. (B) Sulfur mine sampling site containing veins of S^0, surrounded by blue clays and (C) black clays containing high concentrations of disseminated pyrite.

Clay alteration zones at the Foster Creek site are associated with faulting and fracturing of the altered rock (Fig. 2.5 A). Fresh exposures of blue clay zones in the creek waters were also sampled (Fig. 2.5 B). Surface oxidation layers were removed and the blue clay zones were sampled.

Figure 2.5 A and B.

Figure 2.5. Foster Creek sampling of blue clay zones exposed by the creek drainage. (A) Red oxidized surface coatings had to be excavated to access the blue clay beneath. (B) Blue clay exposed in creek bed.

A clay zone to the east of Foster Creek was also identified along a road cut (Figs. 2.2 and 2.6 A). This clay zone was associated with a fault and extended > 5 m from the less altered wall rock. The soil and rock covering the blue clay zone was removed and samples were collected across a 4.5 m section (Fig. 2.6 B).

Figure 2.6 A.

Figure 2.6. Road cut sampling site. (A) Clay zone SW of Foster Creek associated with a fault. (B) Excavation of surface layers covering the blue clay zone, exposing a > 5 m clay zone for sampling.

The mineral samples collected from the OMT deposit were used to determine the hydrothermal conditions that generated these clay alterations by quantifying the mineral assemblages in each zone. Isotopic fractionation of oxygen in quartz was also investigated to place constraints on the hydrothermal fluid sources and temperature. Antibacterial susceptibility testing was initially examined in relation to the observed mineralogy (Chapter 3), followed by an investigation of the geochemical factors controlling the release of metals from the clays (Chapter 4). Finally, the antibacterial mechanism for the OMT clays was investigated utilizing an interdisciplinary approach that combines microbiology, geochemistry and biochemistry (Chapter 5).

Chapter 3

THE MINERALOGY OF AN ANTIBACTERIAL CLAY DEPOSIT

3.1 Introduction

The OMT clay deposit formed from hydrothermal alteration of volcanic rock, generating clay zones that are capable of killing pathogenic bacteria (Williams et al., 2011; Morrison et al., 2014). Here we present the detailed mineralogy of clays across the OMT deposit in relation to their antibacterial effectiveness against model Gram-negative and Gram-positive bacteria. This chapter will identify the geologic environment that lead to the formation of antibacterial clay zones in the OMT deposit.

Characterization of hydrothermal alteration is based on the observed mineral assemblages and chemical changes that occur as a result of alteration (Barnes, 1997; Pirajno, 2009). The identification of hydrothermal alteration zones is important for ore exploration, providing clues to the physio-chemical conditions that form economically viable deposits. Hydrothermal mineral deposits form as heated fluids interact with rocks (typically 50-600°C) (Pirajno, 2009). Hydrothermal clay deposits typically form distant (1-3 km) from the heat source (magma) through lower temperature epithermal and geothermal alteration (Velde, 1995; Meunier, 2005). These deposits contain lower grades of metals and many times represent the gangue minerals that must be excavated to reach the ore body of interest (Barnes, 1997). By characterizing the hydrothermal alteration conditions that produce antibacterial clay deposits we may identify similar deposits worldwide, and show a novel economic use for such deposits.

3.2 Characterizing Hydrothermal Alteration Systems

The OMT mineral deposit is located in the Cascade mountain range, which formed in a volcanic arc setting (Hammond, 1979; Sherrod and Smith, 2000). Volcanic arcs form during the subduction of oceanic crust into the mantle below the continental crust, resulting in dehydration and partial melting of the oceanic plate (Hammond, 1979; Hedenquist and Lowenstern, 1994). The melted oceanic plate ascends toward the continental crust forming volcanic mountain ranges. These intrusive melts provide the heat source for hydrothermal processes, producing characteristic mineral alterations and ore bodies (Barnes, 1997).

Hydrothermal alteration occurs when rocks react with heated water, leading to the formation of new mineral assemblages. As the parent rock is hydrothermally altered, mineralized zones can form a capping barrier that block the migration of hydrothermal fluids and vapors. As pressure increases the capping zone can be hydraulically fractured and brecciated, transferring heat and fluids through the rock (Barnes, 1997; Pirajno, 2009). Tectonic activity also influences hydrothermal alteration, by generating faults and fractures in the rock, increasing fluid convection and heat transfer (Barnes, 1997; Meunier, 2005; Pirajno, 2009). The lower density of the heated fluids causes them to rise through the fractured rock, mixing magmatic and meteoric fluids through convection cycles (Hedenquist and Lowenstern, 1994; Velde, 1995; Meunier, 2005) (Fig. 3.1). As these fluids continue to rise, pressure decreases and boiling occurs, altering the rock at lower temperature (Fig. 3.1). Convecting meteoric ground waters can reach depths of 2-3 km, transferring heat and hydrothermal fluids away from the magmatic heat source,

resulting in zones of lower temperature (< 300°C) epithermal alteration up to 2 km away from the magmatic heat source (Hedenquist and Lowenstern, 1994; Velde, 1995).

3.2.1 High and Low Sulfidation Alteration

The major gasses in magmatic fluids are SO_2, CO_2, with minor amounts of HCl and HF (Hedenquist and Lowenstern, 1994). Changes the oxidation state of sulfur in hydrothermal fluids can influence the mineral assemblages that form during epithermal alteration, providing valuable field relations for ore exploration (Hedenquist and Lowenstern, 1994; Barnes, 1997). Epithermal alteration can be divided into two main types depending on the redox state of sulfur in the gas phase. In low-sulfidation systems sulfur is reduced (H_2S) and alteration occurs at near neutral pH with reduced fluid flow (Hedenquist and Lowenstern, 1994; Pirajno, 2009). High-sulfidation alteration systems are characterized by oxidized sulfur (SO_2) in magmatic fluids and occurs at low pH (< 2) with high salinity (Hedenquist and Lowenstern, 1994). Acid is generated through the disproportionation of SO_2 at elevated temperature (250°-280°C) (reaction 1) (Hedenquist and Lowenstern, 1994; Barnes, 1997; Delmelle et al., 2000). This process generates acidic leaching fluids during high-sulfidation alteration, leaving behind vuggy silica and advanced argillic zones where precious metals are deposited (Velde, 1995; Barnes, 1997; Hedenquist and Lowenstern, 1994).

$$4SO_2 + 4H_2O \rightarrow 3H_2SO_4 + H_2S \qquad (1)$$

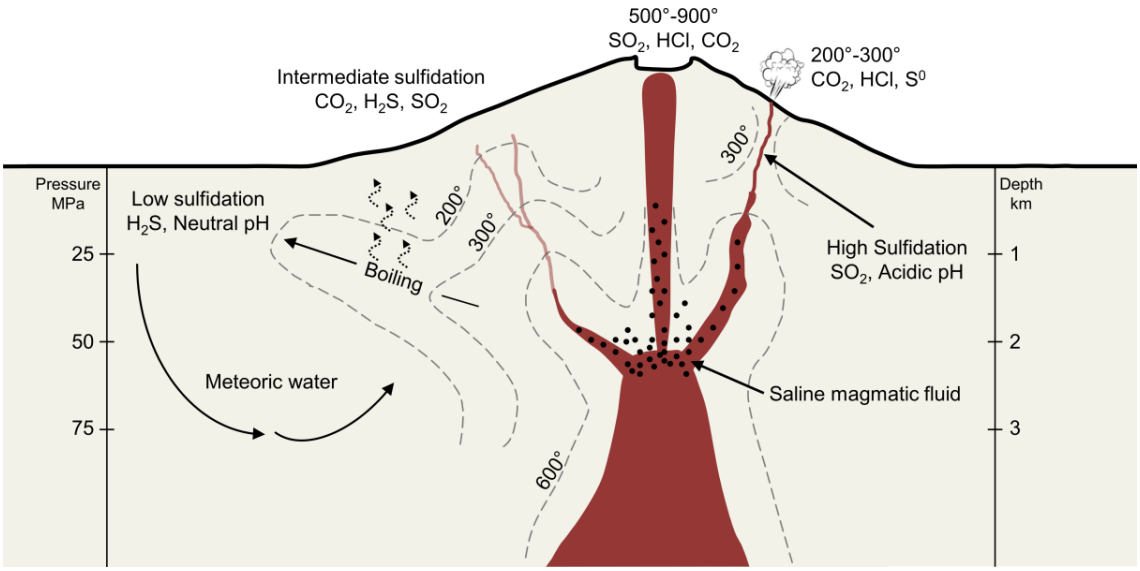

Figure 3.1. Hydrothermal alteration systems. Representation of hydrothermal alteration from sub-volcanic intrusions associated with a stratovolcano (modified from Hedenquist and Lowenstern, 1994). Porphry alteration occurs at higher temperatures (> 600° to 300°C) and greater depths (2-5 km) in direct proximity to the magmatic intrusion, resulting in high temperature acid alteration and the formation of ore bodies. Magmatic fluids associated with porphyry alteration ascend and degas, generating acidic fumaroles and high-sulfidation epithermal alteration at elevated temperatures (>300°-200°C). Low-sulfidation alteration occours more distant from the magmatic source at neutral pH and lower temperature (< 300°C).

3.2.2 Hydrothermal Mineral Zones

The temperature, pH and cation content of hydrothermal fluids produce characteristic mineral zones that are used to identify and categorize ore deposits (Utada, 1980; Velde, 1995). Alteration zones can be characterized by their major cation/H^+ ratio, with low ratios in acidic systems that increase in intermediate and alkaline alteration (Fig. 3.2). Acid alteration causes leaching of the parent rock leaving Al_2O_3 and SiO_2 forming kaolin group minerals and pyrophyllite at higher temperatures (Fig. 3.2). These acidic zones represent high-sulfidation alteration by oxidized fluids (Hedenquist and

Lowenstern, 1994). Intermediate and alkaline alteration fluids contain alkali or alkaline earth elements and neutral to alkaline pH. Intermediate mineral zones are characterized by smectite group minerals at lower temperature (< 150°C), followed by the formation of mixed layered clays (illite-smectite, chlorite-smectite) at elevated temperature (150°-250°C). This neutral pH alteration is found in low-sulfidation deposits. Alteration minerals in the alkaline series are predominantly zeolites, which form in relation to the dominant cations present during alteration (Ca, Na) (Fig. 3.2).

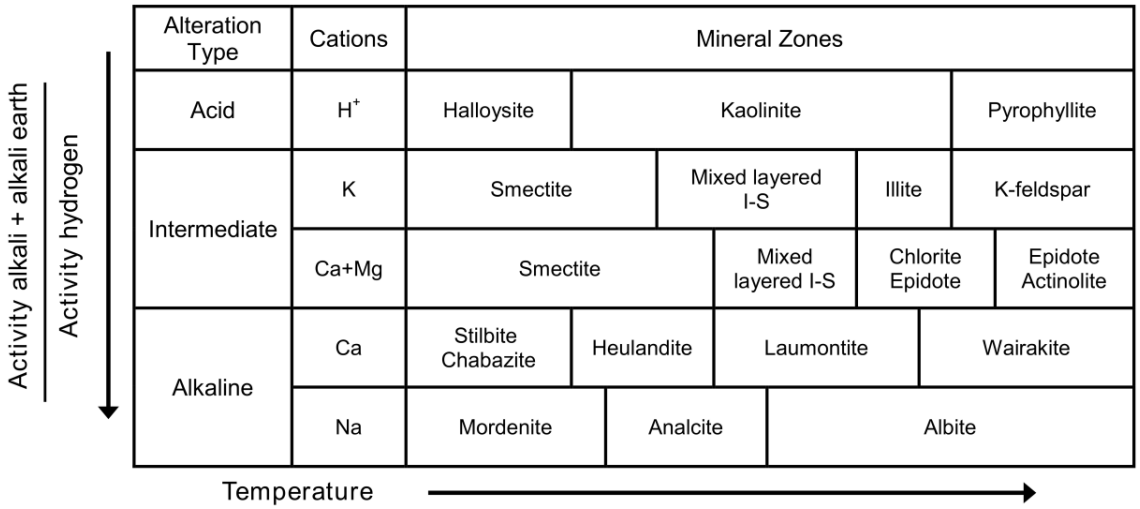

Figure 3.2. Fluid composition and mineral alteration. Diagram illustrating the mineralogical changes corresponding to fluid pH, salinity and temperature that separate hydrothermal alteration zones (figure modified from Utada, 1980). The ratio of cations/H^+ along with the temperature of hydrothermal fluids dictates the mineral assemblage formed.

Our current understanding of hydrothermal alteration is largely based on porphyry-Cu deposits which produce economically viable metal ores (Utada, 1980; Barnes, 1997; Pirajno, 2009). The classification system used to describe porphyry alteration is based on the observed changes in mineral zones and is not necessarily related to the formation process of the alteration zone. The alteration mineral assemblages are grouped into four categories; argillic, phyllic, propylitic and potassic (Table 3.1). This classification system has been divided further into sub-categories that characterize a variety of mineral assemblages associated with different alteration conditions. Lower temperature epithermal alteration (< 300°C, < 1 km below surface) produces clay assemblages through argillic, propylitic and phyllic alteration (Table 3.11) (Velde, 1995; Pirajno, 2009). Potassic alteration associated with porphyry-Cu deposits occurs at high temperature (>600°C to 400°C) closer to the intrusive magmatic heat source (2-4 km), altering the rock into K-feldspar, micas and quartz (Velde, 1995). At this high temperature, acidic and saline fluids preclude the formation of the clay mineral assemblages found in the OMT deposit.

Table 3.1. Mineral assemblages associated with hydrothermal alteration. The major mineral phases are listed in bold (Pirajno, 2009).

Alteration	Mineral Assemblage	Sulfidation State
Advanced Argillic	**pyrophyllite, dickite**, quartz, alunite, pyrite	high-sulfidation epithermal
Argillic	**kaolinite, montmorillonite,** chlorite, muscovite	high and low-sulfidation epithermal, geothermal
Intermediate Argillic	**chlorite, sericite**, kaolinite, smectite, illite-smectite, carbonates, pyrite	high and low-sulfidation epithermal, geothermal
Propylitic	**epidote, chlorite, albite,** carbonates, smectite, illite-smectite, pyrite	high and low-sulfidation epithermal, goethermal
Phyllic	**sericite, quartz, pyrite,** chlorite, illite, biotite, K-feldspar, albite, pyrite	high-sulfidation epithermal, porphyry
Potassic	**K-feldspar, biotite, quartz,** biotite, chlorite,epidote, albite, pyrite	porphyry

3.2.3 Clay Mineralogy

As smectite and illite-smectite (I-S) are generated by hydrothermal alteration, changes in their *Reichweite* ordering (stacking order of clay layers) occurs. The *Reichweite* (R) ordering system is determined by the probability of illite or smectite layers occurring next to each other (Środoń, 1980; Moore and Reynolds, 1997). The ordering probability of illite layers in perfectly ordered I-S (ISIS, rectorite) is 1 and increases to 3 as illite layers increase proportionally (SIII). These stacking sequences are referred to as R1 to R3 ordering. R0 represents random stacking of illite and smectite layers. As temperatures increase the ordering of the illite-smectite increases (R0 to R3). However, time and the availability of major cations needed to precipitate authigenic layers also play a role in the ordering of I-S (Meunier, 2005). The R ordering of mixed-layered clay minerals that are at equilibrium in their environment can provide broad insight into the temperatures reached during hydrothermal alteration. The hydrothermal alteration of volcanic rocks at lower temperatures (< 150°C) often forms smectite, whereas at higher temperatures (250-300°) illite stability is favored, therefore mixed-layered I-S minerals indicate a transitional stability field between end-member smectite and illite. At temperatures above 300°C pure illite is stable, providing temperature constraints in hydrothermal systems (Velde, 1995; Meunier, 2005).

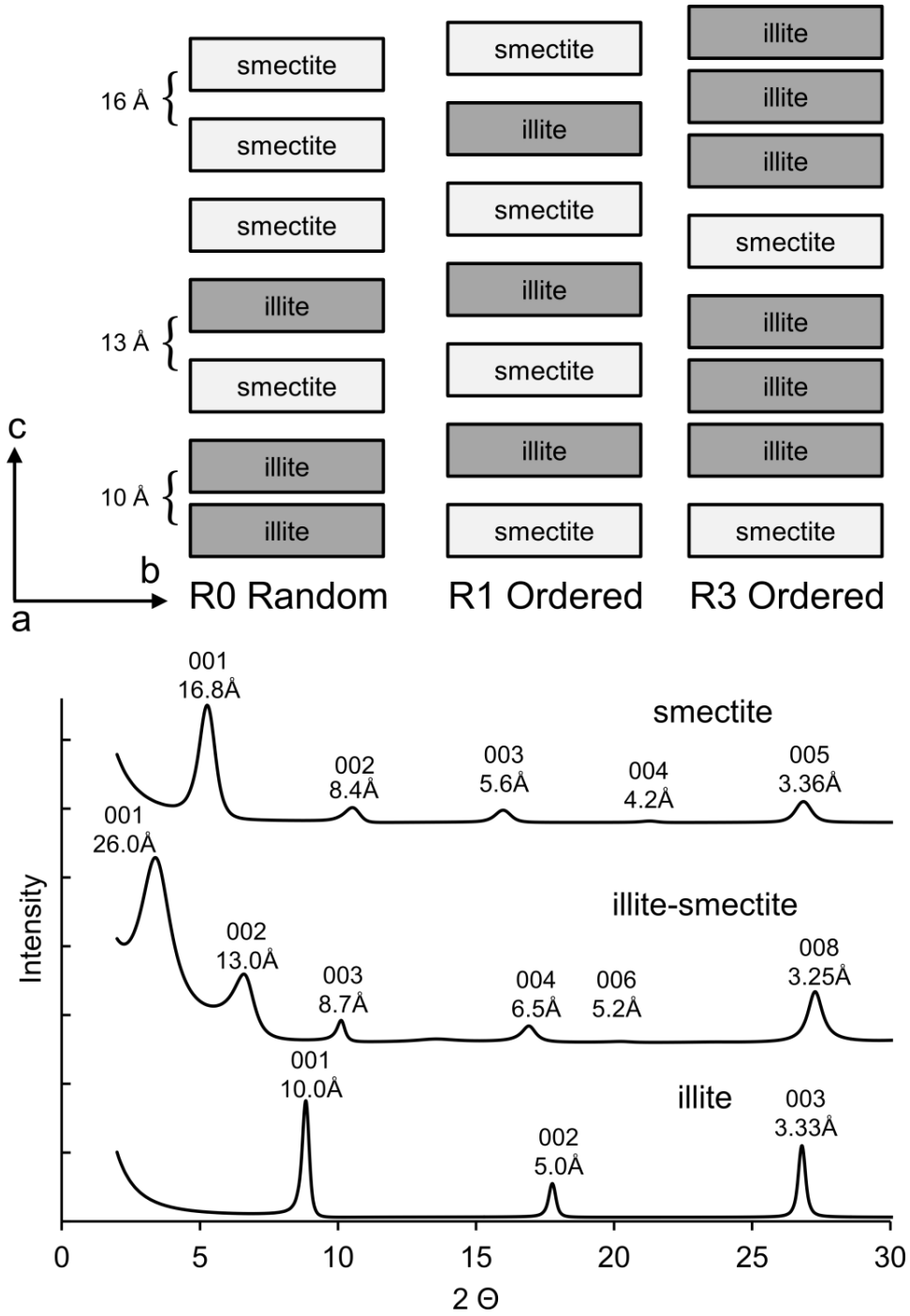

Figure 3.3. Clay mineralogy. Illustration of I-S *Reichweite* ordering showing R0 with random I-S stacking, R1 ordered stacking with 50% illite and smectite layers and R3 ordered containing higher illite content and ordering. Calculated XRD patterns of oriented glycolated smectite, rectorite and illite. The oriented clays stack into layers aligned along the *c*-axis.

The ordering and I-S layer percentages can be determined by measuring the distance between diffraction peaks in XRD patterns of oriented glycolated samples (Moore and Reynolds, 1997). Glycol enters the interlayer space of expandable clays (smectite group) propping open the layers that collapse in the air-dried state. Oriented clays are aligned along the c-axis, which enhances the basal (*00l*) reflections. When saturated with ethylene glycol, uniform spacing (Å) between the clay layers occurs. The *001* reflections of expandable smectite occur at >16 Å, while non-expandable illite has a spacing of 10Å. The spacing of mixed layered I-S falls in-between smectite and illite (Fig. 3.3). Percentages of illite and smectite can be calculated using the ratios of *00l* reflections between pure illite and smectite (Reynolds, 1980; Środoń, 1980).

3.3 Results

3.3.1 Parent Rock

The hydrothermal alteration of volcanic rock is governed mainly by temperature and fluid composition, however the parent rock type also influences alteration products (Velde, 1995). Andesite porphyry rocks are pervasive throughout the OMT deposit and appear to be the parent rock that was hydrothermally altered in the Open pit, Foster Creek and Road Cut sampling sites (Fig 2.2). Previous studies have identified hypabyssal intrusive rocks associated with the Sulfur Mine which suggests more mafic parent rock in the deeper parts of the system (Power et al., 1981; Fiebelkorn et al., 1983). Major elemental compositions of the bulk parent rock were determined using XRF (see Chapter 7 Methods). Compositions of the major elements in the parent rock are characteristic of calc-alkaline magmatic systems with basaltic to andesitic composition (Table 3.2). The

parent andesite associated with Open Pit Mine was taken stratigraphically above the pit, outside of the highly altered clay zones (Fig. 2.2). The Open Pit and Road Cut andesites are elevated in Al_2O_3 and Na_2O compared to Foster Creek. The Sulfur Mine parent rock has a basaltic composition with high Fe, Mg and Ca content (Table 3.2).

Table 3.2. Elemental analysis of parent rock samples. Abundances are expressed as weight % oxides.

Element	Open Pit	Sulfur Mine	Foster Creek	Road Cut
SiO_2	58.48	49.97	56.97	56.59
Al_2O_3	19.16	17.97	17.97	19.29
Fe_2O_3	6.61	10.09	6.09	6.95
MgO	2.75	6.15	3.15	2.42
CaO	5.84	9.19	8.19	8.48
K_2O	1.58	1.35	1.35	1.27
Na_2O	2.99	0.9	1.9	2.52
TiO_2	0.79	1.21	1.2	0.93
MnO	0.08	0.13	0.13	0.14
P_2O_5	0.16	0.41	0.41	0.22

XRD patterns (Fig. 3.4) reveal lower temperature alteration minerals in the parent rocks. This lower grade alteration produced zeolites, quartz and clay minerals. Alteration of the Open Pit parent rock resulted in smectite, chlorite, and laumontite. Unaltered plagioclase feldspars (andesine, oligoclase) are present, reflecting incomplete hydrothermal alteration. Andesites from Foster Creek contain quartz, stilbite and plagioclase (oligoclase). Alteration of andesites from the Road Cut site resulted in chabazite formation and lower peak intensities for plagioclase (labradorite) (Fig. 3.4). XRD patterns of the sulfur mine basalt show only plagioclase feldspars (labradorite), which suggest negligible alteration occurred (Fig. 3.4 E). Antibacterial susceptibility testing of the parent rocks revealed no antibacterial activity.

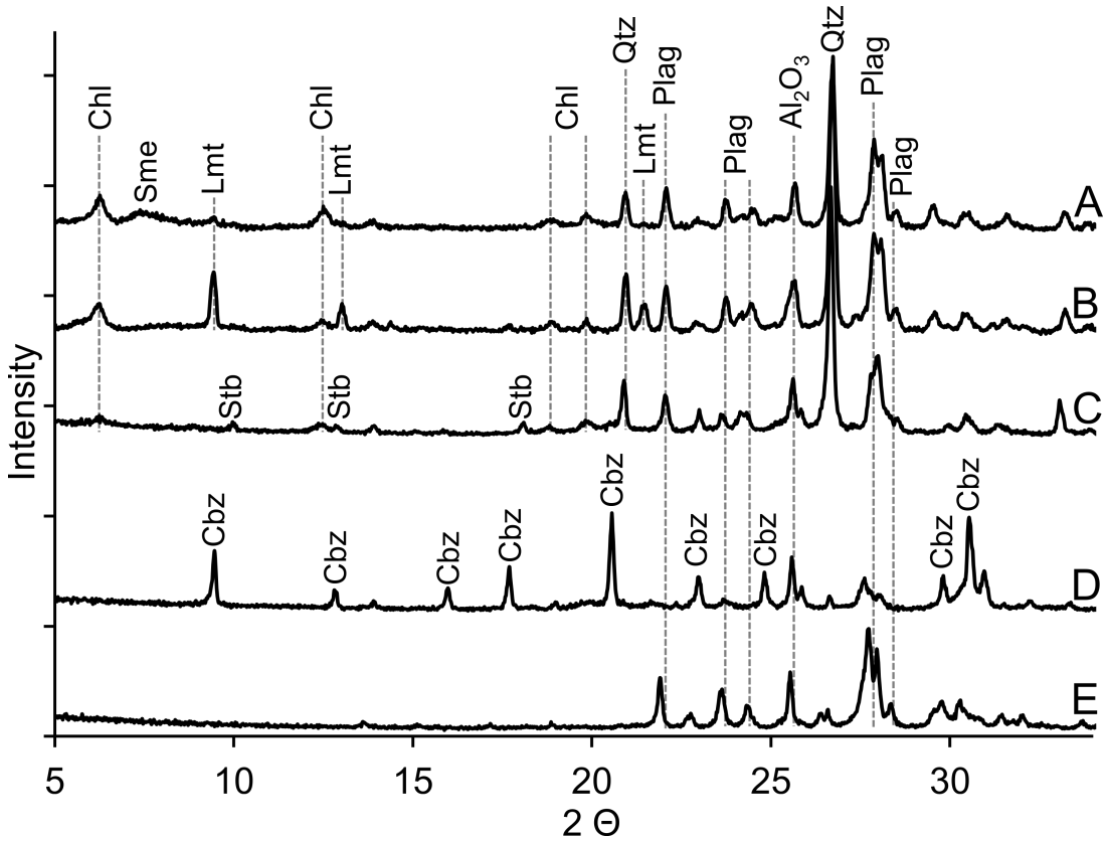

Figure 3.4. Parent rock X-ray diffraction. XRD patterns of parent rocks associated with (A and B) Open Pit Mine, (C) Foster Creek, (D) Road Cut site and (E) Sulfur Mine. Hydrothermal alteration minerals include; quartz (Qtz), chlorite (Chl), laumontite (Lmt), stilbite (Stb), chabazite (Cbz) and smectite (Smec). Abundant primary plagioclase (Plag) feldspars reflect the incomplete alteration.

3.3.2 Clay Mineralogy

Detailed descriptions of clay sampling sites and quantitative XRD will be discussed in the following sections. However, accurate identification of clay minerals must be performed before quantitative XRD analysis. In brief, clay size fractions were separated (<2.0 µm, Na-exchanged), dried onto glass slides and saturated with ethylene glycol (details in Chapter 7 Methods). Modeling of the < 2.0 µm, oriented, glycolated XRD patterns was performed using the program Sybilla (Chevron ETC®, McCarty et al.,

2008). The blue clay from the Open Pit (Fig. 3.5) is dominated by illite-smectite containing 55% illite, which is the mineral rectorite (Eberl, 1978) (Fig. 3.5 A), not pyrophyllite as previously identified by field geologists (Ferrero, 1992). A clay exposure NE of the open pit was also sampled which contained plagioclase (> 20%) rectorite and minor pyrite indicating less intense hydrothermal alteration.

Samples from the Sulfur Mine location contained veins of elemental sulfur surrounded by black clay transitioning to blue clay. The < 2.0 μm fraction of the black clays contained I-S (75% illite) R>1 and R0 illite- smectite (20% illite) with minor amounts of kaolinite (Fig. 3.5 D), that transitions to pure smectite in the less altered rock adjacent to the vein (Fig. 3.5 C). Samples from Foster Creek contained I-S (70% illite) with R>1 ordering, along with kaolinite and a minor amount of smectite (Fig. 3.5 E). The formation of kaolinite is associated with more acidic alteration (pH < 4) where Al solubility increases (Reyes, 1990; Velde, 1995). The I-S from the Road Cut clay site, located to the south of the study area (Fig 2.2), contained 85% illite with R3 ordering indicating higher temperature alteration (Fig. 3.5 G).

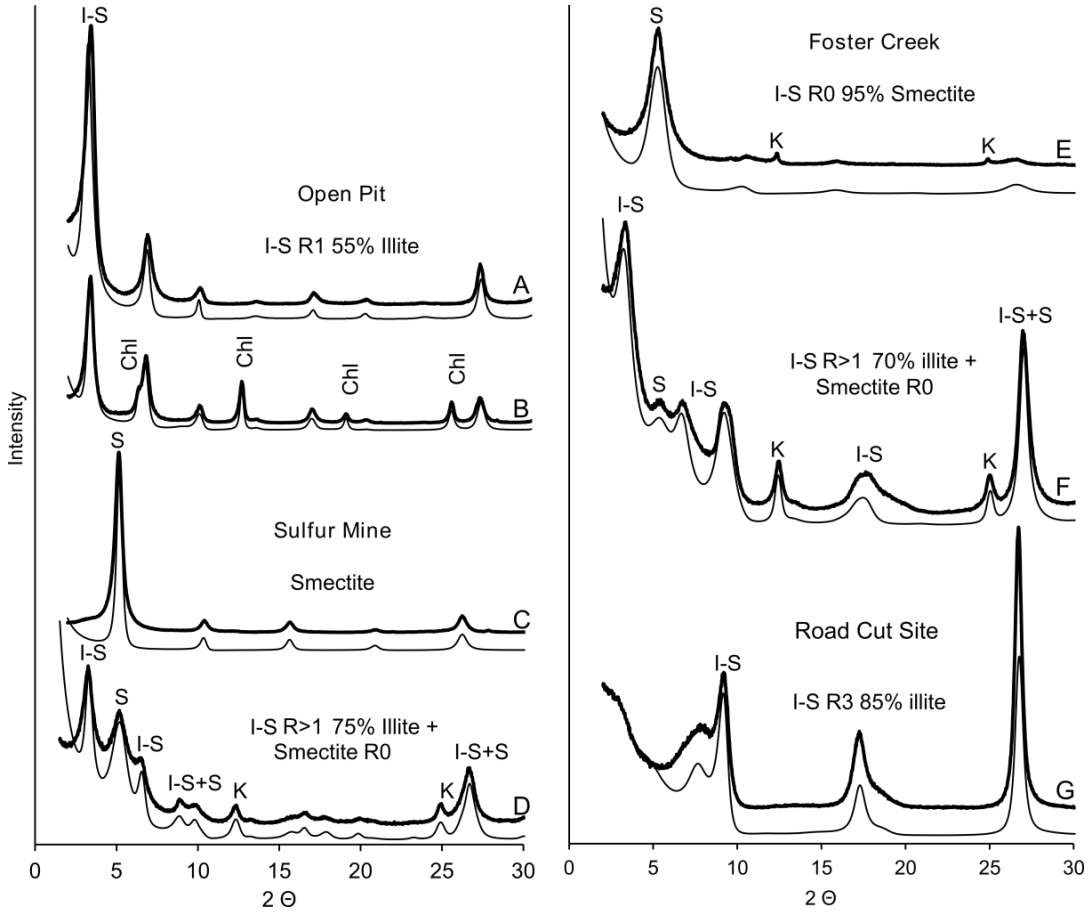

Figure 3.5. Oriented clay XRD patterns. Oriented glycolated <2 μm clay fraction XRD patterns are shown with modeled XRD patterns beneath each sample. (A) Open Pit rectorite and (B) sample taken stratigraphically above the pit with rectorite and chlorite. (C) Sulfur Mine sample of less altered wall rock adjacent to the black and blue clay vein. (D) Black clay sample form the Sulfur Mine, surrounding elemental sulfur crystals, containing a mixture of I-S (75% illite), smectite and kaolinite. (E) Smectite rich sample from Foster Creek. (F) Foster Creek clay vein containing I-S (70% illite) with kaolinite and smectite. (G) Road Cut clay sample containing I-S (855) with R3 ordering. Minerals abbreviations; smectite (S), illite-smectite (I-S), chlorite (Chl) and kaolinite (K).

3.3.3 Open Pit Mine Mineralogy

Oxidized red and white zones above the more reduced blue zones were sampled in the Open Pit (Fig. 3.6A). Samples of blue clay were taken at the interface of the white and blue zones down to 1.5 meters. A series of NW-SE faults run through the pit and

produce white mineral alteration zones (Fig. 3.6 A), and finally a stockwork of non-directional quartz veins are found throughout the blue zone (Fig. 3.6 B). The detailed mineralogy of each alteration assemblage is presented below.

The mineralogy of the Open Pit blue clays (Table 3.3) is dominated by rectorite (40-50 %), quartz (36-49 %) and pyrite (4-6 %); a mineral assemblage suggesting low sulfidation argillic alteration at neutral pH. Clays from the oxidized red and white zones located directly above the blue zone contained no measureable pyrite. The main Fe-bearing mineral phase within the red zone (sample P1) is goethite, which forms from the oxidation of pyrite. In addition to the I-S, minor kaolinite and chlorite are present in the red zone, which likely formed from the acidity generated through pyrite oxidation. The white zone (sample P2) contained 6.3 % smectite in addition to the I-S and trace kaolinite. Secondary minerals gypsum, jarosite and goethite are present in this zone and are characteristic of acidic mine environments as a result of pyrite oxidation (Murad and Rojik, 2003; 2005). Minor amounts of plagioclase feldspars from the parent rock andesite are identified in a portion of the samples (Table 3.3). A stockwork of veins containing quartz and elevated pyrite concentrations (9%) fills fractures in the open pit blue zones. A zone of blue clay was also sampled stratigraphically above the open pit that contained plagioclase, rectorite, chlorite and trace amounts of pyrite. This mineral assemblage reflects lower hydrothermal alteration grading to the lower temperature alkaline alteration of the andesite parent rock.

Figure 3.6 A and B.

Figure 3.6. Open Pit mineralogy. (A) Image of the un-oxidized blue rectorite zone, crosscut by a white oxidized zone associated with a fault (ruler markers are 0.3 m apart for scale). (B) Stockwork of quartz-pyrite veins running through the rectorite dominated blue clay.

Table 3.3 Open Pit XRD. Quantitative XRD results reported as mineral weight percent (Wt. %). Surface samples are from the oxidized red (P1) and white (P2) zones. Blue clay samples were taken at the interface of the oxidized zone from 0.1-1.5 m depth. Samples highlighted in blue are bactericidal against (*E. coli* and *S. epidermidis*) while the light grey samples only inhibit bacterial growth. Un-highlighted samples were non-antibacterial.

Sample	Depth	Quartz	Plagioclase	Pyrite	Gypsum	Jarosite	Goethite	Rectorite	Chlorite	Smectite	kaolinite
P1	0.0 m	36.3	4.6				3.4	44.6	3.5		4.7
P2	0.0 m	48.5	2.9		2.7			36.6		6.3	
P3	**0.1 m**	**46.5**		**5.6**	**1.1**	**1**		**42**			
P4	**0.1 m**	**45.3**	**0.8**	**4.4**	**0.8**	**0.7**		**48.3**			
P5	**0.3 m**	**45.8**	**0.6**	**4.6**	**0.4**	**1.2**		**42.1**			
P6	**0.6 m**	**42.9**		**4.6**	**1.2**	**0.9**		**45.3**			
P7	**0.6 m**	**42.3**	**0.4**	**4.3**	**1.2**			**46.6**			
P8	0.9 m	42.2		5	1.9			47.4			
P9	0.9 m	42.6		5.4	2.1			46.1			
P10	1.2 m	43.7	0.7	5	1.9			49.1			
P11	1.2 m	42.6		5.6	1.6			46.7			
P12	1.5 m	41.9		6.5	2.4			48.1			
P13	Stock work	70.2		9.4				19.7			
P14	Fault	32.8						65.7			
P15	*Above Pit	37.7	21.2	0.5				29.6	8.4		

*Sample collected stratigraphically above the open pit (See Fig. 2.2 for location).

Details of the antibacterial testing are given below to identify the basic mineralogical variables corresponding with antibacterial activity throughout the deposit. The detailed geochemistry and antibacterial activity is presented in Chapters 4 and 5, providing context to the observed field relations and antibacterial activity. The main objective is to determine if mineralogy alone dictates antibacterial activity in different alteration zones of the OMT deposit. The antibacterial activity of the mineral samples will be expressed as; bactericidal (killing 100%), inhibitory (preventing growth) and non-antibacterial (no affect on growth).

The Open Pit antibacterial susceptibility testing (see Chapter 7 Methods) shows that blue clays sampled just below the oxidized zone (0.1 m depth) are bactericidal against *E. coli* and *S. epidermidis* (Table 3.3). With increasing depth in the pit the blue zone becomes less antibacterial, only inhibiting bacterial growth. Pyrite concentrations in the blue zone are fairly uniform (4-6%). Jarosite occurs in the upper 0.6 m of the pit from the oxidation of pyrite. The veins of quartz in the blue clay contain 9.4% pyrite, but showed no antibacterial activity. However, the clays from the white oxidized zone with no pyrite do inhibit bacterial growth (Table 3.3). Clays in the red oxidized zone contained goethite indicating a higher oxidation state, and showed no antibacterial activity. These results indicate that the presence of pyrite alone does not govern the antibacterial activity of the clays in the open pit but that the oxidation state of the mineral assemblage is more important.

3.3.4 Sulfur Mine Mineralogy

The mineralogy in the Sulfur Mine is characterized by veins of S^0 surrounded by black clay containing fine disseminated pyrite (10-18%) and I-S (R>1, 75% illite). The blue clays adjacent to the black clay (Fig. 3.7 A) contain a mixture of I-S that transitions (toward the parent rock) to smectite with plagioclase feldspar, indicating lower intensity alteration. The walls of the vein contain dolomite and calcite (1-2 wt.%) suggesting that a higher pH environment existed during their formation. Kaolinite (1-5%) is found intermittently in the vein (Table 3.4) marking more acidic alteration conditions. This supports a scenario where partial alteration of the wall rock by acidic fluids causes the release of Al and alkaline earth elements forming kaolinite. As acidity is neutralized carbonates precipitate as late phases (Keith and Bargar, 1988; Bargar and Keith, 1999). The overall mineralogy of the Sulfur Mine region and presence of S^0 are characteristic of intermediate argillic zones with high-sulfidation epithermal alteration at temperatures below 300°C (Table 3.1). The sharp transition from zones of I-S, pyrite and sulfur to carbonate, pyrite, plagioclase and smectite suggests a short lived alteration event from an intrusive hydrothermal vein.

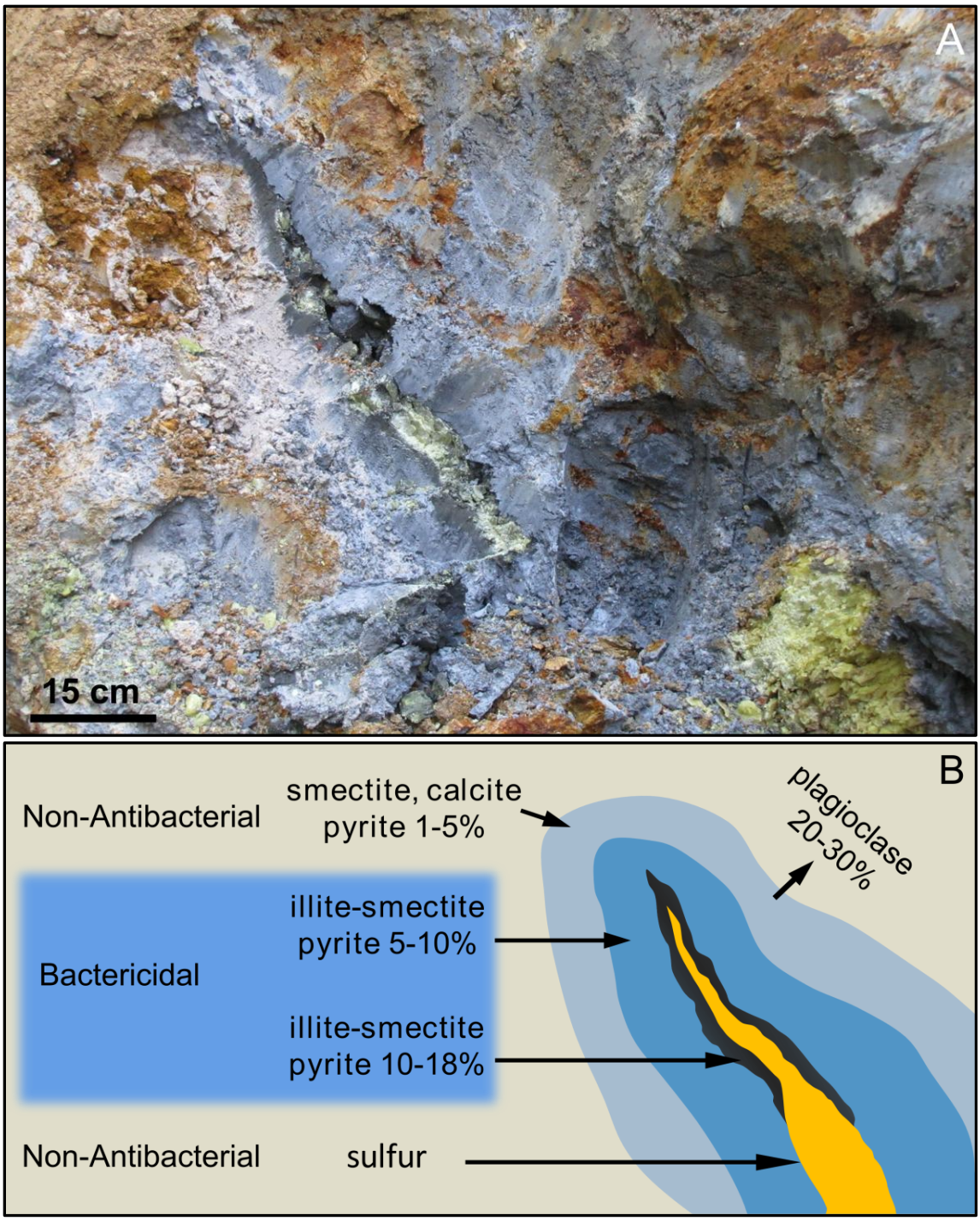

Figure 3.7. Sulfur Mine mineralogy. (A) Veins of pure elemental sulfur are found surrounded by black clay (I-S R1 75% illite) with disseminated pyrite (10-18%) that grades out to I-S + smectite and pure smectite (45%) with plagioclase feldspar (22%) and minor calcite (2.7%) at the perimeter. (B) Diagram illustrating the antibacterial activity of the alteration series surrounding the S^0 veins.

Samples from the Sulfur Mine showed a sharp contrast in antibacterial activity, with zones that completely killing *E. coli* and *S. epidermidis* or not affecting growth at all (Fig. 3.7 B, Table 3.4). Pyrite levels reach 18% in the most antibacterial samples. In contrast, samples containing carbonate, pyrite and plagioclase were not antibacterial. Additionally, crystals of pure S^0 showed no antibacterial activity against *E. coli* and *S. epidermidis*.

Table 3.4. Sulfur Mine XRD. Results are reported as mineral weight percent (Wt. %). Samples highlighted in blue are bactericidal while un-highlighted samples were non-antibacterial.

Mineral	S1	S2	**S3**	**S4**	**S5**	**S6**	**S7**	**S8**	S9	S10
Quartz	37.5	42.8	**38.1**	**34.9**	**35.8**	**28.9**	**13.5**	**39.5**	18.1	19.9
Plagioclase									21.6	31.9
Calcite		1.0							2.7	
Dolomite	5.5									
Pyrite	4.6	5.9	**8.3**	**18.7**	**13.3**	**5.5**	**10.8**	**11.5**	5.1	1.2
Sulfur				**5.2**			**50.4**	**1.7**		
Gypsum	0.6								2.7	2.9
Jarosite	0.4		**1.5**		**1.3**			**2.2**		
Kaolinite	5.1	4.4	**3.1**			**1.4**		**3.1**		
Smectite			**9.3**			**45.7**			46.8	43.3
I-S >70%	41.9	46.9	**36**	**37.5**	**49.6**	**17.8**	**22.7**	**41.3**		

3.3.5 Foster Creek Mineralogy

A blue clay interval associated with faulting was sampled along with blue clay zones exposed by the Foster Creek drainage (Fig. 3.8). Calcite, dolomite, smectite, kaolinite and pyrite are found in the majority of the clay exposures in this region (Table 3.5). Pyrite concentrations were ~4% throughout the Foster Creek alteration zone and most areas contained carbonates (Table 3.5).

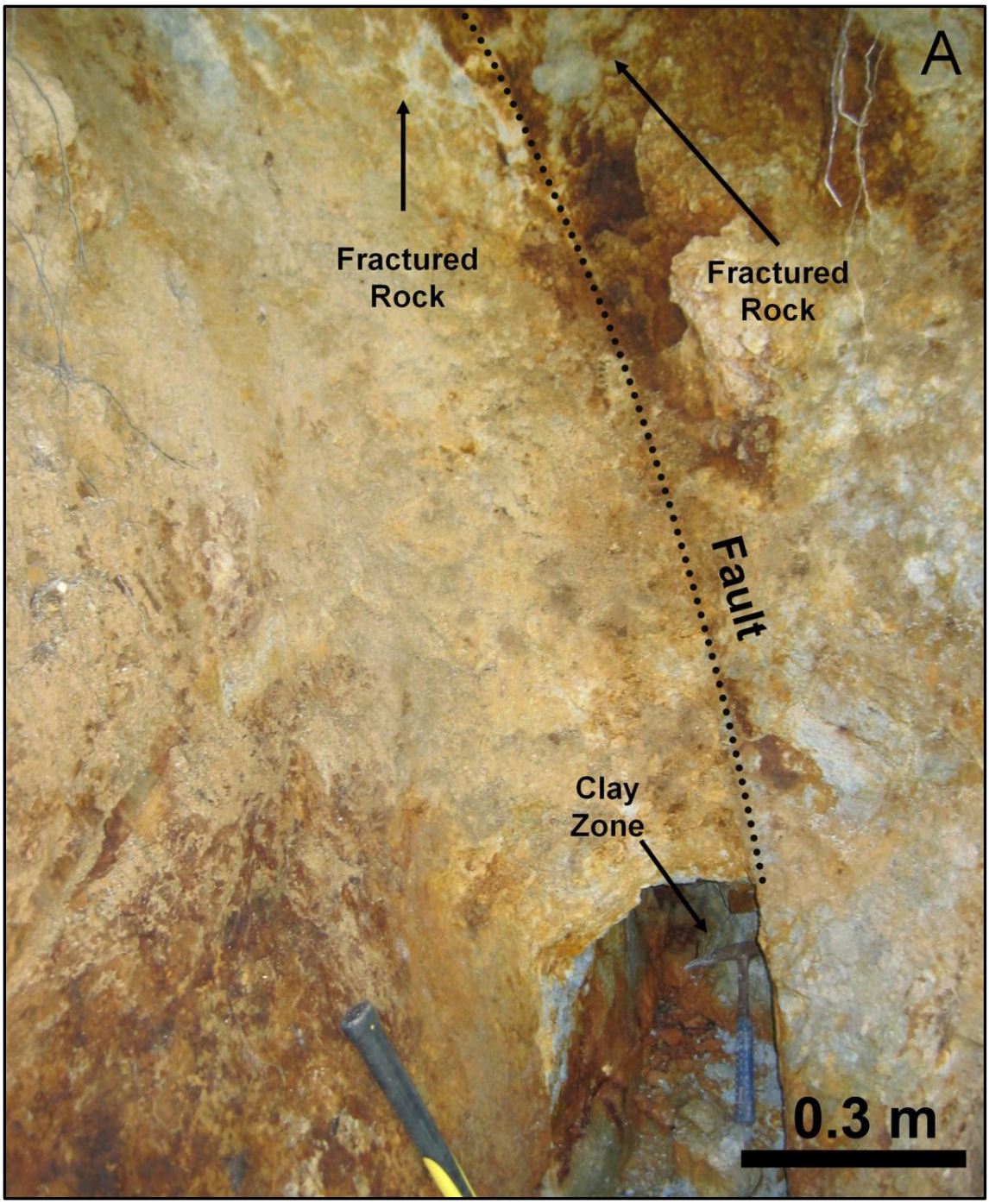

Figure 3.8 A.

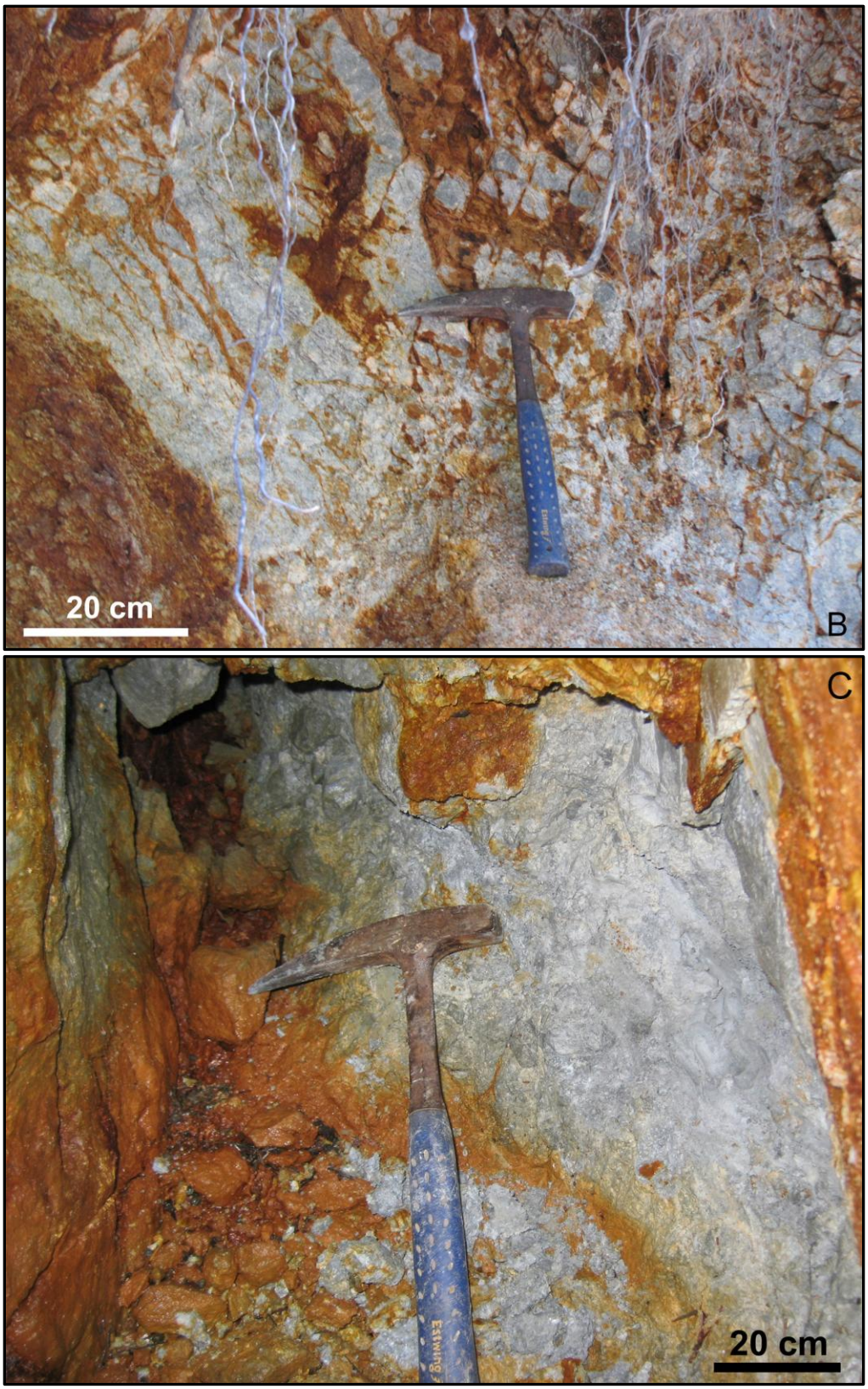

Figure 3.8 B and C.

Figure 3.8.Foster Creek mineralogy. Foster creek clay zone associated with (A) faulting and (B) rock fracturing. (C) Clay alteration along the fault line.

Plagioclase feldspars (7-21%), smectite and kaolinite are present in the Foster Creek samples containing calcite, indicating partial alteration of the parent rock (Reyes, 1990). Areas containing dolomite, I-S (70% illite, R>1), kaolinite and pyrite have low amounts of plagioclase remaining (< 3%), with smectite absent from the mineral assemblages, suggesting higher temperature alteration. Plagioclase feldspars, smectite and kaolinite are not observed in samples F8 and F9, however quartz and I-S levels are elevated, which suggests higher temperature alteration conditions (Table 3.5). Samples from Foster Creek containing carbonates were not antibacterial despite having pyrite concentrations similar to the open pit (4-6% pyrite). However, two samples from Foster Creek without carbonates (F8, F9) were bactericidal (Table 3.5). This suggests that the high pH necessary to stabilize carbonate inhibits the antibacterial process.

Table 3.5. Foster Creek XRD. Results are reported as mineral weight percent (Wt. %). Samples highlighted in blue are bactericidal.

Sample	F1	F2	F3	F4	F5	F6	F7	**F8**	**F9**
Quartz	31	36.7	33.5	21.4	30.4	39	38.1	**40.5**	**42.3**
Plagioclase	7.3	20.7	6.7	9.8	0.5	2.8			
Calcite	4.3	1.0	3.6	10.8					
Dolomite					17.3	2.4	3.2		
Pyrite	4.3	3.7	4.8	0.8	3.4	5.5	6.2	**4.7**	**4.3**
Gypsum					1.7	1.9	2.9	**1.8**	**1.1**
Jarosite								**1.1**	
Kaolinite	1.9	1.5	3.5	7.5	5.5	3.7			
Smectite	21.3	12.5	41.9	48.9					
I-S >70%	26.9	24.8			38.8	44.9	46.9	**49.3**	**46.6**

3.3.6 Road Cut Mineralogy

A large clay alteration zone (> 5 m) SW of Foster Creek was also identified. A cross section of the zone was sampled (4.5 meters) to gauge the mineral alteration from the rock wall into the clay zone (Fig. 3.9).

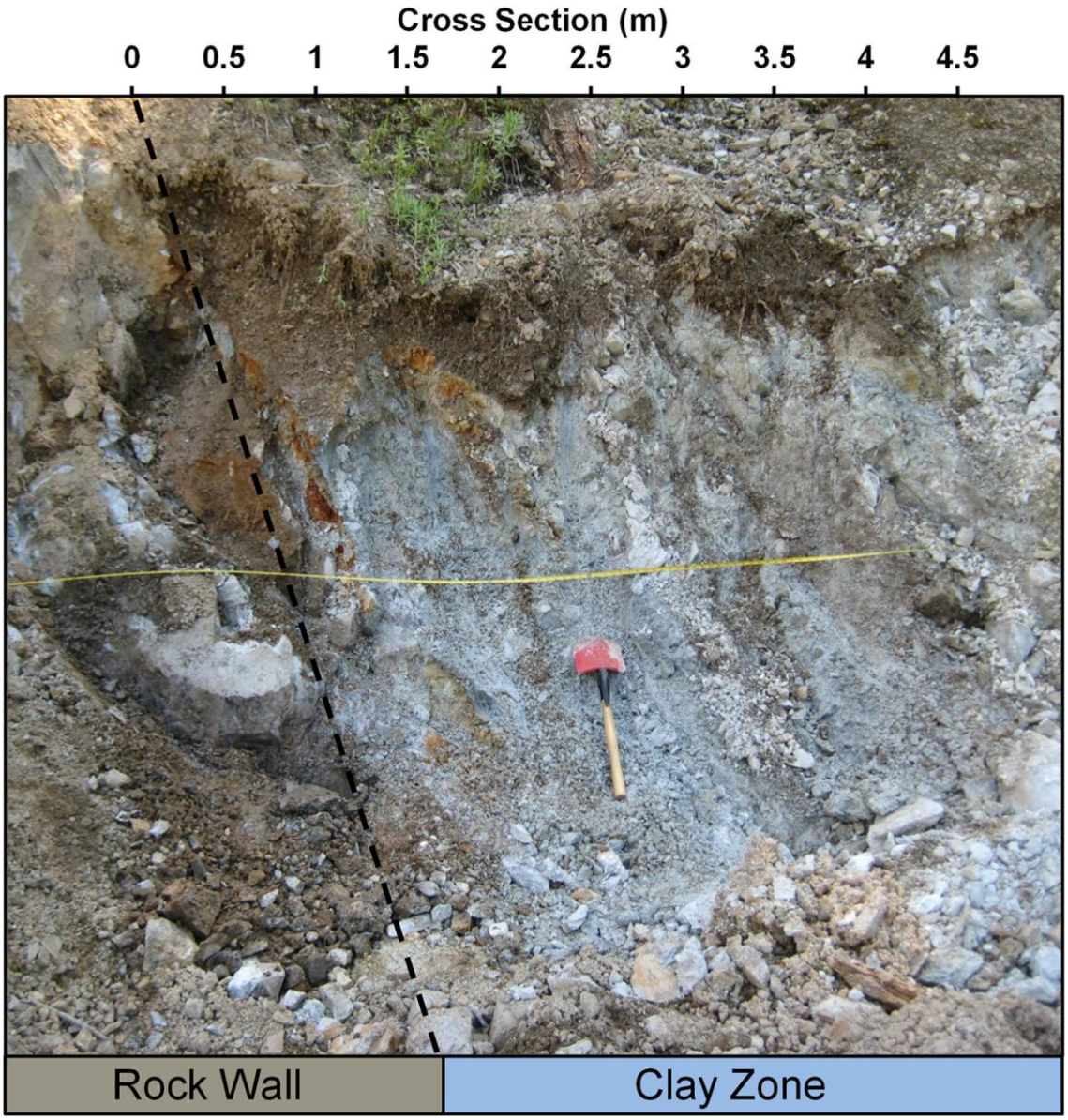

Figure 3.9. Road Cut mineralogy. A 4.5 meter cross section of the clay zone was sampled at 0.5 m increments across the yellow tape measure line.

The alteration minerals present in this zone are calcite, I-S R3 (85% illite), kaolinite and pyrite (Table 3.6). The altered rock wall contained plagioclase feldspar (17%) reflecting incomplete alteration of the parent rock. Calcite and kaolinite abundances increase with distance from the rock wall and intermittent zones of increased pyrite and I-S occur at 2 and 4 meter distances (Fig. 3.9; Table 3.6). No antibacterial activity was observed in samples containing calcite and kaolinite. One sample from the clay vein did inhibit bacterial growth (sample C4) and contained 4.8 % pyrite with no calcite (Table 3.6). Carbonates may buffer solution pH to neutral and alkaline levels, lowering pyrite oxidation rates and metal solubility in these zones, thereby eliminating antibacterial activity.

Table 3.6. Road Cut XRD. Results are reported as mineral weight percent (Wt. %). Highlighted sample (C4) inhibited bacterial growth.

	Cross section (0-4.5 meters)								
Sample	C1	C2	C3	C4	C5	C6	C7	C8	C9
Section (m)	0	0.5	1.0	2.0	2.5	3.0	3.5	4.0	4.5
Quartz	40.6	44.6	36.5	38.1	47.2	45.0	45.6	54.3	50.7
Plagioclase	19.5								
Calcite	2.5	11.3	5.7		3.2	8.9	9.7	3.0	
Pyrite		0.4	3.0	4.8	1.0			1.2	1.3
Gypsum			1.6	1.5	0.3				
Kaolinite	3.4	16.8	6.3		17.4	13.4	12.8	8.0	13.3
I-S > 70%	29.3	24.1	45.3	49.8	29.6	28.1	27.9	33.5	30.8

3.3.7 Oxygen Isotope Fractionation in Quartz

Quartz is not a component of basaltic and andesitic rocks, yet the clay alteration zones contain abundant secondary quartz. The oxygen isotopic composition of quartz in the altered zones should reflect whether the hydrothermal fluids were magmatic (isotopically heavy) or meteoric (isotopically light), and could help in constraining the alteration temperatures (Beaty and Hugh, 1988; Hervig et al., 1995; Taylor and Huston, 1998; Bindeman, 2008). The oxygen isotopic content of quartz from the sulfur mine and open pit blue and white zones were measured (Fig. 3.10 A). All oxygen isotope values are expressed in standard delta notation (δ) with permil (‰) units (see Chapter 7 Methods for more detail) (Barnes, 1997).

The Sulfur Mine quartz $\delta^{18}O$ values range from 21-25 ‰, suggestive of greater magmatic water input. The Open Pit blue zone had lower $\delta^{18}O$ values (12-16 ‰) indicating mixing between meteoric and magmatic fluids. The lowest $\delta^{18}O$ values were measured in the open pit oxidized white zone (4-6 ‰), signifying meteoric fluids (Fig. 3.10 A). The interpretation of the quartz $\delta^{18}O$ values is dependent on both the water oxygen isotope composition and temperature of mineralization. Using the mineralogical constraints discussed above, the relative temperatures of each zone can be estimated. Then the quartz-water $\delta^{18}O$ fractionation equation (Matthews and, 1979) can be used to constrain the water composition.

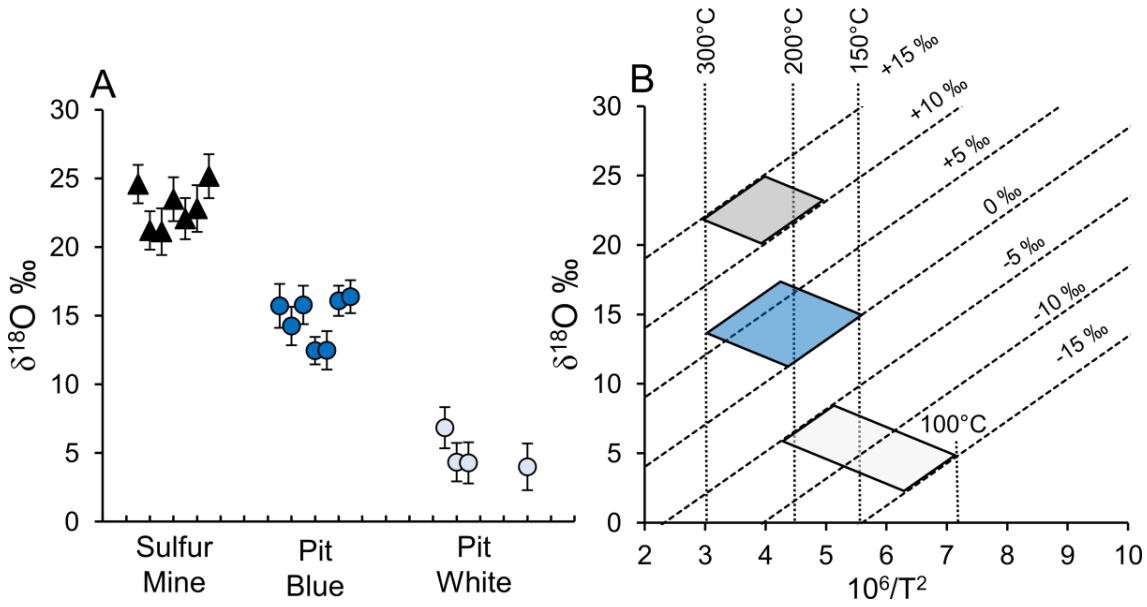

Figure 3.10. Quartz thermal history. (A) $\delta^{18}O$ values measured in quartz from the Sulfur Mine (black clay) and Open Pit blue and white clay zones. (B) Temperature ranges for quartz crystallization constrained by quartz-water isotopic fraction lines with different water compositions (+15 to -15 ‰) and an upper limit of 300°C.

Quartz formation temperature estimates were determined using constraints from the observed mineral assemblages using a range of potential alteration fluid $\delta^{18}O$ values (Clayton et al., 1972; Matthews and Beckinsale, 1979; Bindeman, 2008; Tanner et al., 2015). In the open pit, the absence of end member illite, which is stable at 300˚C, suggests that temperatures must have been below this limit assuming equilibrium. (Velde, 1995; Meunier, 2005). Primary magmatic fluids have isotopically heavy $\delta^{18}O$ values that range from +5‰ to +9‰ (Bindeman, 2008; Tanner et al., 2015). Their oxygen isotopic composition is restricted by elevated temperatures (700°-1100°C) and the igneous rocks they are intruding (+5-6‰ for basalts and andesites) (Barnes, 1997; Bindeman, 2008). Hydrothermal fluids dominated by magmatic fluids can reach $\delta^{18}O$ values over +15‰

from isotopic exchange with rock at elevated temperature (> 300°C) and boiling, which enriches the fluids in ^{18}O (Beaty and Hugh, 1988; Taylor and Huston, 1998; Barnes, 1997). Meteoric waters are depleted in ^{18}O as their source is mainly rainwater, which is enriched in the lighter ^{16}O isotopes (Barnes, 1997). Meteoric waters have low $\delta^{18}O$ (-40 to 0‰) values that reflect the mean annual temperature, latitude and elevation of the rain and snow fall generating these waters (Craig, 1961). As warmer subtropical ocean waters evaporate they become enriched in ^{16}O due to ^{18}O remaining in the residual water. This ^{16}O enrichment increases as water vapor reaches more northern latitudes and higher elevations, due to Rayleigh fractionation, where cold air enhances ^{18}O precipitation, progressively lowering meteoric $\delta^{18}O$ values (Craig, 1961). Modern meteoric $\delta^{18}O$ values in the Cascade arc range from -8 to -15‰, however meteoric water compositions estimated from fossil horse teeth dated over the last 30Ma were heavier (-5 to -10‰) (Kohn et al., 2002).

The Sulfur Mine black clay zone contained elevated pyrite (18%), kaolinite and S^0, which form from high-sulfidation, acidic, magmatic fluids at temperatures < 300°C (Hedenquist and Lowenstern, 1994) based on the mineralogical assemblage. For the Sulfur Mine a minimum fluid composition of +10‰ ($\delta^{18}O$) was modeled (Fig. 3.10), supporting the higher temperature magmatic hydrothermal alteration. In the Open Pit, the lower pyrite levels and pervasive rectorite reflects low-sulfidation alteration, characterized by low fluid flow and mixing of magmatic and meteoric fluids (Hedenquist and Lowenstern, 1994; Pirajno, 2009). The temperature stability range of rectorite is between 150-200˚C, which places the $\delta^{18}O$ fluid compositions in the Open Pit between 0 and +5‰ in the blue clay. The white zones containing smectite suggest temperatures

below 150˚C, consistent with meteoric waters in the range of -5‰ (at 30Ma; Kohn et al., 2002) to -15‰ (present day) (Fig. 3.10 B).

The minimum temperatures for quartz formation are shown in Figure 3.10 B using the quartz-water oxygen fractionation equation from Matthews and Beckinsale, 1979 (see Appendix B for calculations). Quartz-water fractionation lines were calculated using $\delta^{18}O$ water values from (-15 to +15‰) and plotted against the measured quartz $\delta^{18}O$ values to show the theoretical temperature ranges and fluid sources that formed the Open Pit and Sulfur Mine clay zones (Fig. 3.10 B). The positive $\delta^{18}O$ values of quartz from the Sulfur Mine suggest a minimum quartz formation temperature of ~180°C with +10‰ alteration fluids (Fig. 3.10 B, Appendix B). If +5‰ to 0‰ waters formed the blue zones in the open pit, the minimum alteration temperature would be ~150°C. The low quartz $\delta^{18}O$ values (4-6‰) in the Open Pit white zone suggest a meteoric fluids with a minimum temperature of ~99°C, if these zones formed from meteoric waters ranging from -5‰ to -15‰, as 0‰ waters would require temperatures above 300°C.

3.4 Discussion

3.4.1 Hydrothermal Formation of the OMT Deposit

The alteration minerals formed in the parent rock samples are characteristic of low temperature alkaline (Ca-series) hydrothermal alteration at neutral pH. Parent rocks from the Foster Creek and Road Cut sites contain zeolites associated with low temperature alteration (<100°C), while the Open Pit parent rock mineral assemblage reflects hydrothermal alteration temperatures around ~120-150°C (Figs. 3.4 and 3.11). The Sulfur Mine parent rock XRD pattern contained only plagioclase feldspar, which

suggests little or no hydrothermal alteration occurred in some areas. The lower temperature alteration of the parent rocks associated with the Sulfur Mine, Foster Creek and Road Cut sites may reflect a more short lived higher temperature event associated with faults and fractures with higher fluid flows (Velde, 1997; Meunier, 2005).

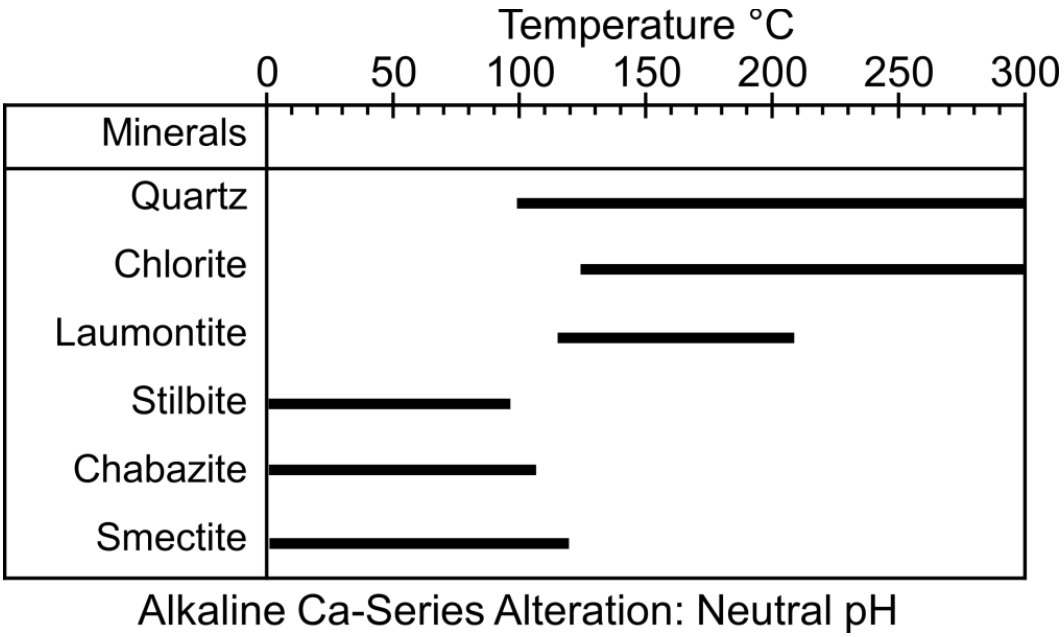

Figure 3.11. Parent rock alteration temperatures. Temperature stability ranges for parent rock alteration minerals (Reyes, 1990; Velde, 1995).

The clay zones in the Open Pit are characteristic of argillic alteration with low sulfidation fluids (Table 3.1). The Open Pit has a series of NW-SE faults where white clay zones cut through the blue zone. Slickensides are found in this white zone which suggests that the faulting in the Open Pit occurred after the hydrothermal alteration, providing a path for meteoric water to oxidize and leach elements from these zones (3.12). Rectorite was pervasive in the open pit with pyrite concentrations in the blue clay

zone ranging from 4-6%. Rectorite can form at temperatures up to 200°C, where more illitic I-S (70-80% illite) normally starts to appear (Velde, 1995; Meunier, 2005). The uniform R1 ordering may give rectorite a greater temperature stability range compared to I-S with lower illite content (Velde, 1995). Low-sulfidation epithermal systems are associated with low fluid flow and near neutral pH reducing environments (Hedenquist and Lowenstern, 1994; Pirajno, 2009). The quartz $\delta^{18}O$ values in the open pit blue zone (+12-16 ‰) suggest a mixture of magmatic and meteoric fluids with a constant heat source (150°C-200°C) provided the conditions for rectorite formation.

Figure 3.12. Fault zone slickenside. Picture of slickensides from the Open Pit white clay zones associated with faulting.

A stockwork of non-directional quartz-pyrite veins run through the blue clay zone in the Open Pit that may have formed from hydraulic fracturing of the altering rock. Quartz veins are typically observed at higher pressures (> 3 kbar) and temperatures > 300°C outside of the epithermal temperature and pressure range (Bons, 2001). As rocks are hydrofractured, fluids rapidly ascend through the fracture network. As temperatures decrease, SiO_2 solubility also decreases and quartz veins are deposited (Bons, 2001; Pirajo, 2009). Precipitation of quartz veins has therefore been associated with alteration at greater depth, closer to the heat source, excluding many epithermal systems (Bons, 2001; Pirajno, 2009). However a study by Bons (2001) found that rapid transport of silica-bearing fluids (up to 1 m/s) through hydrofractured systems can produce quartz veins at shallow crustal depths. The high fluid transport speeds do not allow significant cooling and precipitation to occur until fluid transport is halted by a capping zone (Bons, 2001). The quartz veins observed in the open pit contain fine disseminated pyrite (> 9%) that filled the fractured andesitic parent rock. The precipitation of these quartz-pyrite veins may be a combination of steady, low-temperature alteration with periods of rapidly ascending SiO_2-rich fluids due to changes in fluid pressure and fracturing. As the fluids rapidly ascended through the low-sulfidation alteration zone and cooled, H_2S and Fe^{2+} in the fluids, would precipitate pyrite in higher concentrations (> 9%) than in the altered andesite (4-5%).

The mineral alterations observed in the Foster Creek and Road Cut sites (kaolinite, smectite, I-S R>1, pyrite and carbonate) reflect intermediate argillic alteration with an intermediate sulfidation state and temperatures below 300°C (Table 3.1). The presence of kaolinite, I-S R>1 (> 70% illite) and pyrite in these areas suggests a short

lived alteration event with higher temperature moderately acidic fluids (< 250°; Reyes, 1990), possibly associated with faulting, formed the initial clay zones. Carbonates would precipitate as temperatures decreased and fluids containing Ca and Mg (leached from the parent rock) increased pH during mixing with meteoric water. The late precipitation of carbonates has been observed in similar hydrothermal systems (Keith and Bargar, 1988; Bargar and Keith, 1999).

The precipitation of S^0 in the Sulfur Mine region is associated with high-sulfidation epithermal alteration (Hedenquist and Lowenstern, 1994). The mineral assemblage identified (S^0, pyrite, I-S R>1, kaolinite, smectite and carbonate), indicates intermediate argillic alteration where high-sulfidation fluids formed these zones. The presence of kaolinite and carbonates suggests formation conditions similar to the Foster Creek clay zones, with late precipitation of carbonates after the initial higher temperature acidic alteration. Oxygen isotopes from quartz in the Sulfur Mine reveal a dominantly magmatic fluid source. This high sulfidation SO_2 rich fluid would disproportionate into H_2SO_4 and H_2S at elevated temperature (250°-280°C) as it ascended through rock fractures (Delmelle et al., 2000; Pirajno, 2009). However, reducing conditions were likely maintained as indicated by the high levels of pyrite.

The precipitation of S^0 at atmospheric pressure is limited to temperatures < 115°C (Barnes, 1997). However, increased pressure occurs when heated fluids are blocked by an impermeable layer (e.g., clay), generating supralithostatic pressure (2-6 kbar) at temperatures up to 300°C (Bons, 2001; Pirajno, 2009, Naumov et al., 2015). This increase in pressure can extend the temperature range for S^0 crystallization to temperatures ~150°-200°C at ~2-6 kbar pressure (Susse et al., 1966; Barnes, 1997). The

following reactions among H_2S, SO_2, H_2SO_4 and O_2 can lead to the formation of S^0 (Delmelle et al., 2000):

$$H_2SO_4 + 3\ H_2S \rightarrow 4\ S^0 + 4\ H_2O \quad (1)$$

$$SO_2 + 2\ H_2S \rightarrow 3\ S^0 + 2\ H_2O \quad (2)$$

$$O_2 + 2\ H_2S \rightarrow 2\ S^0 + 2\ H_2O \quad (3)$$

The formation of I-S due to hydrothermal alteration can take place in a geologically short time span (10-10,000 years) depending on the temperature and fluid chemistry (Meunier, 2005). Estimates for the formation of I-S (> 80% illite) suggest that this process can occur in as little as 10 years when temperatures are 250°C (Meunier, 2005). At 150°C this process can take on the order of 10,000 years to occur (Meunier, 2005). The pervasive nature of rectorite in the Open Pit, along with quartz $\delta^{18}O$ values (+12-16 ‰), suggests that a mixture of magmatic and meteoric fluids resulted in low-sulfidation, neutral pH alteration through a more stable conduction heat source (Fig. 3.13 A). The Sulfur Mine, Foster Creek and Road Cut clay zones, associated with faulting, may have formed more rapidly at higher temperatures with a convection heat source that transported higher temperature magmatic fluids through the faulted and fractured rock. (Fig. 3.13 B).

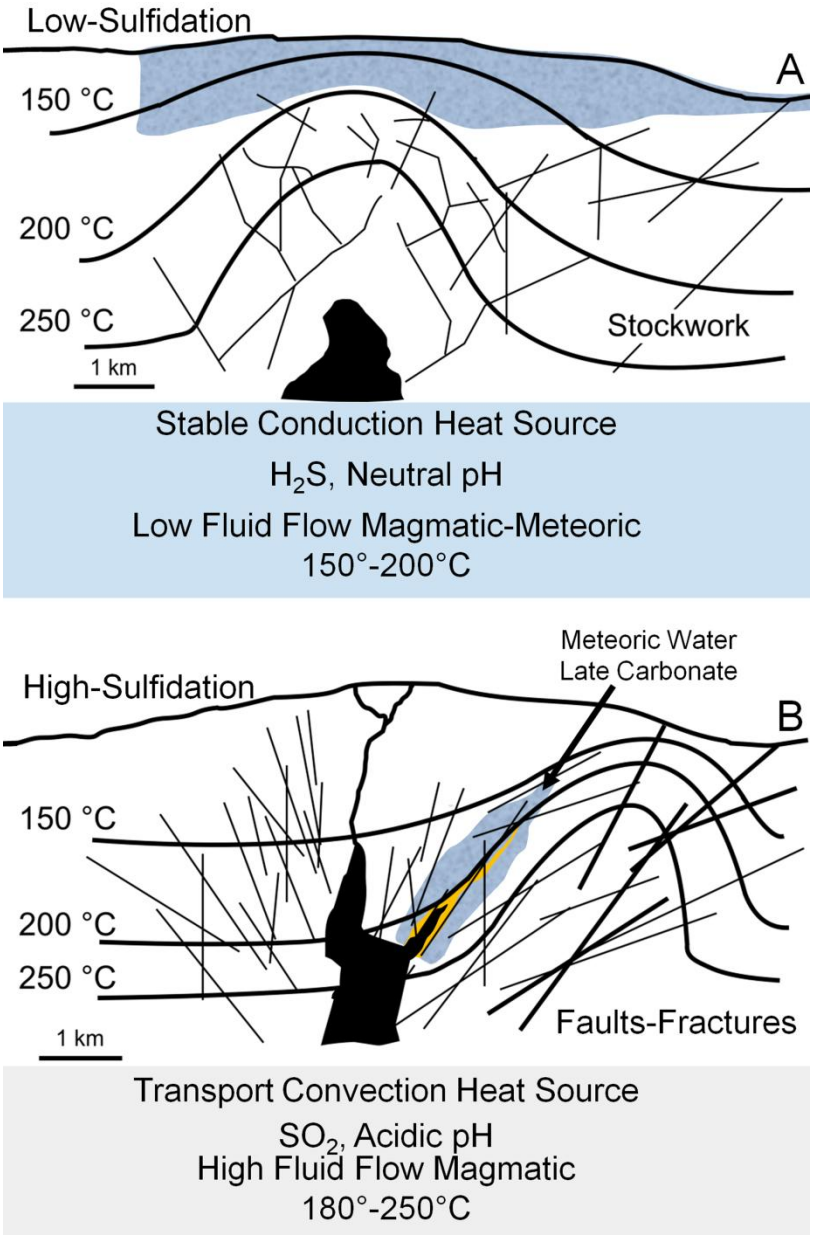

Figure 3.13. Hydrothermal alteration conditions. (A) Open pit mine hydrothermal alteration from a low-sulfidation, conduction heat system at temperatures < 200°C. Secondary alteration minerals (I-S, pyrite, quartz) form a capping layer, resulting in increased pressures, hydraulic fracturing and precipitation of quartz-pyrite stockwork veins. (B) Sulfur mine alteration from a high-sulfidation, convection heat system at temperatures < 250°C. Faults and fractures in the parent rock transport hot magmatic fluids, causing an initial higher temperature acidic alteration. Carbonates precipitate as a late mineral phase when temperatures decreased and high-sulfidation fluids were neutralized by the parent rock and meteoric water.

3.4.2 Mineralogical Variables and Antibacterial Activity

The antibacterial susceptibility testing of clay alteration zones in the OMT deposit indicates that a specific mineral assemblage does not consistently dictate antibacterial effectiveness (Tables 3.3 to 3.6). The majority of antibacterial samples in the deposit contained pyrite, with the most antibacterial samples in the Open Pit and Sulfur Mine zones. Oxidized white zones in the Open Pit contained no pyrite, however still inhibited bacterial growth. The Open Pit red zones also contained no pyrite, but were not antibacterial. Goethite was identified in the red zone which forms as a secondary mineral phase due to pyrite oxidation. Almost all the clay zones sampled at the Foster Creek and Road Cut sites were not antibacterial despite having pyrite concentrations (4-5%) similar to the open pit mine. The presence of carbonates in these zones may be responsible for the lowered the antibacterial activity, potentially increasing pH and lowering pyrite oxidation rates and metal solubility.

The oxidation of pyrite at neutral to alkaline pH is driven by dissolved O_2 (Moses and Herman, 1991; Evangelou, 1995). At these pH levels Fe-oxides form on pyrite surfaces, lowering oxidation rates (Evangelou, 1995). The release of soluble metals from OMT clays appears to be the driving force behind their antibacterial activity (Williams et al., 2011; Morrison et al., 2014). Previous studies of the OMT clays showed that samples with low pH (< 4) are antibacterial and release mM levels of soluble Fe^{2+}, Fe^{3+}, Al^{3+} and Ca^{2+} (Williams et al., 2011; Morrison et al., 2014). Pyrite oxidation at low pH (< 4) is driven by soluble Fe^{3+} (Moses and Herman, 1991; Evangelou, 1995). The acidic pH lowers the buildup of Fe-oxide coatings on pyrite, which inhibit oxidation. This caveat in

pyrite oxidation may explain the lowered antibacterial activity in zones containing mixtures of pyrite and carbonate.

The antibacterial white zones in the Open Pit contain no detectable pyrite, suggesting that the antibacterial activity of the OMT clays is not strictly a function of pyrite content (Table. 3.3). Mineral dissolution along with the exchange of cations in expandable clays apparently plays a role in the antibacterial activity in these zones (Morrison et al., 2014). The I-S found throughout the deposit contains expandable smectite layers capable of exchanging cations (Meunier, 2005). The cation exchange capacity (CEC) of I-S clays varies from ~20-60 meq/100g (milliequivalents of charge), which provides an exchange capacity of 10-30 mM/100g for divalent cations (e.g., Fe^{2+} and Ca^{2+}; Meunier, 2005). Therefore the CEC of the clay minerals in the OMT deposit could be playing an important role in the antibacterial process. From these results it is clear that the bulk mineralogy of clay zones in the OMT deposit is only part of the antibacterial effectiveness. Moreover, the pH and oxidation state of the mineral assemblage are critical to the antibacterial reactions.

3.5 Conclusions

The OMT deposit formed from the hydrothermal alteration of volcanic rocks with basaltic to andesitic composition. The mineral assemblages that formed are characteristic of intermediate argillic alteration. Low-sulfidation hydrothermal fluids formed the clays in the Open Pit mine, with high-sulfidation alteration associated with the Sulfur Mine. Intermediate-sulfidation fluids likely formed the Foster Creek and Road Cut clay zones. The pervasive nature of rectorite in the Open Pit and quartz $\delta^{18}O$ values suggest a

constant heat source (150°-200°C) with mixing magmatic and meteoric waters. The other clay zones sampled contained I-S with higher illite layers (70-80%), pyrite, kaolinite and carbonate. The more acidic fluids associated with intermediate to high-sulfidation alteration promote Al solubility and kaolinite formation. The alteration in these zones was likely brief compared to the Open Pit as indicated by the presence of carbonates, which require pH neutralization from Ca and Mg dissolution in the parent rock. Carbonates therefore represent a late phase mineralization event as fluids cooled, after the initial high temperature acidic alteration event.

Antibacterial susceptibility testing indicates that pyrite is not the only mineralogical variable that produces the observed bactericide. The red oxidized zone in the Open Pit contained goethite from the oxidation of pyrite and it was not antibacterial, suggesting that the oxidation state is too high for antibacterial reactions to occur. The white oxidized zones contained no pyrite but still inhibited bacterial growth. Interlayer cation exchange by expandable clay minerals along with mineral dissolution may be playing a role in the open pit white zones. The reduced blue clay zone in the Open Pit showed decreasing antibacterial effectiveness with depth. The most bactericidal samples were found at the interface of the blue and white oxidized zones. Jarosite appears in the bactericidal samples from the blue zone which may reflect a transition to more oxidizing conditions in this zone. The Sulfur Mine clay zones showed the highest antibacterial activity and contained elevated pyrite concentrations (10-18%) resulting in bactericidal activity. Samples containing pyrite (4-6%) and carbonates showed no antibacterial activity, likely due to increases in pH that lowered pyrite oxidation rates.

The results from this study represent the first attempt to identify the hydrothermal processes that generate antibacterial clay deposits, opening the potential for a new economic geology and use for argillic alteration zones that are often considered to be overburden during ore exploration. However the findings presented here indicate that the antibacterial activity of such clay deposits is not a simple relation between mineralogy and antibacterial activity. The antibacterial activity of the rehydrated clays is also influenced by pH, Eh, metal speciation and mineral reactivity, as shown by the detailed investigation into the antibacterial mechanism presented in Chapters 4 and 5. Next we will explore the geochemical factors that influence the antibacterial activity, in the context of the observed mineralogy.

Chapter 4

GEOCHEMISTRY AND ANTIBACTERIAL ACTIVITY

4.1 Introduction

The previous chapter investigated the mineralogy and hydrothermal alteration conditions that formed the OMT clay deposit. The antibacterial activity of clay alteration zones was examined and compared with the mineralogy to determine if a distinct mineral assemblage was antibacterial throughout the deposit. The antibacterial activity in the alteration zones correlated broadly with the hydrothermal alteration conditions. High-sulfidation clay zones in the Sulfur Mine with elevated pyrite (10-18%) showed the greatest antibacterial activity, while low sulfidation blue clay zones in the Open Pit (4-6 % pyrite) showed variable antibacterial activity. The white zones in the Open Pit contained no measurable pyrite but still inhibited bacterial growth, making interlayer cation exchange with expandable clay minerals a possible source of their antibacterial activity. Throughout the deposit samples containing carbonates in addition to pyrite were not antibacterial. These results suggest that pyrite alone does not explain all of the observed antibacterial activity.

The goal of this chapter is to determine the mineralogical and geochemical variables that influence the antibacterial activity observed in each alteration zone, providing critical mineralogical and geochemical constraints that can be used to identifying future antibacterial deposits. This will be achieved by exploring the differences in mineralogy, leachate chemistry, metal speciation, redox state and cation exchange capacity as they relate to antibacterial activity.

4.2 Results

4.2.1 Antibacterial Activity and Leachate Chemistry

The general trends in antibacterial activity of the OMT deposit are summarized in Figure 4.1. Antibacterial zones of inhibition were measured on *E. coli* ATCC 25922 and *S. epidermidis* ATCC 14990 using the agar diffusion method along with spot plate counts to determine inhibitory or bactericidal activity (see Chapter 7 Methods). The antibacterial activity is linked to solution pH which controls metal solubility and hydrogen peroxide generation (Fig. 4.1). Bactericidal samples have pH values < 4.2, with Fe^{2+}, Fe^{3+} and Al^{3+} concentrations over 1 mM. The most antibacterial samples are from the Sulfur Mine location, which is associated with high sulfidation alteration, elevated pyrite (10-18%) and I-S (70% I) R > 1, producing zones of inhibition > 17 mm (Fig. 4.1 A and B). The Open Pit blue clays contain lower pyrite contents (4-6%) that produce zones of inhibition up to 8 mm and 16 mm for *E. coli* and *S. epidermidis*, respectively. Samples from the white oxidized zone inhibited bacterial growth when tested by plate counting but did not produce a zone of inhibition in the disk diffusion test. These samples released lower concentrations of metals (< 1 mM) with pH values ranging from 4.2-4.7. As pH levels rise above 4.2 metal and hydrogen peroxide concentrations steadily decline until bacterial growth is not affected above pH 4.7 (Fig. 4.1).

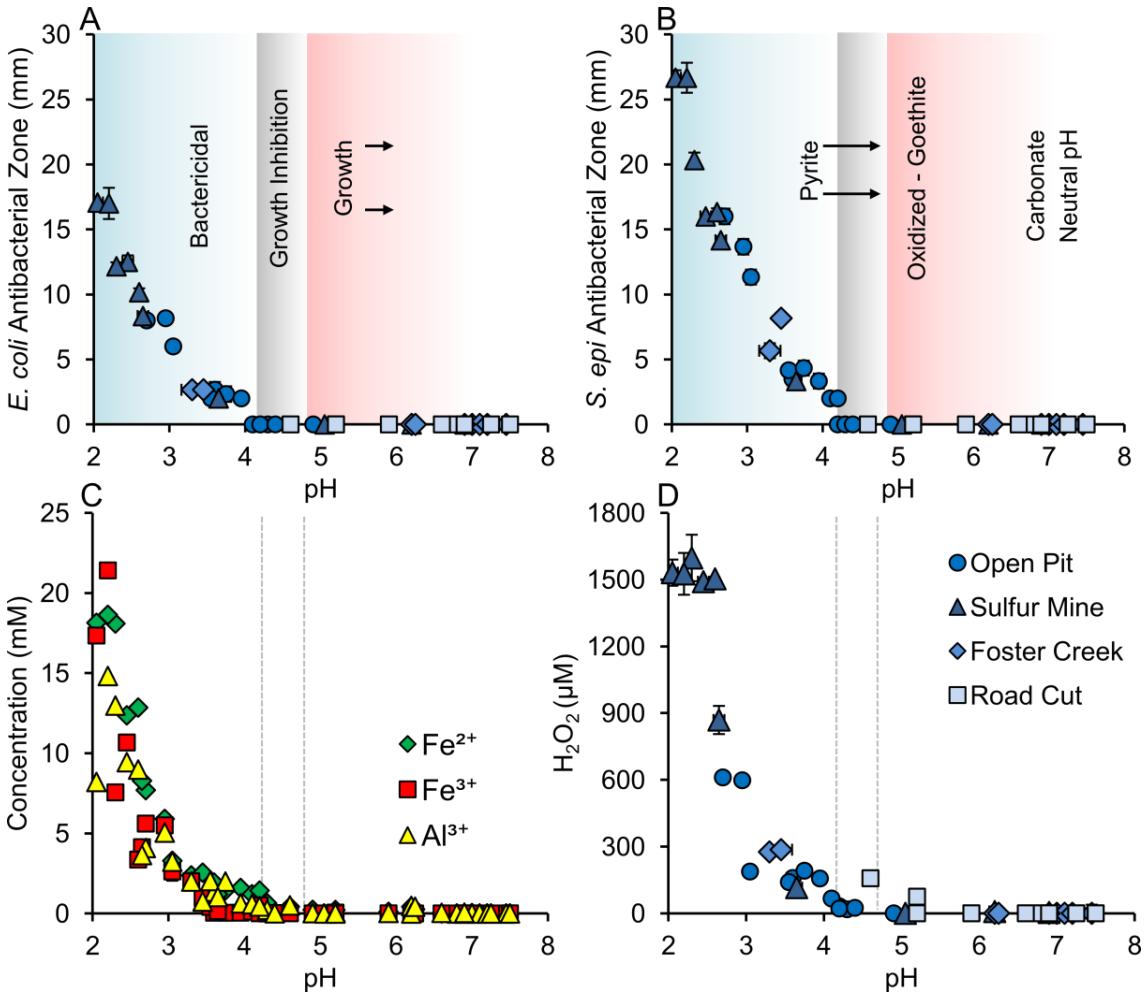

Figure 4.1. Trends in antibacterial activity. Antibacterial susceptibility testing of (A) *E. coli* and (B) *S. epidermidis* (disk diffusion method) vs. pH. The shaded areas correspond to antibacterial effectiveness with; bactericidal (blue), growth inhibition (grey) and normal growth (red). (C) Metal and (D) hydrogen peroxide concentrations vs. pH. The dashed lines correspond to the shaded antibacterial effectiveness regions in A and B.

Non-antibacterial samples fall into two categories, oxidized and carbonate buffered. Oxidized red samples from the Open Pit contain goethite, which formed from the oxidation of pyrite. The Foster Creek and Road Cut sampling sites contain calcite and dolomite, which buffer solution pH (~ 7), preventing the release of metals. Antibacterial

susceptibility testing against antibiotic resistant strains of model bacteria (*E. coli* ATCC 35218 and *S. epidermidis* ATCC 35948) produced similar results (Appendix C, Fig. 4.8).

Table 4.1 compares the elements released by clays in the Open Pit and Sulfur Mine. pH and Eh measurements were measured on 100mg/ml mineral suspensions after 24 hrs. Bactericidal samples from the Open Pit blue zone have lower pH (< 4.2) and release > 1 mM Fe^{2+}, Fe^{3+} and Al^{3+}. The Open Pit white zone (P2) contained no measurable pyrite but still released Fe and Al at low pH (4.2) (Tables 4.1 and 3.3). Exchangeable cations from smectite interlayers or dissolution of smectite layers may be the source of these elements. The oxidized red clay zone from the Open Pit (P1) released the lowest amounts of metals with no measurable Fe^{2+}, due to the high oxidation state of the mineral assemblage. Williams et al., (2011) measured the chemistry of the anions in the OMT blue clay leachates and found that sulfate was the major ion species due to the oxidation of pyrite.

Samples from the Sulfur Mine released the highest amounts of Fe and Al with more acidic pH values (2.1-2.7) (Table 4.1). The black sulfide-rich clay in sample S4 contained over 18% pyrite that produced the acidic pH (2.1), high metal content of these leachates. Samples from the sulfur mine with lower pyrite concentrations (~ 5%) released lower amounts of Fe and Al higher pH (2.7) (Table 4.1). The bactericidal samples from the open pit and sulfur mine have low pH (< 3) and high Eh (> 500 mV) values (Table 4.1).

Table 4.1. Open Pit and Sulfur Mine leachate chemistry. Elemental analyses of mineral leachates. All values are reported at micro-molar (µM) concentrations. Elements <1nM are listed as below detection limit (BDL). The main elements released by the clays are highlighted in gray.

	Open Pit			Sulfur Mine	
Element	Blue (P4)	White (P2)	Red (P1)	Black(S4)	Blue (S6)
Na	34.2	39.1	43.4	239.9	193.3
Mg	749.2	274.3	13.8	660.1	1114.1
Al	4599.8	456.3	54.4	8208.0	3646.9
P	233.3	1.7	1.20	96.1	19.5
K	0.7	44.2	11.8	198.2	65.2
Ca	3933.7	11176.1	35.8	523.1	1734.5
Ti	0.2	0.28	2.81E-02	0.3	0.1
V	1.3	4.73E-03	2.67E-02	7.8	16.8
Cr	0.8	0.12	1.15E-02	5.5	4.4
Mn	30.0	11.8	0.19	120.2	239.7
Fe^{2+}	5885.2	224.8	0.0	18137.5	8283.9
Fe^{3+}	5456.3	504.2	11.9	17134.2	4136.0
Co	6.5	0.40	2.75E-3	21.2	7.5
Ni	8.3	0.38	8.67E-3	30.1	13.1
Cu	11.8	1.9	4.27E-2	35.2	13.0
Zn	5.8	2.8	9.57E-2	36.7	31.6
As	1.4	BDL	BDL	1.9	0.2
Se	0.8	4.4E-2	BDL	0.9	0.5
Rb	3.8E-2	6.4E-2	5.85E-3	0.2	3.7E-2
Sr	18.0	7.9	0.15	6.2	12.3
Mo	0.1	2.6E-2	2.49E-03	0.1	3.2E-2
Cd	8.0E-3	1.6E-3	BDL	0.2	0.4
Cs	2.1E-2	5.8E-3	2.34E-03	---	---
Ba	1.6E-2	1.1E-1	1.34E-02	0.4	0.1
Hf	BDL	BDL	BDL	BDL	BDL
W	1.6E-3	BDL	BDL	1.6E-03	---
Ag	BDL	BDL	BDL	---	---
Hg	BDL	BDL	BDL	---	---
Pb	BDL	BDL	BDL	---	---
U	2.3E-03	BDL	BDL	---	---
pH	2.9 ± 0.1	4.2 ± 0	6.8 ± 0	2.0 ± 0.1	2.7 ± 0.1
Eh (mV)	611 ± 1.3	443 ± 1.5	349 ± 10.1	724 ± 0.4	594 ± 15.0

Note: relative standard deviations for elemental analysis were <7.0 %

Carbonates were present in the majority of the samples from the Foster Creek and Road Cut sites, which eliminated their antibacterial activity (Tables 3.5 and 3.6) due to increases in pH (Fig. 4.1). The elements leached from antibacterial and non-antibacterial samples from these sites are compared in Table 4.2. Bactericidal samples from Foster Creek (F8, F9) contained ~ 4% pyrite and released ~2 mM Fe^{2+}, Fe^{3+} and Al^{3+} at low pH (3.3). The non-antibacterial clays from Foster Creek, containing carbonate, had near

neutral pH and released only µM concentrations of Fe and Al (Table 4.2). The same trend is observed in the Road Cut samples, however only one sample (C4) inhibited bacterial growth at higher pH (4.2).

Table 4.2. Foster Creek and Road Cut leachates. All values are reported at micro-molar (µM) concentrations. Elements <1nM are listed as below detection limit (BDL). The main elements released by the clays are highlighted in gray.

	Foster Creek		Road Cut Clay	
Element	Blue (F8)	Calcite (F1)	Blue (C4)	Calcite (C3)
Na	62.8	190.2	53.0	435.6
Mg	2509.3	155.2	497.5	384.2
Al	2065.5	1.4	62.9	38.2
P	24.1	5.8	0.7	0.3
K	1.8	96.0	374.7	424.4
Ca	4612.0	1176.2	4775.4	4209.7
Ti	0.1	6.1E-3	2.0E-2	4.4E-3
V	0.2	7.6E-3	BDL	BDL
Cr	0.1	5.9E-3	3.0E-3	1.7E-3
Mn	71.3	2.0	12.8	14.5
Fe^{2+}	2374.9	30.4	422.8	101.9
Fe^{3+}	2010.5	BDL	13.5	7.8
Co	4.3	1.1E-2	3.4	2.7
Ni	4.8	0.1	1.0	0.8
Cu	6.1	0.2	0.7	0.6
Zn	4.6	1.9	5.3	3.8
As	0.1	BDL	1.2E-1	0.2
Se	0.6	7.8E-3	2.9E-2	2.5E-2
Rb	9.8E-3	8.7E-3	9.4E-2	8.9E-2
Sr	7.7	3.3	32.2	35.9
Mo	9.6E-3	1.3E-2	4.1E-03	2.9E-03
Cd	9.5E-3	2.2E-3	9.6E-3	1.0E-2
Cs	7.0E-3	3.0E-3	1.0E-3	BDL
Ba	0.1	0.4	0.5	0.5
Hf	BDL	BDL	BDL	BDL
W	1.6E-3	BDL	4.3E-3	8.3E-2
Ag	BDL	BDL	BDL	BDL
Hg	BDL	BDL	BDL	3.1E-3
Pb	0.4	3.0E-2	0.2	0.1
U	4.1E-03	BDL	3.8E-3	2.9E-3
pH	3.3 ± 0.1	7.0 ± 0	4.2 ± 0.1	5.3 ± 0.1
Eh (mV)	520 ± 3.3	368 ± 1.6	408 ± 6.7	367 ± 2.1

Note: relative standard deviations for elemental analysis were <7.0 %

Changes in antibacterial activity due to increases in pH from carbonate buffering are shown in Figure 4.2. Samples from the Sulfur Mine show a positive correlation between pyrite concentrations, hydrogen peroxide levels and antibacterial activity (Fig. 4.2 A and B). The Open Pit clays have relatively uniform pyrite levels and do not show a correlation between antibacterial activity and pyrite concentration. Samples from the Sulfur Mine resulted in decreasing pH values as pyrite levels increase, however samples from the other sites show a broad range in pH values (pH 3-7) despite having similar pyrite concentrations (~ 5%) (Fig. 4.2 C). These increases in pH correlate with the total amount of carbonate present in the sample, with high carbonate levels buffering solutions to near neutral pH (Fig. 4.2 D).

These results indicate that the pH, Eh, solubility and toxicity of metals leached from the OMT clays are linked to their antibacterial activity. As Fe^{2+} oxidizes to Fe^{3+} the ionic radius decreases while charge increases. This promotes hydrolysis reactions forming insoluble Fe-oxyhydroxides that precipitate out of solution (Pearson, 1966). Ferric iron and aluminum have low pKa values (acid hydrolysis equilibrium) (2.2 and 4.5 respectively), which limits their solubility to these pH ranges (Pearson, 1966).

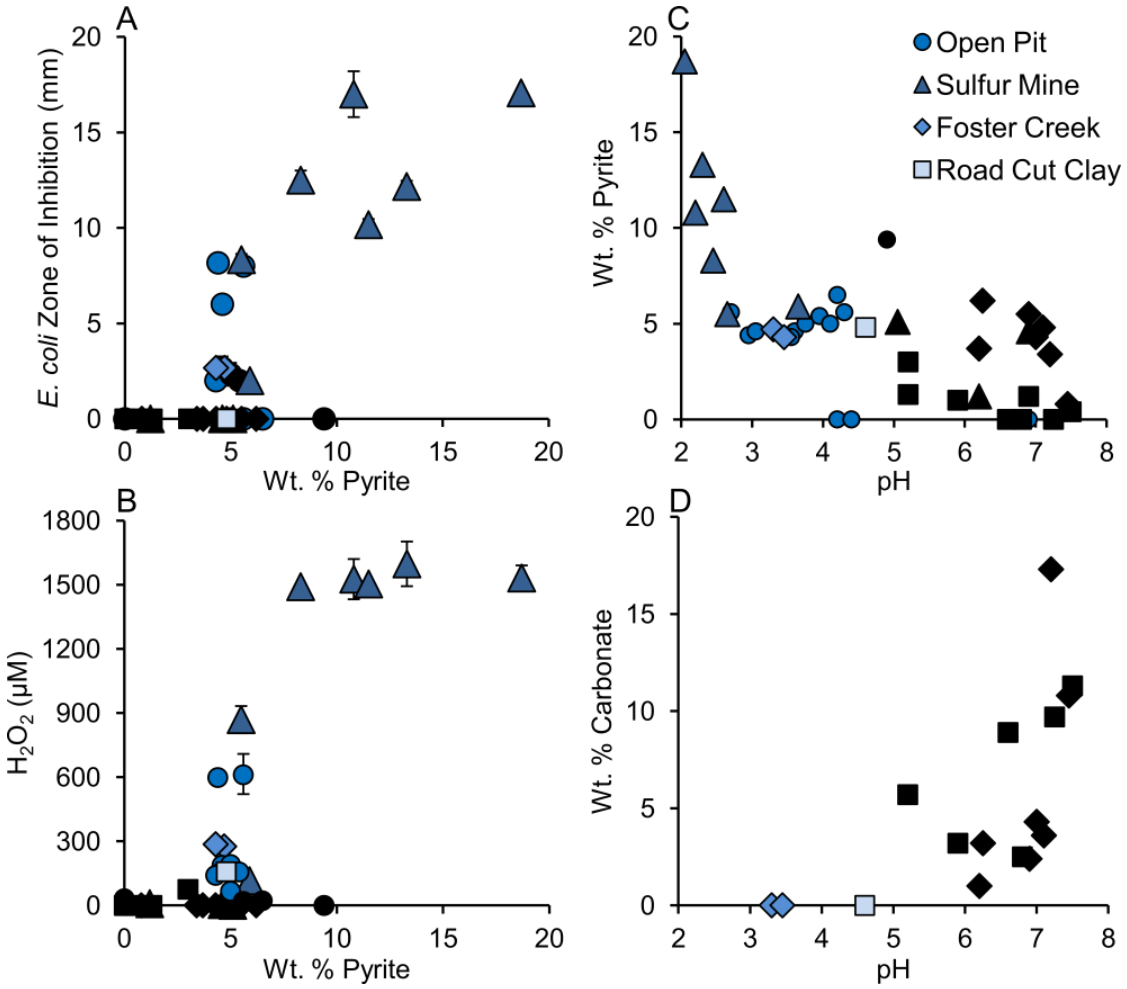

Figure 4.2. Effect of pyrite and carbonate. (A) Zones of *E. coli* growth inhibition and (B) hydrogen peroxide concentration (µM) plotted against weight % pyrite. (C) Weight percentages of pyrite and (D) carbonate plotted against pH of mineral suspensions. Samples in blue are antibacterial while black samples showed no antibacterial effect.

4.2.2 Metal Solubility and Speciation

Modeling changes in metal speciation at varying pH and Eh can shed light on the aqueous geochemistry of antibacterial clays. Measured pH and Eh values of mineral suspensions (100 mg/ml in 10 g/l LB broth) were are plotted against calculated Pourbaix (pH-Eh) diagrams for Fe, Al and S (Fig. 4.3). The logK values and reactions used in the

calculations are listed in Appendix F. When samples are mixed with bacteria in growth media (10 g/l LB) the pH and Eh of the system shifts towards a more oxidized equilibrium, eventually forming goethite. Bactericidal samples have pH values < 4.2 and Eh > 0.5 V. Samples with high Eh (> 0.5V) and low pH (< 4.2) released mM amounts of Fe^{2+}, Fe^{3+} and Al^{3+} as pyrite oxidation and mineral dissolution occurred (Fig. 4.1). Below pH 3.8 Al is soluble either as Al^{3+} or $AlSO_4^+$ cations, as shown in the pH-Eh diagram (Fig. 4.3 B). This transition to more soluble Al species is observed in the mineral leachates, where Al concentrations increase below pH 4 (Fig. 4.1 C).

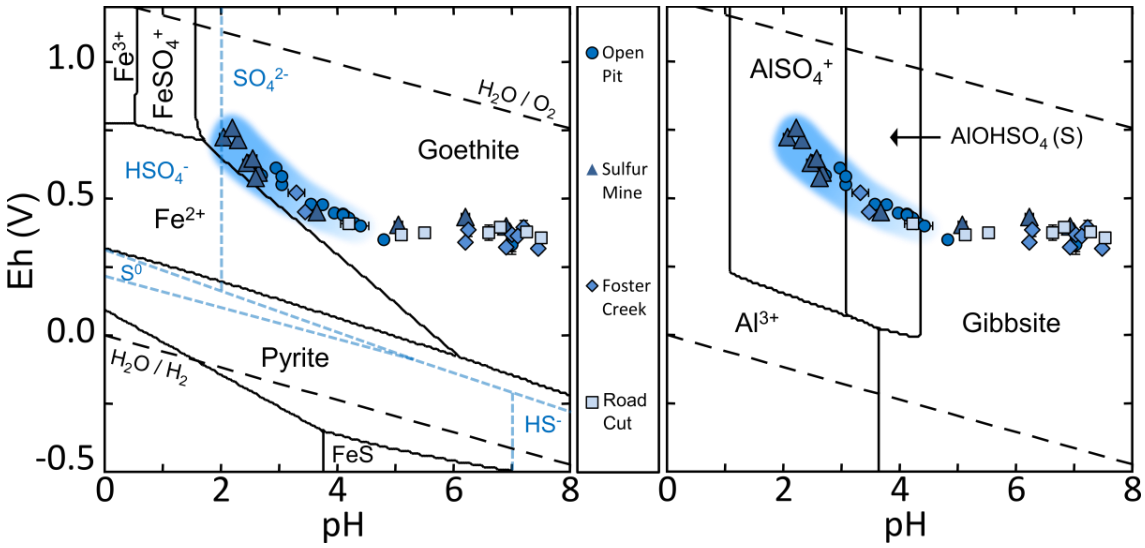

Figure 4.3. pH-Eh speciation diagrams. Speciation diagrams of the (A) Fe-S-O-H (black lines) and S-O-H system (blue lines) and (B) Al-S-O-H system at 25°C. Concentrations of Fe and Al were set at 2 mM and S at 4 mM to mimic bactericidal leachates. Data points are from pH and Eh measurements of mineral suspensions (100mg/ml) containing 10 g/l LB. The bactericidal samples (highlighted in blue) occurred at pH < 4.2 and Eh > 0.45 V.

4.2.3 Antibacterial Activity in the Open Pit Mine

Samples of blue clay taken at the interface of the overlying oxidized zones showed greater antibacterial activity than samples taken at depth (1.5 m) (Table 3.3). A closer examination of the depth series shows that the pH and redox state of the rehydrated samples play an important role in the antibacterial process (Fig. 4.4). The pH values decrease as samples approach surface in the blue zone, as a result of increased metal solubility and hydrolysis. This corresponds with increased pyrite oxidation and H_2O_2 production (Fig. 4.4 A-C). The antibacterial activity of the blue clays declines with depth due to elevated pH (> 4), which lowers Fe^{3+} solubility and pyrite oxidation rates in the prepared mineral suspensions (Fig. 4.4 D).

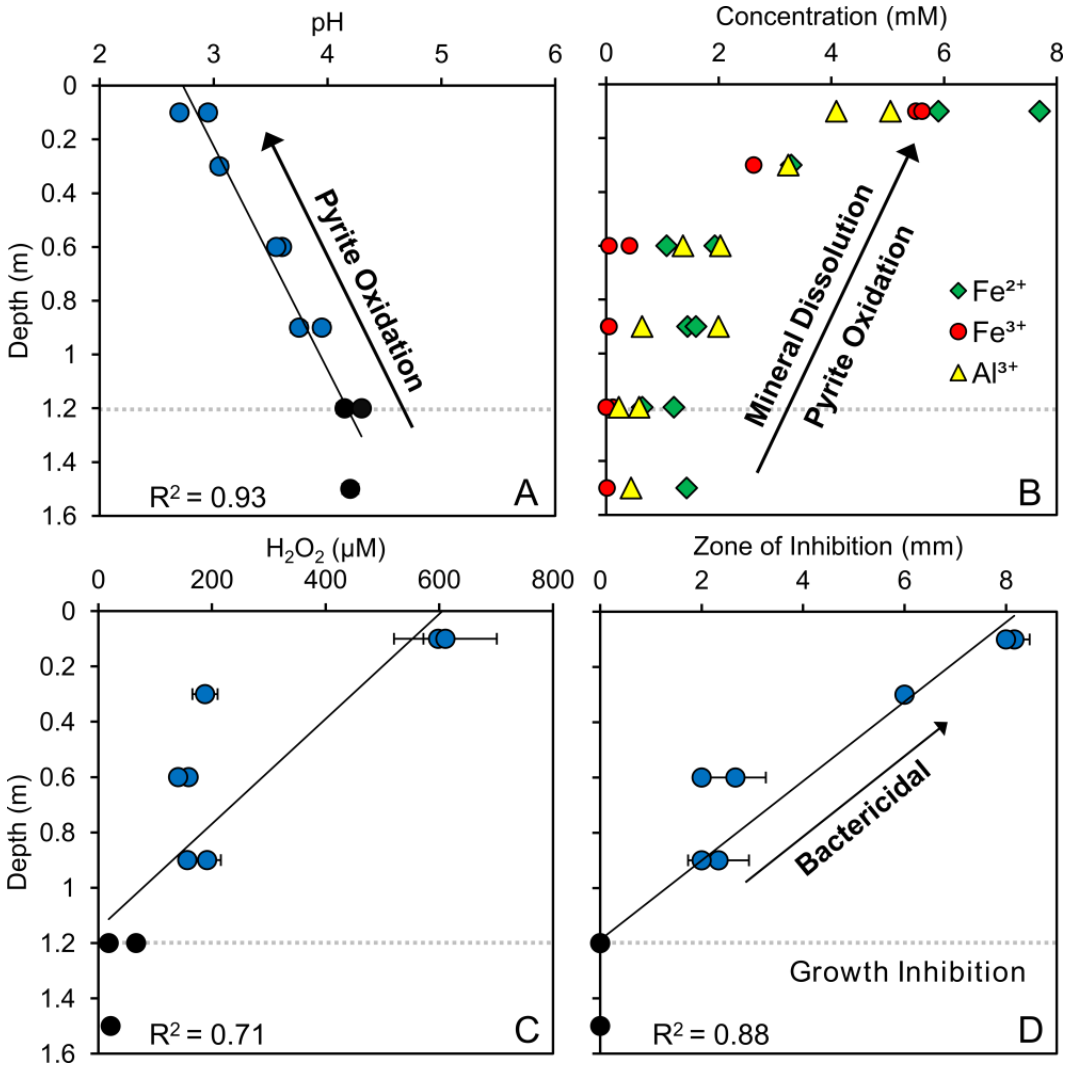

Figure 4.4. Open Pit oxidation trends. Samples from the Open Pit blue zone taken from 0.1 to 1.6 m depth plotted against (A) pH, (B) metal concentration, (C) hydrogen peroxide concentration and (D) *E. coli* ATCC 25922 zones of growth inhibition. Data points for bactericidal samples are shown in blue and samples that inhibited bacterial growth are shown in black.

4.2.4 Pyrite Size and Redox

The crystal size of pyrite can affect oxidation and dissolution, with greater reaction rates in smaller size fractions (Schoonen et al., 2010). The black clay zones in the Sulfur Mine contained fine disseminated pyrite, while the Open Pit blue clays had

larger pyrite crystals that are visible with the naked eye (50-100µm) in addition to finer Fe-S precipitates. Less than 20µm size fractions of samples from the Sulfur Mine and Open Pit were separated and measured with XRD to qualitatively compare pyrite content. The black clay zones in the Sulfur Mine are richer in < 20µm pyrite that rapidly oxidizes (Fig. 4.5 C). Increasing soluble Fe^{2+} concentrations and high Eh values correlate with increasing pyrite concentrations in the Sulfur Mine (Fig. 4.5 A and B). Blue clays from the Open Pit only show increased Fe^{2+} and Eh values in the more oxidized samples towards the surface (Fig 4.5 A and B). Increased antibacterial activity in the Sulfur Mine occurs due to the high concentrations of < 20 µm pyrite. The small crystal size provides greater surface area for pyrite oxidation, increasing Fe solubility and H_2O_2 generation (Figs. 4.2 and 4.5).

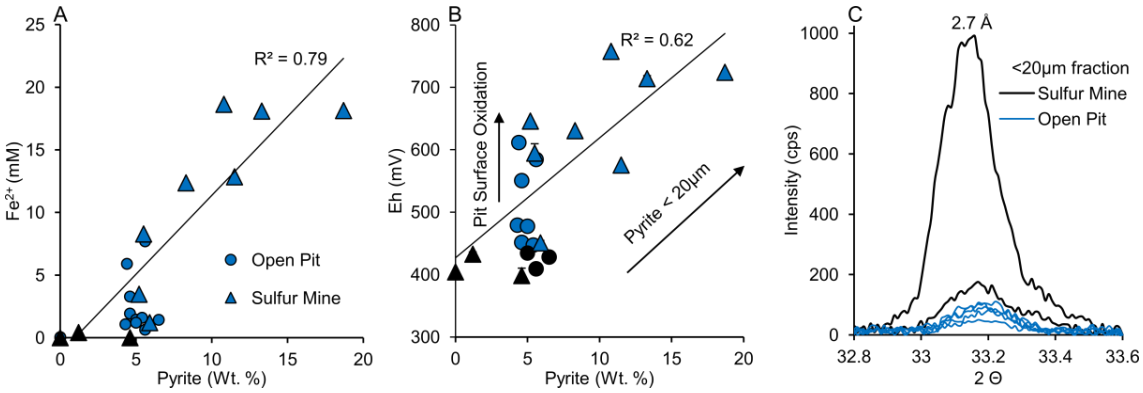

Figure 4.5. Pyrite redox and size. (A) Leachate Fe^{2+} concentrations (mM) and (B) Eh values (mV) plotted against pyrite wt. %. (C) XRD pattern of pyrite intensity in < 20µm size fractions separated from samples in the Sulfur Mine and the Open Pit. Samples marked in black showed no antibacterial activity.

4.2.5 Cation Exchange Capacity

The Open Pit white oxidized zones, with no measureable pyrite, inhibited bacterial growth releasing lower, but significant amounts of Fe^{2+}, Fe^{3+} and Al^{3+} (Table 4.1). The source of Fe and Al may be from clay mineral dissolution and possibly clay mineral cation exchange. Average cation exchange capacity (CEC, milliequivalent/100g) values for the different alteration zones are shown in Figure 4.6. The CEC values range from 12-23 meq/100g with the highest values measured in the Open Pit white clay where smectite is present. From the CEC in the white clays it is calculated that up to 11.5 mM of divalent cations can be stored in the interlayer spaces of the expandable clay, providing an abundant reservoir for Fe^{2+} released from pyrite. Smectite interlayer exchange sites prefer Ca^{2+} (Moore and Reynolds, 1997), which might displace Fe^{2+} as Ca^{2+} increases in solution.

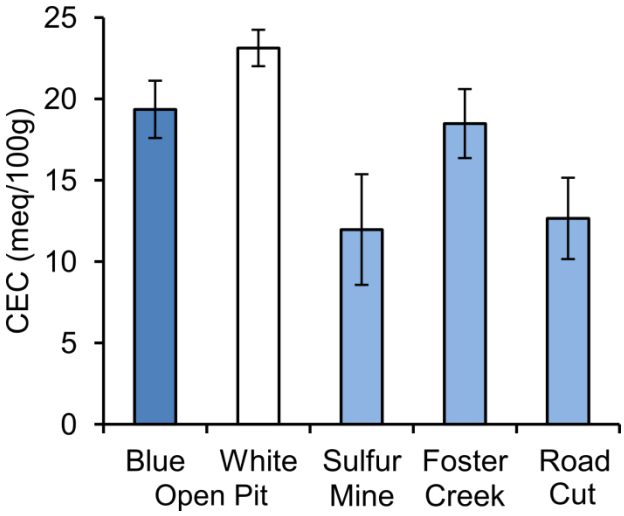

Figure 4.6. Cation exchange capacity. Average CEC values from the 4 clay zones sampled in the OMT deposit. CEC values are reported as milliequivalent charge per 100g sample (meq/100g).

4.2.6 Transmission Electron Microscopy

TEM imaging of *E. coli* and *S. epidermidis* cells reacted with a bactericidal blue sample from the Open Pit (sample P4) were measured to determine if minerals resulted in major cell lysis. This sample was chosen because of its bactericidal activity and more moderate pH (~3) compared to the acidic (pH 2.1) black clays from the sulfur mine. Figure 4.7 compiles the TEM images of *E. coli* and *S. epidermidis* cells in their initial healthy condition, and in time series (2, 8 and 24hrs) after incubation with a mineral suspension (100 mg/ml).

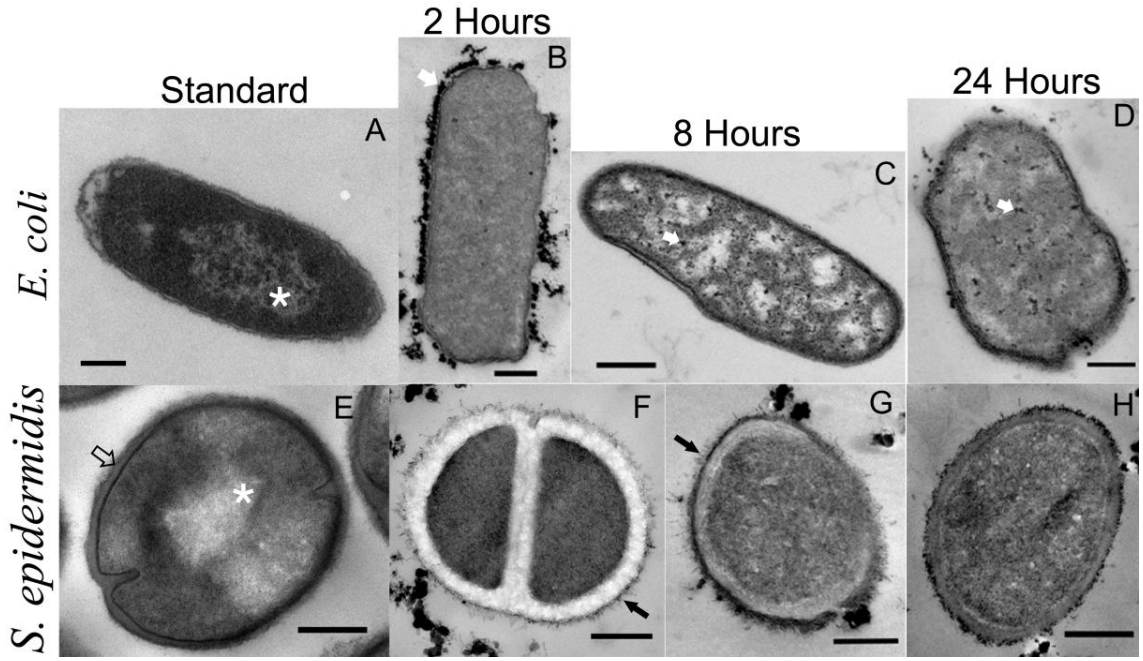

Figure 4.7. TEM imaging. Time series TEM images of (A-D) Gram negative *E. coli* ATCC 25922 and (E-H) Gram positive *S. epidermidis* ATCC 14990 reacted with a 100mg/ml mineral suspension from the Open Pit mine (sample P4) (scale bars = 250 nm). (A and E) White stars indicate bacterial nucleoids. Solid white arrows (B, C, D) point to mineral particles and electron dense particles within the cytoplasm. (E) Hollow black arrow shows peptidoglycan layer. (F, G) Solid black arrows point to thread like appendages coated with electron dense particles.

The presence of intact bacterial cell membranes indicates that cell lysis is not the primary antibacterial mechanism; however membrane permeability may still be compromised (Fig. 4.7). Both bacterial species accumulated extracellular mineral particles (20-100 nm diameter), which did not appear to disrupt the cell walls (Fig. 4.7). The Gram negative *E. coli* cells exhibited greater changes in their cell morphology than Gram positive *S. epidermidis*. Cytoplasmic condensation occurred in *E. coli* after 8 and 24 hrs (Fig 4.7 C and D) resulting in electron transparent voids and small (5-10 nm) particles throughout the cytoplasm. The *S. epidermidis* cells develop a less electron dense region surrounding the cell envelope after 2 hrs of reaction (Fig. 4.7 F). After 8 and 24 hrs the *S. epidermidis* cells regain contrast in their cell walls and display adhesion of (< 5nm) mineral particles (Fig. 4.7 G and H). After 8 and 24 hours both species show an electron dense zone surrounding their cell walls. The *S. epidermidis* cells also show hair like wisps on the exterior cell walls (Fig. 4.7 F, G and H), likely in response to acidic conditions (Beveridge and Koval, 1981).

4.3 Discussion

4.3.1 Antibacterial Mineral Zones

In this study, mineralogy, solution chemistry and antibacterial activities were compared among samples representing different mineral alteration zones within the OMT clay deposit. We hypothesize that antibacterial activities relate to the mineralogy, fluid pH and redox state of the hydrated clays when applied to pathogenic bacteria. To test this, we measured the antibacterial effectiveness as a function of mineralogical and chemical variables across the deposit. The degree of antibacterial activity correlates with

mineralogical variables controlling pH and redox conditions, which in turn influences element solubility and exchange between minerals and bacteria.

When antibacterial clays are hydrated with DDI water, a series of spontaneous reactions occur as a new chemical equilibrium is approached (Williams et al., 2008; 2011; Morrison et al., 2014). These conditions are different from those established within the natural geologic setting. Quantitative mineralogy and antibacterial susceptibility testing results indicate that not all samples containing pyrite are antibacterial (Tables 3.3-3.6). The white oxidized zones in the Open Pit, which do not contain pyrite or any other detectable sulfides, still prevented bacterial growth (Table 3.3). The Open Pit red oxidized zones were not antibacterial and contained no measurable pyrite, however the Fe-oxide goethite (3.4 %) was present in these samples, which is a common pyrite oxidation product (Hutchinson and Ellison, 1992).

The consistently high abundance of Fe associated with the most antibacterial OMT samples points to its involvement in the bactericidal process. The most potent antibacterial samples are found in the Sulfur Mine, which contain high concentrations of < 20μm pyrite that rapidly oxidize, lowering pH and promoting mineral dissolution (Fig. 4.5). Antibacterial activity and pyrite concentration (< 20 μm) were directly related in samples from the Sulfur Mine, indicating pyrite size and surface area govern the reactivity of sulfides in the bactericide.

Bactericidal samples from the Open Pit exist where pH and Eh conditions promote pyrite oxidation and silicate mineral dissolution. The precipitation of secondary minerals such as jarosite occurs at low pH (< 3) during pyrite oxidation (Hutchinson and Ellison, 1992; Murad and Rojik, 2005). Jarosite is not present in the less antibacterial

(inhibitory) samples at greater depths in the blue zone, which have higher pH (> 3) and release a lower amount of metals (Fig. 4.4). Hydrogen peroxide production in aqueous solution was also associated with increased metal release and pyrite oxidation in the bactericidal samples from the Open Pit (Fig. 4.4). Elevated pH (5-7) due to the presence of carbonate in all of the identified zones eliminated the antibacterial effect by lowering metal solubility and pyrite oxidation. The oxidation of pyrite results in a cascade of redox reactions (discussed below) that lower pH and release both ferrous and ferric iron into solution. Environmental microbes have evolved to handle this low pH metal rich environment, whereas human pathogens have not (Garrels and Thompson, 1960; Nies, 2003).

4.3.2 Environmental Microbes

It is important to note that, while the OMT Blue clays are antibacterial against a broad spectrum of human pathogens, (Cunningham et al., 2010, Morrison et al., 2014; see Methods Chapter 7) there are environmental microbes that have evolved to survive in the natural environment and are metabolically active in the clay. Isolation of environmental microbes from an OMT Blue sample showed that the genus *Burkholderia* comprises the majority of bacteria living in the low pH, metal-rich conditions (pers. comm. Weimin Gao, ASU Biodesign Institute). The genus *Burkholderia* is metabolically diverse and contains 58 species (Bhowal and Chakraborty, 2011). Isolates of *Burkholderia* have been found in acidic soils (pH 2.9), iron ores, and acid mine drainage (pH 1.5-3) (Valverde et al., 2006; Church et al., 2007; Bhowal and Chakraborty, 2011). *Burkholderia* growing in acid mine drainage settings are chemolithoautotrophic and oxidize thiosulfate to sulfate

(Bhowal and Chakraborty, 2011). Acidophilic bacteria exhibit more robust metal efflux systems and different membrane lipid compositions compared to human pathogenic bacteria, which evolved to survive in iron-limited host environments (Ratledge and Dover, 2000; Nies, 2003).

4.3.3 Iron Sulfides and Reactive Oxygen Species

The dissolution of pyrite, under circum-neutral to alkaline pH conditions, is a function of the dissolved molecular O_2 content according to Reaction 1 (below). However, Fe^{3+} is the major oxidant in acidic (pH < 4) conditions (Reaction 2) (Moses and Herman, 1991; Evangelou, 1995). Pyrite oxidation rates by Fe^{3+} are therefore limited by oxidation rates of ferrous iron (Fe^{2+}) in solution by dissolved O_2, (Garrels and Thompson, 1960; Singer and Stumm, 1970), with a rate constant of approximately 10^{-3} M/min (Reaction 3) (Stumm and Morgan, 1996; Morgan and Lahav, 2007). Cohn et al., (2006) showed that pyrite spontaneously generates ROS through a series of intermediate reactions (Reactions 4-6). Superoxide anions ($\bullet O_2^-$) and hydrogen peroxide (H_2O_2) are respectively produced via the Haber-Weiss reactions (Reactions 4 & 5), and ultimately form hydroxyl radicals (•OH) via the Fenton reaction (Reaction 6) (Rimstidt and Vaughan, 2003; Cohn et al., 2006; Schoonen et al., 2010). Pyrite, as a semi-conductor, has the ability to exchange 2 electrons at a time, making the direct formation of hydrogen peroxide possible (Schoonen et al., 2010). Pyrite oxidation, known to cause nucleic acid degradation by •OH radicals, rapidly reacts with biomolecules and impedes certain cellular functions (Cadet et al., 1999: Cohn et al., 2006). The oxidation of pyrite

involving ROS helps to explain the observed bactericidal activity caused by OMT Blue samples.

Stable Reactions:

$$2\ FeS_2 + 7\ O_2 + 2\ H_2O \rightarrow 2\ Fe^{2+} + SO_4^{2-} + 4\ H^+ \quad (1)$$

$$FeS_2 + 14\ Fe^{3+} + 8\ H_2O \rightarrow 15\ Fe^{2+} + 2\ SO_4^{2-} + 16\ H^+ \quad (2)$$

$$Fe^{2+} + O_2 + 2H^+ \rightarrow Fe^{3+} + 2\ H_2O \quad (3)$$

Intermediate Reactions:

$$Fe^{2+} + O_2 \rightarrow Fe^{3+} + \mathbf{\bullet O_2^-} \quad (4)$$

$$Fe^{2+} + \bullet O_2^- + 2\ H^+ \rightarrow Fe^{3+} + \mathbf{H_2O_2} \quad (5)$$

$$Fe^{2+} + H_2O_2 \rightarrow \mathbf{\bullet OH} + OH^- + Fe^{3+} \quad (6)$$

4.3.4 Cation Exchange

In low pH (< 4) acid mine waters smectite has been shown to fully dissolve (Galan et al., 1999). However, kaolinite and illite show little change in their crystal chemistry when exposed to these acid conditions (Galan et al., 1999; Shaw and Hendry, 2009). The mixed-layered illite-smectite found in the OMT deposit may be more resistant to acid dissolution because of its high illite content, allowing the expandable interlayer of smectite in the mixed-layered clay to act as a reservoir for exchangeable cations. Therefore, if dissolution of pyrite supplies abundant Fe^{2+}, it may be adsorbed in the expandable smectite interlayers. The pH in the interlayer of expandable clay minerals can be several log units lower than that of the bulk (external) solution (Yariv, 1992; Yariv and Cross, 2002). The lower acidity of the interlayer may slow the oxidation rate of

reduced iron (Singer and Stumm, 1970), thus preserving it for extended 'time-release' from the clay.

Exchangeable Fe^{2+} in illite-smectite would be released from the smectite when DDI water is added to make a clay poultice, potentially by Ca^{2+} exchange, since Ca is abundant due to feldspar dissolution in the deposit. Therefore, the I-S in the antibacterial clay may both buffer the fluid to stabilize Fe^{2+} and act as a potential reservoir. The cation exchange capacity of the clay minerals coupled with pyrite oxidation and feldspar dissolution explains the elevated cation levels measured in the leachates of the blue clay samples. The average CEC measurements of the bulk minerals (Fig. 4.6) indicate that mM levels of cations can be exchanged by the clay mineral interlayer spaces. Considering the composition of the mineral leachates, Ca^{2+} and Fe^{2+} are more likely to participate in the exchange process over trivalent cations (Fe^{3+} and Al^{3+}). Since Ca^{2+} is a preferred cation in the smectite interlayer (Moore and Reynolds, 1997), it would outcompete Fe^{2+} for exchange sites.

As an example, consider the water chemistry associated with the white clay zone from open pit mine. This clay, in suspension, has some antibacterial effect (Tables 3.3 and 4.1), but the aqueous leachate is only bactericidal at high mineral loading (500 mg/ml; data not shown). Given the CEC of this clay (Fig. 4.6), and the measured cation content of its aqueous leachate, we calculate that the smectite interlayer 'reservoir' could hold up to 11.5 mM Fe^{2+} at a 100mg/ml mineral:water ratio. We tested the ability of smectite to serve as a reservoir for Fe^{2+} by saturating a standard smectite (SWy-1; Wyoming bentonite from the Clay Minerals Repository, Purdue Univ.) with Fe^{2+} using a 1M $FeCl_2$ solution. Antibacterial susceptibility testing with the Fe^{2+}-saturated smectite

also showed no surviving bacterial colonies. This test confirms that smectite can be a reservoir of Fe^{2+} that is antibacterial when released by cation exchange.

4.3.5 Mineral and Metal Toxicity

Minimum inhibitory and bactericidal concentrations (MIC) and (MBC) are used to measure the antibacterial potency of a compound. The MIC is defined as the lowest concentration of an antibacterial compound that prevents visible bacterial growth (optical density at 600 nm) in nutrient broth. The MBC is defined as the minimum amount of an antibacterial compound that causes a 100% reduction in bacterial growth measured by plating and CFU counting (Wilson et al., 1990; Harrison et al., 2005). All metal concentrations in mineral leachates when reacted with bacteria are below published MBCs for *E. coli* (Table 4.3), which were measured at circumneutral pH (Nies, 1999; Harrison, 2005). However not only the metal concentration, but its speciation, which is a function of pH and Eh, is important to consider as this determines the chemical reactions that may affect bacterial cell viability (Fig. 4.3). Calcium is very high in the OMT mineral leachates due to the dissolution of the high Ca primary feldspars and their alteration products, however it is not considered a toxic element (Borrok et al., 2004).

Notably, the aqueous leachates of the blue clays contain complex cation mixtures (Tables 4.1 and 4.2) and combinations of elements might work synergistically to produce the observed bactericidal activity at lower MIC and MBC concentrations than reported for individual metals (Nies, 1999; Harrison et al., 2005). The majority of studies on bacterial metal toxicity utilize buffered nutrient broth near circumneutral pH, which likely alters the redox state and causes pH-sensitive metals to precipitate (Nies, 1999;

Harrison et al., 2005). In studies of human pathogens, the toxicity of iron is traditionally not considered due to its low solubility (10^{-18} M) at circumneutral pH (Table 4.3). However, the natural mineral-water suspensions studied here have distinctly different solution pH and Eh, which influence the solubility of metals. Clearly, exposure of bacterial cells to metal concentrations exceeding microbial demand requires rapid homeostatic responses to prevent cell death.

Table 4.3. Published MIC and MBC concentrations of elements for *E. coli*.

Element	Ion Species	*E. coli* [a]MIC	*E. coli* [b]MBC
Al	(Al^{3+})	2000	19000
V	(V^{3+})	5000	
Cr	(Cr^{3+})	5000	
Mn	(Mn^{2+})	20000	198000
Co	(Co^{2+})	1000	
Ni	(Ni^{2+})	1000	17000
Cu	(Cu^{2+})	1000	16000
Zn	(Zn^{2+})	1000	31000
As	(AsO_2^-)		75000
Se	(SeO_3^{2-})		13000
Ag	(Ag^+)	20	60
Cd	(Cd^{2+})	500	2300
Au	(Au^{3+})	20	
Hg	(Hg^{2+})	10	40
Pb	(Pb^{2+})	5000	

[a]Minimum inhibitory concentration (MIC) of metals (24 hrs) for *E. coli* determined using Tris-buffered mineral salts medium (pH 7), with 2 g/L Na-gluconate and 1g/L yeast extract (Nies, 1999).
[b]Minimum bactericidal concentration (MBC) of metals (24 hrs) for *E. coli* determined using Luria-Bertani medium enriched in vitamin B1 (Harrison et al., 2005)

4.3.6 TEM

Given that human pathogens evolved to thrive under circumneutral pH conditions with limited Fe availability, one might suspect that acidic, metal-rich conditions imposed by topical application of OMT Blue clays would compromise cell integrity. However, TEM images (Fig. 4.7) do not support cell lysis as a dominant antibacterial mechanism

for the OMT clays. While many antibacterial agents damage peptidoglycan peptide linkages and induce lysis (Silhavy, 2010), the bacterial cells treated with OMT Blue clays maintain their rigidity and structure. Accumulation of mineral particles around bacterial cells did not appear to penetrate cell walls or disrupt the peptidoglycan layers (Fig. 4.7), but both *E. coli* and *S. epidermidis* cells showed cytoplasmic condensation, and intracellular accumulation of <10 nm electron dense particles. The *S. epidermidis* appeared more resistant to cytoplasmic condensation and had fewer cytoplasmic particles. An electron transparent region surrounding the *S. epidermidis* cells appeared after 2 hours of reaction with the blue clay (Fig. 4.7 F), which could result from secretion of a protective layer of polysaccharides (N-acetyl-glucosamine) that allows *S. epidermidis* cells to adhere to surfaces and resist environmental stress (Götz, 2002). These polysaccharides appear transparent because none of the chemical stains used in TEM preparation (osmium tetroxide, lead citrate and uranyl acetate) bind to these exo-polysaccharides to provide contrast. This layer is not observed at longer incubation times; suggesting that the defense mechanism failed and infiltration of metals began.

4.4 Conclusions

Antibacterial susceptibility testing indicates that clays formed in high-sulfidation environments (Sulfur Mine) are the most antibacterial. The high pyrite content (~ 18%) and small crystal size (< 20μm) in these zones promotes oxidation and mineral dissolution, releasing Fe^{2+}, Fe^{3+} and Al^{3+} (> 10 mM) while generating H_2O_2. Samples from the Open Pit contained lower pyrite levels (4-6 %) that were bactericidal when pH and Eh conditions promoted pyrite oxidation, mineral dissolution and H_2O_2 generation.

The Open Pit white oxidized zones contained no iron sulfides and still prevented bacterial growth through the release of Fe^{2+} and Al^{3+} at low pH (< 4.7). The clays in the white zone likely release Fe^{2+} through cation exchange, indicating that the I-S interlayer spaces provide an important reservoir for cations. Bioimaging of bacteria reacted with mineral suspensions suggest that cell lysis is not the primary mechanism causing cell death. The soluble metals leached from the clays accumulate on the exterior of the bacteria, as intracellular metals accumulate and precipitate nano-particles.

The results from this chapter clarify many of the variations in antibacterial activity found in the OMT deposit and provide simple mineralogical and geochemical parameters (pH and Eh) that can be used to identify antibacterial clay zones in hydrothermal deposits. The physiological and genetic stress responses of *E. coli* will be investigated in the next chapter. By characterizing the synergistic toxicity of metal mixtures in relation to pH, metal solubility and reactive oxygen species we provide mechanistic insight into a natural geochemical process capable of killing pathogenic bacteria.

Chapter 5

THE ANTIBACTERIAL MECHANISM

5.1 Introduction

The previous chapter compared the geochemical properties of different hydrothermal alteration zones in the OMT deposit to find similarities among the different mineral assemblages. Only a few clays have been identified that kill a broad spectrum of human pathogens (Williams et al., 2008; Morrison et al., 2014). Critically important is the buffering capacity of the mineral assemblage, maintaining pH environments (< 4) where Fe and Al are soluble and may be stored in exchange sites of clay interlayers for extended release (Morrison et al., 2014). A bactericidal sample from the Open Pit mine (P4) was chosen for this study. While the most antibacterial samples are found in the sulfur mine, this sample was chosen because it is bactericidal at higher pH (~3) compared to the sulfur mine samples (pH 2) and releases mM concentrations (~10 mM) of Fe and Al in 100mg/ml mineral suspensions.

The emergence of antibiotic resistant human pathogens has accelerated inquiries into alternative antibacterial compounds (Walsh, 2000; Lemire et al., 2013). Bacteria rapidly establish resistance against traditional antibiotics that target specific cellular mechanisms (DNA replication, protein and cell wall synthesis (Walsh, 2000). As a result, alternative therapies against bacterial infections have gained attention. The aim of this chapter is to determine how pathogenic bacteria are killed by a geochemical process, where minerals are transitioning to a new more oxidized equilibrium.

Pathogenic bacteria have made their living in the host environment, where soluble metals and pH are tightly regulated. Pathogenic bacteria exposed to elevated metal

concentrations rapidly express various efflux systems that attempt to moderate toxic metal entry into the cytoplasm (Mullen et al., 1989; Nies, 1999). More energetically demanding methods of metal resistance include complexation onto thiol-containing molecules and alteration of redox to allow toxin efflux (Nies, 1999; Lemire et al., 2013). Bacterial exposed to Fe^{2+}, Fe^{3+} and Al^{3+} in the presence of ROS may be subject to lipid peroxidation and oxidation of membrane proteins (Hailwell and Chirico, 1993; Gutteridge, 1995; Tang et al., 2000; Cabiscol et al., 2000). Lipid peroxidation rates by Fe^{2+} has also been shown to increase in the presence of other divalent and trivalent cations (Al^{3+}, Fe^{3+}, Pb^{2+}) by potentially altering lipid membrane structure to promote peroxidation (Gutteridge et al., 1995; Aruoma et al., 1985). Therefore the mixture of metals in the OMT clays may be working synergistically to damage bacterial cells unlike single metal systems.

The metals released by the OMT clays likely overwhelm bacterial efflux mechanisms by providing a continuous source of soluble Fe^{2+}, Fe^{3+} and Al^{3+}, typically not encountered in the host environment. In nature microbes have evolved in contact with minerals, many times in low pH (< 3) metal rich environments where microbes deriving energy through the oxidation of metals or the minerals themselves (Kostka et al., 2002: Valverde et al., 2006; Church et al., 2007; Bhowal and Chakraborty, 2011). However, when antibacterial clays are hydrated for medicinal application their natural equilibrium shifts, altering pH and redox conditions and releasing metals that stress pathogenic bacteria (Williams et al., 2011; Morrison et al., 2014). The effect of Fe and Al solubility on bacterial toxicity will be investigated since these are the primary elements producing toxicity in the OMT clays (Williams et al., 2011; Morrison et al., 2014).

Fe and Al have contrasting roles in biological systems. Fe is essential to nearly all organisms, performing vital cellular functions (e.g., respiration, gene regulation, DNA biosynthesis) as protein cofactors (Andrews et al., 2003). Oxidized Fe^{3+} is a limiting nutrient for bacterial growth due to its exceedingly low solubility (10^{-18}M) at physiological pH, requiring siderophore-mediated uptake (Andrews et al., 2003). On the other hand, Fe^{2+} is soluble but excess amounts can be toxic to bacteria by increases oxidative stress in the cell (Imlay et al., 2008). In contrast, Al has no known biological function but is thought to exhibit toxicity through membrane damage (Williams, 1999). The toxicity of metals is primarily related to their binding affinities and production of reactive oxygen species (ROS) (Lemire et al., 2013).

Toxicity from metals, ROS and pH trigger genetic responses in *E. coli* that can be used to gain insight to the mechanism of metal toxicity created by the OMT clays. In this chapter we will investigate the physical and genetic stress responses of *E. coli* to membrane damage (σ^E-stress response) and DNA damage (SOS response). LacZ gene fusions were used to measure gene expression, linking a gene of interest to the *lac* operon, which expresses the enzyme β-galactosidase (Huisman et al., 1984). The concurrent expression of β-galactosidase and the gene of interest occur and gene expression can be quantified by measuring β-galactosidase activity (Huisman et al., 1984; Vidal-Aroca et al., 2006). Two LacZ fusions were chosen for this study, *rpoHP3*::*lacZ* (σ^E-response) and *sulA*::*lacZ* (SOS-response), which are part of many genetic response mechanisms used by the cell to combat stress (Huisman et al., 1984; Alba and Gross, 2004; Raivio, 2005).

The σ^E-stress response (*rpoH3* sigma factor) is controlled by the RseA repressor that keeps σ^E bound until a stress event triggers its release (Alba and Gross, 2004). Outer membrane stress from heat (> 40°C), ethanol and ROS can cause misfolding of outer membrane proteins (OMPs), rendering them useless to the cell (Alba and Gross, 2004). These misfolded proteins must be removed from the outer membrane for proper cell function to resume. Under normal growth conditions σ^E is repressed by RseA but when misfolded proteins accumulate the σ^E-stress response is activated through a series of proteolytic events triggered by the binding of misfolded c-terminus protein moieties (exposed carboxyl group) to DegS in the periplasm. This activates the DegS protease, leading to a series of proteolytic events that release σ^E from the repressor (Ades, 2004). Once σ^E is free from the repressor it binds RNA polymerase and transcribes a series of genes that degrade the misfolded proteins and regulate the synthesis and folding of OMPs in the outer membrane (Alba and Gross, 2004).

The SOS-stress response in *E. coli* is regulated by the LexA repressor, which remains bound to DNA until its release is triggered by DNA stress (Huisman et al., 1984). Oxidative stress inside the call can cause single strand breaks in DNA that must be repaired before cell division resumes (Huisman et al., 1984). The RecA protein in *E. coli* binds to these DNA strand breaks, allowing the activated RecA* to cleave the LexA repressor (Huisman et al., 1984). Once cleaved, LexA binds RNA polymerase and expresses over 30 genes involved in DNA repair. The *sulA* gene (used in the LacZ fusion) is part of these downstream genes and halts cell division by binding FtsZ and preventing it from assembling the septum filaments that separate dividing cells (Huisman et al., 1984).

This chapter documents the antibacterial mechanism of the OMT clays. Using metal toxicity, oxidation and genetic assays, along with advanced bioimaging techniques, we gained mechanistic insights to the key elements of this natural antibacterial process. Our findings have implications for the discovery and synthesis of novel mineral based antibacterial agents.

5.2 Results and Discussion

5.2.1 Metal Solubility and Reactive Oxygen Species

The Oregon blue clay completely kills a broad range of human pathogens, including antibiotic resistant strains (see Methods). To understand the antibacterial mechanism exhibited by the blue clays we first measured metal solubility and its effect on toxicity and ROS production. The blue clay (sample P4) releases metals (Fe^{2+}, Fe^{3+}, Al^{3+} and Ca^{2+}) through pyrite oxidation, cation exchange and dissolution of clay minerals and plagioclase feldspar (Morrison et al., 2014), reaching mM concentrations (Fig. 5.1A). Other metal species (e.g., As, Ag, Hg, Pb, Cu, Zn, Ni) are present in nM to µM concentrations, below levels that inhibit growth (Nies, 1999; Harrison et al., 2005) (Appendix D, Table 5.1). Clay suspensions in deionized water, and their aqueous leachates (equilibrated 24h, the time it takes to kill 100%) were prepared for antibacterial susceptibly testing. Minimum inhibitory and minimum bactericidal concentrations (MIC, MBC) of clay suspensions, and leachates were compared in minimal salts and amino acids (MSA) media and Luria broth (LB) (Fig. 5.1, Appendix F, Table 5.2).

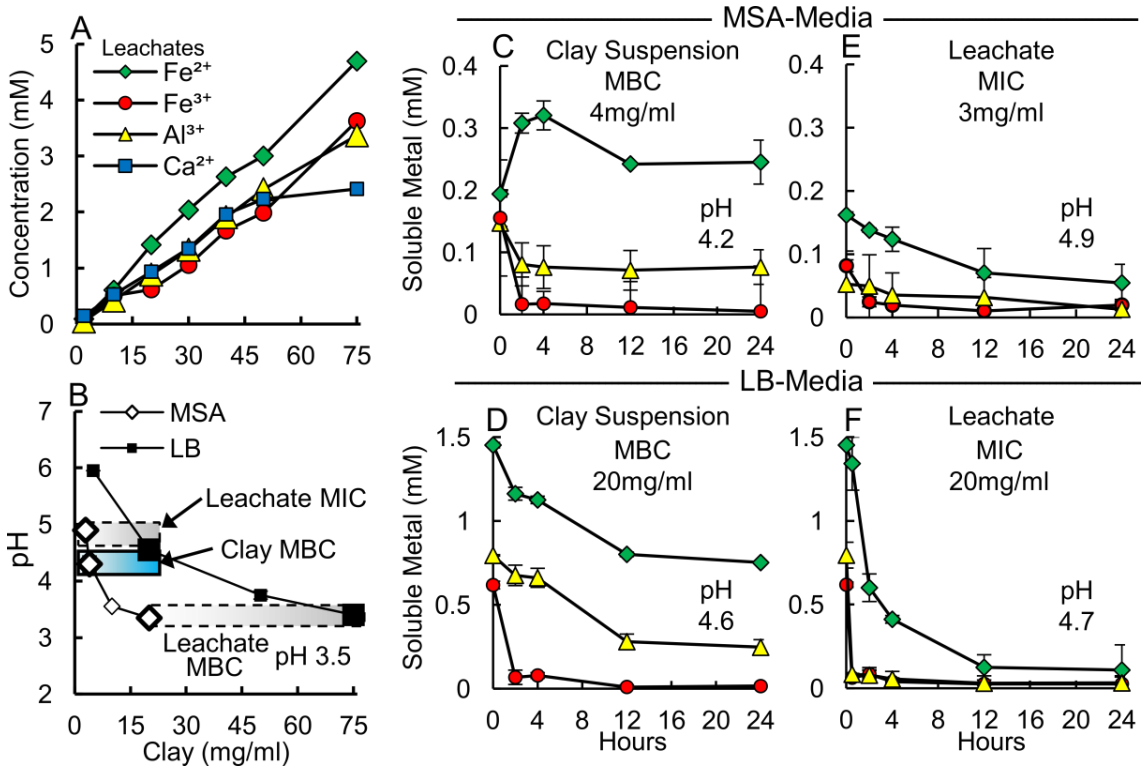

Figure 5.1. Extended metal release. Clay suspensions provide extended metal release whereas aqueous leachates alone precipitate metals. (A) Major element concentrations leached from the blue clays. (B) pH, MIC and MBC for leachates (gray bars) and MBC for clay suspensions (blue bar) measured in MSA and LB media. The leachate pH is low (pH 3.4-3.5) at MBC in both media, while clay suspensions kill bacteria at higher pH levels (pH 4.2-4.6). A comparison of soluble metal concentrations (C, D) show clay suspensions kill bacteria by maintaining metal solubility over 24h, while (E, F) leachates precipitate metals only inhibiting growth.

The antibacterial activity of mineral suspensions occurs when clay concentrations increase to levels that lower solution pH (< 5), while sustaining metal release and ROS (i.e. hydrogen peroxide, H_2O_2) production (Figs. 5.1, 5.2). Leachates at similar concentration, without the clay buffer, precipitate metals and H_2O_2 production stops (Fig. 5.1, 5.2). Leachate MBC for *E. coli* occurs at low pH (3.4), while clay suspensions are bactericidal above pH 4, showing that pH alone is not killing bacteria (Fig. 5.1B). Synthetic metal mixtures of Fe^{2+}, Fe^{3+} and Al^{3+}, simulating leachate concentrations,

produced similar MIC and MBC (Appendix F, Table 5.3), supporting Fe and Al as primary bactericidal agents. The metal combination is more toxic than single metal solutions (Appendix F, Tables 5.2 and 5.3). Increases in pH occur when clay leachates are mixed with growth media due to metal speciation, causing Fe^{3+} and Al^{3+} precipitation, which reduces bioavailability (Fig. 5.1 C-F). This is an important point because many toxicity studies have not considered precipitation and bioavailability of metals to bacteria (Nies, 1999; Harrison et al., 2005). We assessed bioavailability of metals derived from the blue clay, by measuring soluble metals in different growth media (Fig. 5.1 C-F). Unbuffered solutions precipitate metals, requiring higher concentrations for toxicity. However, clay suspensions buffer pH while sustaining Fe^{2+} and Al^{3+} release.

The oxidation of pyrite has been shown to generate H_2O_2 which reacts with Fe^{2+} to form hydroxyl radicals (·OH) (Schoonen et al., 2010). The hydrated clay reaches redox conditions (Eh > 500 mV), oxidizing pyrite and producing H_2O_2 (Fig. 5.2). Clay suspensions produced H_2O_2 over 24h, while aqueous leachates ceased H_2O_2 production after 2h in both MSA and LB media (Fig. 5.2 A, B). Therefore, metal solutions alone are limited as a bactericide. However, by providing a constant source of soluble Fe^{2+}, Al^{3+} and ROS, the clay kills bacteria at lower metal concentrations. Pyrite oxidation by molecular O_2 can directly generate H_2O_2 on the crystal surfaces (Schoonen et al., 2010). However, at low pH (< 4.5) pyrite can also be oxidized by Fe^{3+}, releasing soluble Fe^{2+} that can also produce H_2O_2 and ·OH (Schoonen et al., 2010). The expandable smectite component of the Blue clays may serve as a reservoir for Fe^{2+}, as divalent cations are preferred over trivalent cations in the smectite interlayer, providing extended Fe^{2+} release when cation exchange occurs during rehydration for medicinal application (Moore and

Reynolds, 1997; Morrison et al., 2014). These combined oxidation reactions can explain the elevated H_2O_2 levels observed in the Blue clay suspensions, leading to sustained ROS production, killing pathogens via geochemical process (Fig. 2).

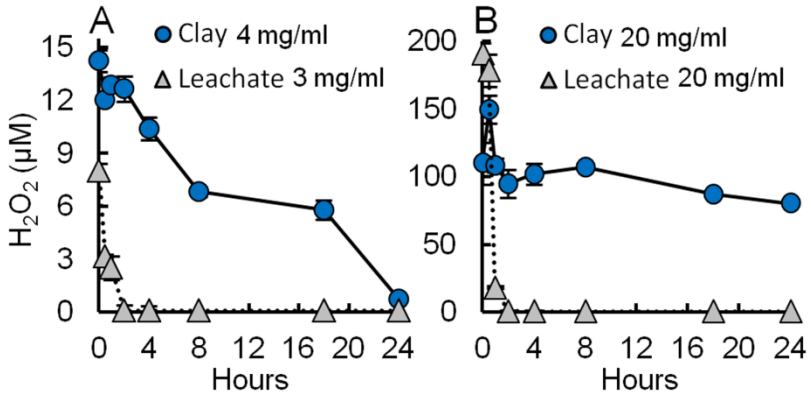

Figure 5.2. Hydrogen Peroxide. Generation of H_2O_2 is maintained by clays suspensions in (A) MSA and (B) LB-media, while leachates cease production after 2h. These data show that clay suspensions sustain metal release and H_2O_2 production that leads to cell death.

5.2.2 Metal Hydrolysis

Pyrite is present in the blue clay (~5%) which can produce H_2SO_4 during oxidation (Schoonen et al., 2010; Morrison et al., 2014). The hydrolysis of soluble metal cations can also generate acidity as metals precipitate (Pearson, 1966). To determine if metal hydrolysis resulted in acidic conditions during precipitation we measured the pH and solubility of individual metals (Fe^{2+}, Fe^{3+} and Al^{3+}) at MIC and MBC levels. We found that bacterial metal toxicity is linked to solution pH and solubility, with acidic metal cations (Al^{3+} and Fe^{3+}) generating the most acid (Fig. 5.3). At MIC and MBC, the pH and solubility of individual metals correlates with their pKa (acid dissociation constant). Fe^{3+} and Al^{3+} hydrolysis generates acidity (eqn. 1), while precipitation occurs

at pH values > pKa (Pearson, 1966). The amount of acid generated through metal hydrolysis is greatest for $Fe^{3+} > Al^{3+} > Fe^{2+} > Ca^{2+}$. Therefore, acid production from Fe^{3+} and Al^{3+} hydrolysis reaction are an overlooked aspect of metal toxicity and may enhance the toxicity of other metals with low pKa values (< 5) (Fig. 5.3). We observed that leachates and synthetic metal mixtures produced similar pH, indicating that metal hydrolysis plays a greater role in lowering pH than pyrite oxidation in the Oregon Blue clays (Appendix D, Table 5.3).

$$[Fe^{3+}(H_2O)_6]^{+3} + 3\ H_2O \leftrightarrows [Fe^{3+}(H_2O)_3(OH)_3] + 3\ H_2O + 3\ H^+ \qquad \text{(eqn. 1)}$$

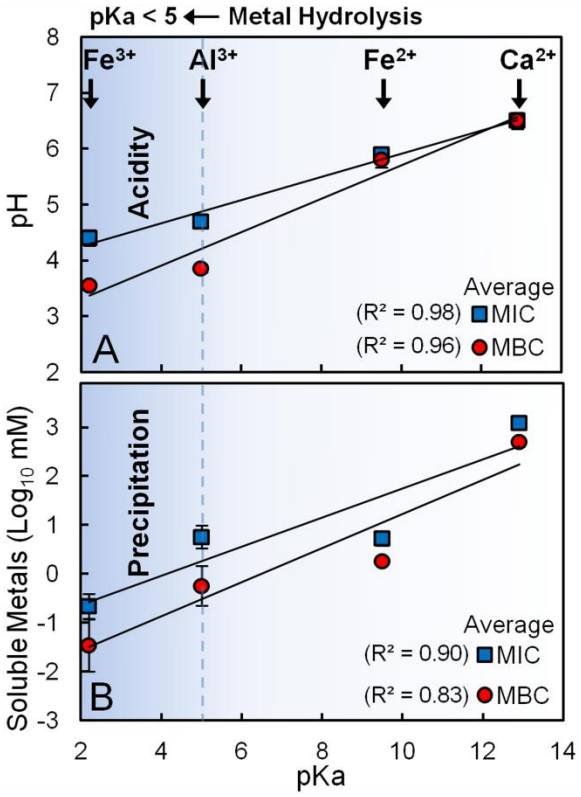

Figure 5.3. Metal hydrolysis reactions generate acidity; therefore, pH, metal solubility and toxicity correlate with pKa. These plots show average MIC and MBC for individual metals in MSA and LB media correlating with (A) pH and (B) soluble metal content.

5.2.3 Bioimaging

Bacteria adsorb a range of metals on their cell envelopes due to a high anionic charge density from phosphate and carboxyl groups (Beveridge and Koval, 1981; Fein et al., 1997). We used elemental bioimaging to examine the adsorption, redox state and location of metals reacting with *E. coli*. Clay suspensions (100 mg/ml) reacted with *E. coli* were analyzed *in situ* using synchrotron scanning transmission X-ray microscopy (STXM) for C, K, Ca, Fe^{2+} and Fe^{3+} (Fig. 5.4 A-C).

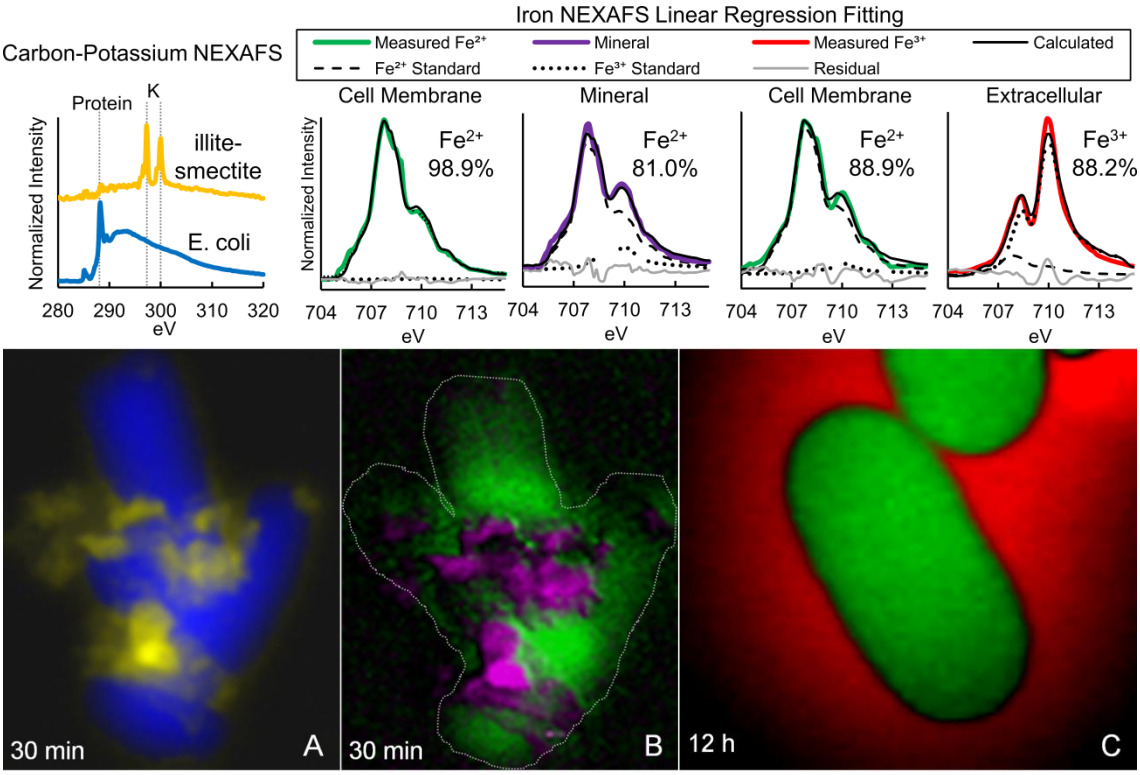

Figure 5.4. STXM elemental maps of *E. coli* reacting with a mineral suspension with corresponding NEXAFS spectra above each map. Elemental maps showing (A) protein-C from cells (blue) and K (yellow) from illite-smectite (I-S), (B) Fe distribution, showing Fe^{2+} adsorption on *E. coli* (green) and Fe in I-S particles (purple), (C) *E. coli* cells after 12h showing continued Fe^{2+} (green) adsorption, leaving Fe^{3+} (red) in extracellular solution. Percentages of Fe^{2+} and Fe^{3+} were calculated using ferrous and ferric iron standards from Dynes et al., 2006.

Near edge x-ray absorption fine structure (NEXAFS) spectra of C and K show K-rich particles adhered to cells (Fig. 5.4 A). Illite-smectite (I-S) dominates the deposit mineralogy (Morrison et al., 2014) and is the likely source of K in these particles. Linear-regression fitting of Fe spectra with reference compounds (Dynes et al., 2006), shows Fe in I-S particles (Fig. 5.4 B, C), is mostly Fe^{2+} (81%), possibly in exchange sites of I-S. Soluble Fe^{2+} (89-99%) is adsorbed preferentially to cell envelopes (Fig. 5.4 B, C), while Ca^{2+} remains in solution (Appendix E. Fig. 5.9). In *E. coli*, Ca^{2+} and Mg^{2+} adsorbed to phosphate-rich lipopolysaccharides provide outer membrane stability; however, under acidic conditions H^{+} can displace these cations (Borrok et al., 2004).

Nano-scale secondary ion mass spectrometry (NanoSIMS) maps of C, Al and Fe were measured to determine their binding sites in the cell (Fig. 5.5). Cells were measured after reaction with a 100 mg/ml Blue clay suspension for 12hrs. A clump of *E. coli* cells were sputtered with the primary ion beam, exposing the cell interior and Fe and Al maps were generated. The images show that Al binds to bacterial membranes, while Fe enters the cell (Fig. 5.5 B). *E. coli* that were not reacted with Blue clay showed no intracellular Fe (below detection limit), consistent with previous studies indicating 354 and 2662 ppm intracellular Fe concentrations in control and clay reacted cells respectively (Williams et al., 2011). The mechanism for Al toxicity is unknown, but it has been shown to compete with Ca and Mg for phosphate binding (Williams, 1999). Previous measurements of extracellular elements in *E. coli* reacted with the Oregon Blue clay leachates indicate that Fe and Al replace membrane bound Ca and Mg (Williams et al., 2011).

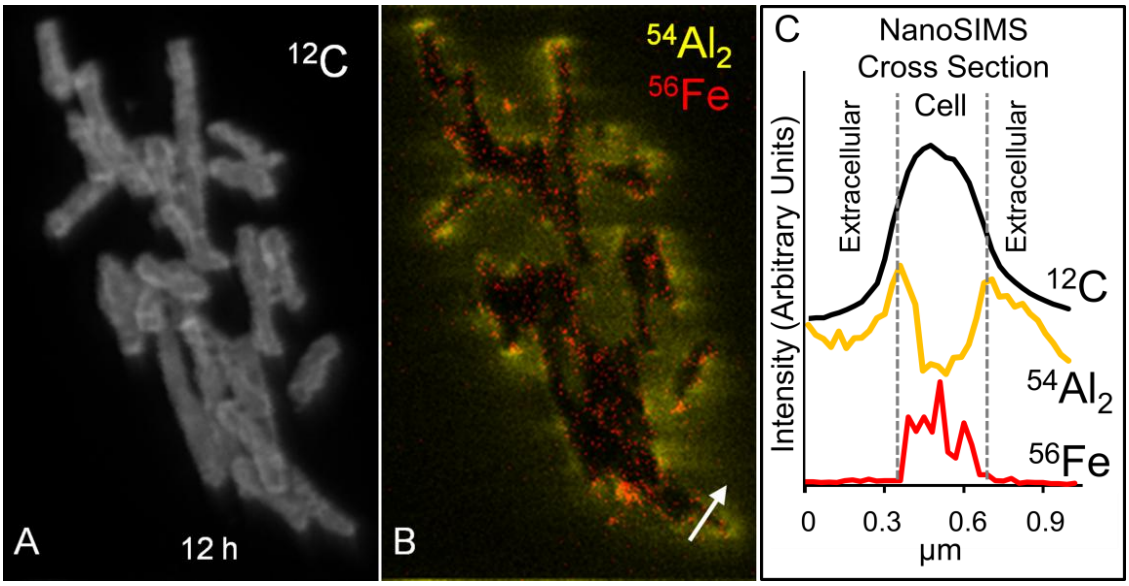

Figure 5.5. NanoSIMS image of *E.coli* showing, (A) ^{12}C map of cells, (B) $^{54}Al_2$ outside and ^{56}Fe inside cells. (C) A cross section of ion counts across the white arrow in (B).

The composition of the intracellular nano-particles was measured using scanning transmission electron microscopy-electron energy loss spectra (STEM-EELS). Figure 5.6 shows STEM dark field images of *E. coli* cells reacted with a mineral suspension (100 mg/ml) and fixed using high pressure freezing. EELS measurements of intracellular and extracellular particles reveal the presence of O-K edge and Fe-$L_{2,3}$ edge spectra. Accumulations of mineral particles outside the cell appear to be 20-100nm Fe-oxide particles (Fig. 5.6 A). The intracellular nanoparticles are smaller in size (< 10 nm) and are also Fe-oxides. A second EEL spectrum of the intracellular particles was measured at a resolution of 0.3 eV revealed only Fe^{3+} particles at 709.5 eV (Fig. 5.6 D). Other elements that may play a role in antibacterial processes (e.g., Al, Cu, Zn) were not detected intracellularly. Williams et al., (2011) suggested that a flood of Fe^{2+} through the cell wall might have generated intracellular reactive oxygen species (ROS) responsible for the

cytoplasmic condensation, resulting in precipitated Fe^{3+} nano-particles, however the composition of the electron dense particles was not confirmed. Here, results from the STEM-EELS confirm that these particles are Fe^{3+}-oxides (Fig. 5.6).

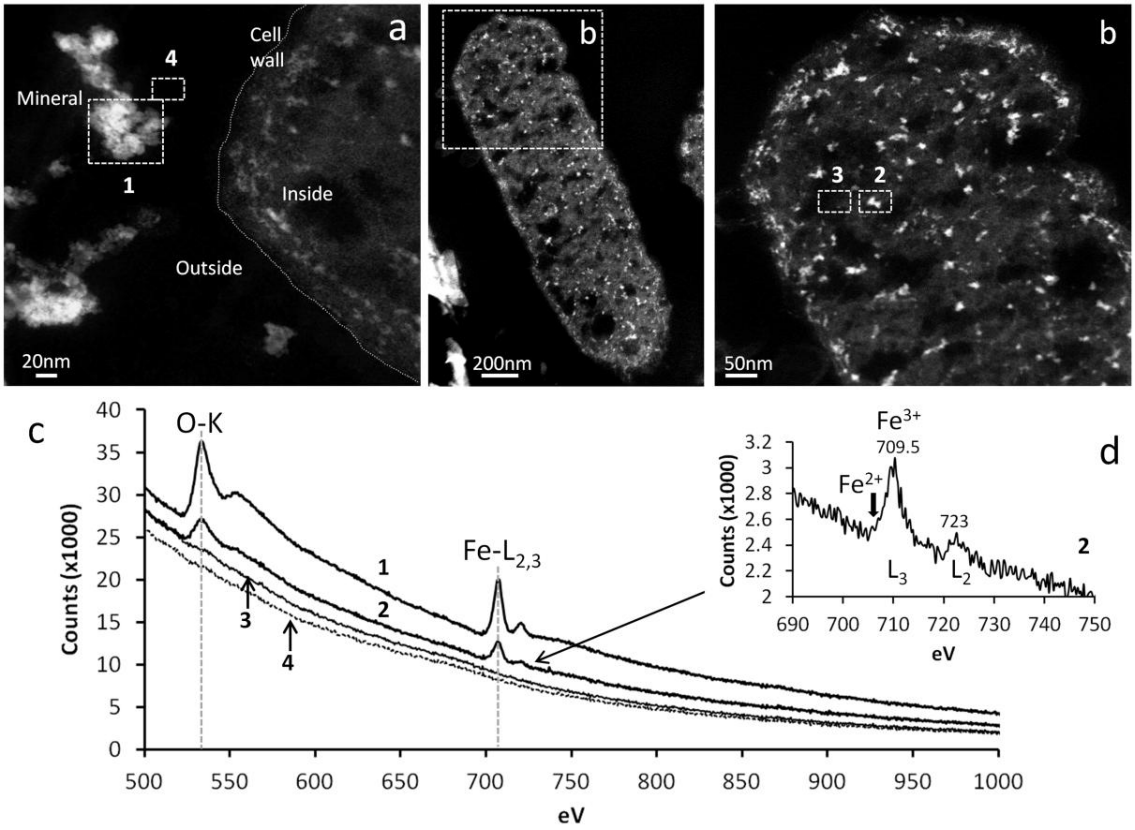

Figure 5.6. STEM dark field images (contrast reversed from TEM images, Fig. 5) and electron energy loss (EELS) in eV of *E. coli* reacted with a 100 mg/ml Blue 1 mineral suspension for 24 hours. (A) Mineral particles outside the cell range in size from 20-100nm; (B) intracellular particles (<10 nm) are shown in two separate images; (C) EELS spectra of the oxygen K edge (533 eV) and iron $L_{2/3}$ edge (709.5 eV) with 0.5 eV resolution. Both the extracellular and intracellular mineral particles are composed primarily of iron and oxygen. (D) The iron $L_{2/3}$ edge of the intracellular particles measured at 0.3 eV resolution reveals the presence of Fe^{3+} at 709.5 eV, while Fe^{2+} at 707.5 eV was below detection.

The STXM and NanoSIMS bioimaging results reveal that bacterial membranes remain enriched in Fe^{2+} and Al^{3+} throughout the antibacterial process. The STEM-EELS images show Fe^{3+}-oxide particles inside the cells that likely formed from the oxidation of excess intracellular Fe^{2+} which may enter the cell through low affinity uptake (chemiosmotic) systems (Nies, 2003). Rapid Fe^{2+} uptake and oxidation to Fe^{3+} is likely responsible for the intracellular Fe-oxide nanoparticles due to the fact that Fe^{2+} is taken into the cell with rapid unspecific chemiosmotic uptake mechanisms while Fe^{3+} requires siderophore based transport (Nies, 2003). If cytoplasmic Fe^{2+} levels exceed cellular demand oxidation to Fe^{3+} and storage in ferritin occurs in order to keep free Fe^{2+} at low concentrations (Smith, 2004). The influx of Fe^{2+} into the cell could overwhelm iron storage proteins potentially leading to toxic levels of free Fe^{2+}, while oxidation leads to precipitation of iron oxide nanoparticles which cannot be removed by efflux. As these intracellular iron nanoparticles are precipitating, ROS may also be generated leading to more oxidizing conditions inside the cell. The STEM-EELS and EDS (data not shown) analysis did not reveal the presence of intracellular Al^{+3}, nor have bulk analytical methods indicated that Al^{3+} is entering the cell (Williams et al., 2011). Trivalent Al does not normally diffuse through cell walls (Neis, 1999; Williams, 1999) and if it is chelated and makes it through the membrane, the cells quickly expel it (Williams, 1999). At low pH (< 4.5) $AlOH^{2+}$ may be stable on the cell wall, competing with Ca^{2+} binding sites, and can lead to precipitation of aluminosilicates (Urrutia and Beveridge, 1995).

5.2.4 Protein Oxidation

Hydroxyl radicals (·OH) are generated as Fe^{2+} is oxidized by H_2O_2 through the Fenton reaction (Imlay et al., 2008). The proximity of ·OH generation is crucial to toxicity because they exist briefly (10^{-9} s half-lives) with nanometer diffusion distances (Winterbourn, 2008). Thus, Fe^{2+}-enriched bacterial membranes (Fig. 5.4 C), reacting with H_2O_2 from the clays (Fig. 5.2), will generate ·OH in direct proximity to membrane proteins and lipids. We evaluated protein oxidation by measuring carbonyl content (Levine et al., 1990) in separated membranes and soluble protein fractions of *E. coli* reacted with clay leachates and metal solutions (Fig. 5.7 A). Membrane fractions of *E. coli* showed the greatest protein oxidation (30-60 nmol-carbonyl/mg-protein) upon exposure to leachates and metals, while soluble protein fractions (dominated by intracellular proteins) had lower carbonyl content (4-7 nmol/mg). This indicates that bacteria exposed to antibacterial clays first experience ROS stress targeting membranes, followed by gradual intracellular protein oxidation.

5.2.5 Genetic Stress Responses

Our results show that the synergistic activity of Fe^{2+}, Fe^{3+} and Al^{3+} produces greater toxicity at lower concentrations than individual metals. LacZ reporter gene fusions were employed to quantify bacterial stress responses to clay leachates and metals (Huisman et al., 1984; Alba and Gross, 2004; Raivio, 2005). Genetic responses to envelope and DNA stress were evaluated in MSA-media using *rpoHP3*::*lacZ* (σ^E-response) and *sulA*::*lacZ* (SOS-response) constructs (Fig. 5.7 B-E). Outer membrane protein (OMP) misfolding from ROS can activate the σ^E-response, transcribing genes

whose products regulate OMP proteolysis and folding (Alba and Gross, 2004; Raivio, 2005). Leachates caused the greatest activation of the σ^E-response, increasing *rpoHP3*::*lacZ* expression 4 fold upon reaction with a 1mg/ml leachate solution (Fig. 5.7 B, C). Weaker envelope stress occurred for individual Fe^{2+} and Al^{3+} solutions, requiring 77% more metal to reach leachate stress levels. This further supports the synergistic role of Al^{3+} and Fe^{2+} for membrane damage. Misfolding of OMPs by Al^{3+} may aid in protein oxidation by exposing amino acids to ·OH attack, supporting Al as a pro-oxidant (Exley, 2004). Pathogenic Gram-negative bacteria activate the σE-response to protect against ROS generated by host macrophages (Alba and Gross, 2004). These results demonstrate that metal binding to envelopes and ROS are capable of misfolding proteins. Consequently, antibacterial clays may act in a manner similar to macrophages by engulfing and killing bacteria with metal based ROS attack.

DNA damage triggers the SOS-response in *E. coli*, suspending cell growth until DNA is repaired (Huisman et al., 1984). Leachates and Fe^{2+} solutions produced similar DNA stress (Fig. 5.7 D, E), while Fe^{3+} and Al^{3+} alone were not genotoxic. Thus, intracellular stress results from excess Fe^{2+} uptake. *E. coli* take in Fe^{2+} through low and high affinity uptake systems (Feo, Zup), while trivalent cations (Fe^{3+}) must enter through high affinity siderophore systems (TonB-ABC transporters) (Andrews et al., 2003). Al^{3+} substitution in Fe-S proteins, resulting in free intracellular Fe and ROS stress, has been proposed as a mechanism of Al^{3+} toxicity in Gram-negative bacteria (Lemire et al., 2010). However, our bioimaging (Fig. 5.5) and genetic data show that Al does not enter the cell or trigger the SOS-response.

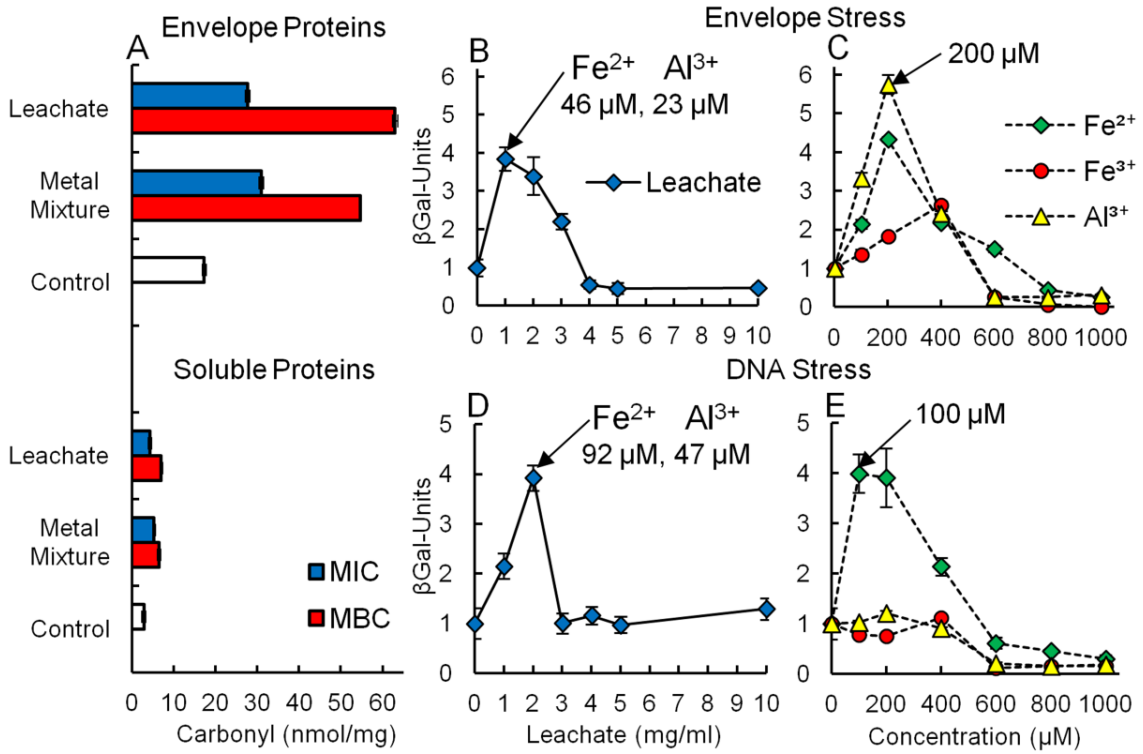

Figure 5.7. Bacterial stress responses. Clay leachates produce high levels of envelope protein oxidation, activating σE and SOS stress responses. Plots show (A) protein carbonyl content (nmol-carbonyl/mg-protein) measured in envelope vs. soluble protein fractions of *E. coli* reacted with leachates and metal mixtures in MSA media, at MIC and MBC concentrations. (B) Envelope stress measured by σE-response from LacZ fusions in leachates compared to (C) single metal solutions. (D) DNA stress measured on *E. coli* reacted with leachates, and (E) single metal solutions. LacZ results are normalized to levels measured in control *E. coli* (β-Gal Units).

5.3 Conclusions

The essential components for the antibacterial activity of the Oregon Blue clay are Fe^{2+}, Fe^{3+} and Al^{3+}, which work synergistically to overcome the highly evolved metabolic functions of human pathogens. The hydrated antibacterial clays generate a low pH (< 4.5) environment, through mineral oxidation, dissolution and hydrolysis reactions, sustaining metal release and ROS production throughout the antibacterial mechanism

(Fig. 5.8 A). Expandable smectite interlayer spaces provide a reservoir for Ca^{2+} and Fe^{2+} exchange. Pyrite oxidation by O_2 generates H_2O_2 on the mineral surfaces, while oxidation by Fe^{3+} releases Fe^{2+} into solution. Hydroxyl radicals are generated as Fe^{2+} is oxidized to Fe^{3+} by H_2O_2, providing additional Fe^{3+} for pyrite oxidation. Mineral dissolution (plagioclase and I-S) releases Al^{3+} and Ca^{2+} into solution. Hydrolysis of Fe^{3+} and Al^{3+} generate H^+, maintaining low pH (< 4.5), promoting mineral dissolution and metal solubility (Fig. 5.8 A).

The Oregon blue clays synergistically attack pathogenic bacteria by generating an oxidizing, metal rich environment that damages multiple cellular components (Fig. 5.8 B). Fe^{2+} and Al^{3+} both accumulate on cell envelopes, impairing membranes through protein misfolding (Al^{3+}) and oxidation (Fe^{2+}), activating the σ^E-stress response. Cell envelopes remain enriched in Fe^{2+}, providing a constant source of ·OH attack. Fe^{2+}, not Al^{3+}, floods the cytoplasm generating intracellular ·OH that damages DNA and proteins, marking oxidation sites with Fe^{3+}-oxide precipitates (Fig. 5.8 B). This constant intracellular oxidation causes single strand DNA breaks and overwhelms the cells defense mechanisms against ROS. The critical components identified in this natural antibacterial process should guide designs for new mineral-based antibacterial agents.

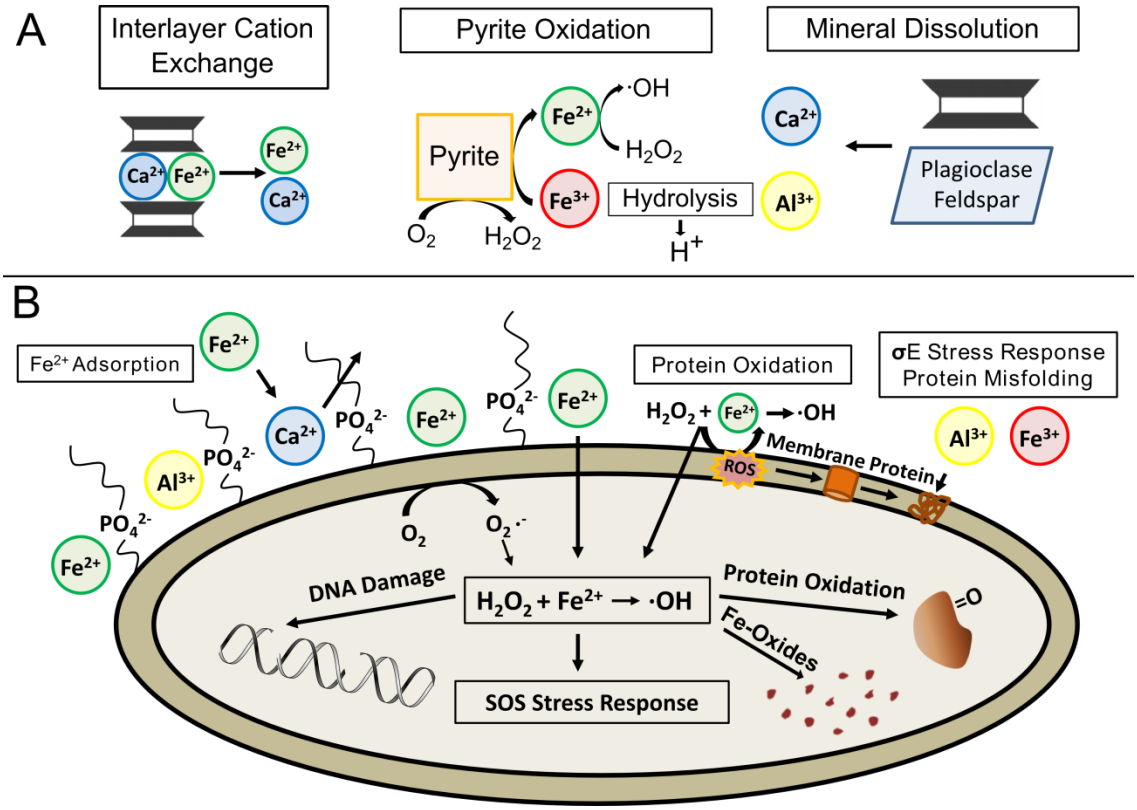

Figure 5.8. Antibacterial mechanism. Schematic showing the antibacterial mechanism of the Oregon Blue clays. (A) Illite-smectite interlayer cation exchange, pyrite oxidation and mineral dissolution (plagioclase feldspar and I-S) provide soluble Fe^{2+}, Fe^{3+}, Al^{3+} and Ca^{2+}, while generating H_2O_2. Hydrolysis and precipitation of Fe^{3+} and Al^{3+} sustain the acidic environment. (B) Fe^{2+} and Al^{3+} out compete Ca^{2+} binding to phosphate rich lipopolysaccharides on the outer membrane of *E. coli*, which results in protein misfolding and oxidation, activating the σ^{E}-stress response. Hydrogen peroxide generated extracellularly by clay suspensions diffuses through the cell envelope and reacts with intracellular Fe^{2+}, forming radicals that oxidize proteins and DNA, activating the SOS-response. Fe^{3+}-oxide precipitates coincident with cell death. Through extended metal release and H_2O_2 production, the Oregon blue clays simultaneously stress multiple cellular systems unlike traditional antibiotics.

Chapter 6

CONCLUSIONS, APPLICATIONS AND FUTURE RESEARCH

6.1 Summary of Findings

Clays are a mixture of < 2.0 μm minerals that have equilibrated with pore fluids in natural geologic environments. When antibacterial clays are taken from natural formations and hydrated at room temperature and pressure with de-ionized water, the minerals re-equilibrate and release metals through mineral dissolution, oxidation and cation exchange reactions (Williams et al., 2008; Morrison et al., 2014). This research shows that different mineralogical assemblages within the natural OMT clay deposit demonstrate varying antibacterial effectiveness on model Gram-negative and Gram-positive bacteria.

Selecting representative samples from different alteration zones, within the OMT deposit, we conclude that samples containing pyrite and mixed-layered illite-smectite at pH < 4.2 and Eh > 500 mV are effective at killing (100%) of the model pathogens tested (*E. coli* and *S. epidermidis*) by generating H_2O_2 and releasing > 1 mM concentrations of Fe^{2+}, Fe^{3+} and Al^{3+}. Samples without pyrite (white zone) also prevented bacterial growth, buffering solutions to acidic pH (< 4.7) and oxidizing Eh (> 450 mV) conditions, releasing lower amounts (< 1 mM) of Fe and Al. The mixed-layered illite-smectite plays an important role as a cation reservoir, producing the antibacterial effect observed in clays not containing pyrite. The dominant illite layers (in illite-smectite) may protect the expandable smectite layers from dissolution, allowing adsorption of Fe^{2+} (or other transition metals) into their stabilizing acidic interlayers. The mixed layered illite-

smectite also provides a delivery mechanism for metal release and maintains hydration during the clay application to wounds.

Because the hydrated clays remained bactericidal over a 24 hr period, this study focused on fluid chemical changes within this timeframe. The antibacterial effectiveness correlates with elevated concentrations of Fe^{2+}, Fe^{3+}, and Al^{3+} in the aqueous leachates. Metal hydrolysis reactions also maintain acidic pH levels, promoting metal solubility. The concentrations of Fe and Al alone do not explain observed antibacterial activity because they are below published MBCs for the bacteria tested. The antibacterial clays release a mixture of Fe and Al that combined kill bacteria at lower metal concentrations than the individual metal species, while maintaining metal solubility and ROS generation.

Bioimaging of bacteria by TEM, after exposure to aqueous mineral suspensions of the blue clay, showed no evidence of cell lysis; however cytoplasmic condensation and appearance of electron dense intracellular particles occurred after 8 hrs. These particles were determined to be Fe-oxides which formed from the rapid influx of Fe^{2+}, forming ROS that attack cell components and precipitate Fe^{3+} oxides. Fe^{2+} and Al^{3+} both attack the exterior of cells resulting in protein oxidation and misfolding. Evidence suggests that Al^{3+} remains adsorbed to the cell envelope, misfolding proteins, while Fe^{2+} enters the cell causing oxidative stress.

6.2. Topical Wound Healing

Using the information gathered in this study we propose a medicinal application of these natural clays that may promote wound healing. Chronic non-healing wounds typically exhibit more alkaline pH levels than acute wounds (Leveen et al., 1973; Gethin,

2007). The surface pH of healthy skin cells is slightly acidic (pH 4-6.3) which lowers potential bacterial colonization levels (Lambers, 2006; Schneider et al., 2007). High bacterial populations in chronic wounds shift the environment to more alkaline pH (7.3-8.9) and only heal upon transition to more acidic pH (4-6) conditions (Leveen et al., 1973; Gethin, 2007; Schneider et al., 2007). This increased alkalinity prevents the release of oxygen from hemoglobin, (Gethin, 2007; Leveen et al., 1973) causing a more reduced environment with Eh values ranging from -140 mV to -400 mV (Bullen et al., 2006). In healthy muscle tissue, Eh values are $\geq$ 300 mV, which helps keep iron oxidized (Fe^{3+}) and bound in transferrin (Bullen et al., 2006). When wound Eh falls below -140 mV (at pH 7.3-8.9), Fe^{3+} is reduced to Fe^{2+} and no longer bound by transferrin. This makes Fe^{2+} available for bacterial metabolic activities (Bullen et al., 2006).

Conventional thinking is that Fe^{3+} within chronic wounds is a limiting nutrient for bacterial growth due to its low solubility (10^{-18} M) at physiological pH (~7) (Ratledge and Dover, 2000). Iron in mammals is transferred in the blood stream by the proteins transferrin and hemoglobin while cellular storage occurs within ferritin. Pathogenic bacteria access this Fe through direct contact and siderophore production, degrading the host cells to access this iron (Ratledge and Dover, 2000). In fact, the use of iron chelating compounds to limit pathogenic bacterial growth has been employed as a treatment option for infections (Taylor et al., 2005). In contrast to the conventional medical strategy of limiting bacterial Fe supplies, Musk et al. (2005) suggested that excess Fe levels can perturb biofilm formation by repressing pathogen virulence factors associated with Fe acquisition (Musk et al., 2005). Therefore, careful applications of natural minerals such as the OMT blue clay, that generate excess soluble Fe and Al, may similarly limit

pathogenic bacterial growth and/or biofilm development. Furthermore, due to the highly absorptive surfaces of clay minerals (especially smectite), these clays may aid in wound debridement including removal of abnormal collagen tissue, and toxic bacterial products (e.g. NH_4^+, a preferred interlayer cation in smectite).

In many clinical trials, chronic wound acidification has been advocated as a treatment option (Leveen et al., 1973; Gethin et al., 2008; Kaufman et al., 1985) and successfully eliminated many problems associated with alkaline wound environments (Liu et al., 2002; Gethin, 2007; Schneider et al., 2007). Manuka honey and acidified nitrite are examples of acidifying agents (pH 3-4.5) that have been used in chronic wound care (Gethin et al., 2008; Weller et al., 2001; 2006). However, acidification with many weak acids (e.g., 1% acetic acid) can only maintain an acidic environment for up to an hour, so compounds that buffer an acidic environment, like the antibacterial clays, are needed (Leveen et al., 1973; Gethin et al., 2008). Another viable option for chronic wound healing is hyperbaric oxygen therapy, which raises tissue oxygen levels, promoting skin cell growth (Leveen et al., 1973: Roth and Weiss, 1994). Despite the fact that hyperbaric oxygen and acidified nitrite can produce damaging ROS and reactive nitrogen species (RNS), these therapies have been shown to promote skin cell growth (Weller et al., 2001; Alleva et al., 2005; Weller et al., 2006).

Similar to these accepted treatments of chronic wounds, the antibacterial OMT clays can stabilize aqueous environments to pH < 4 with elevated Eh (> 550 mV) relative to chronic wound environments (Fig. 6.1). The acidic OMT clays can maintain the low pH for many hours due to their buffering capacity and continued release of H^+ during pyrite oxidation. In mammalian cells, macrophages and neutrophils utilize a burst of ROS

to fight invading pathogens (Fang et al., 2004). However, the alkaline pH levels in chronic wounds lead to hypoxic conditions, making such a respiratory burst of ROS difficult (Roy et al., 2006). The application of antibacterial minerals to wounds may function in wound healing by lowering the pH of a chronic wound from alkaline conditions allowing the release of oxygen from hemoglobin while potentially generating reactive oxygen species resulting in a burst of ROS similar to those utilized by macrophages.

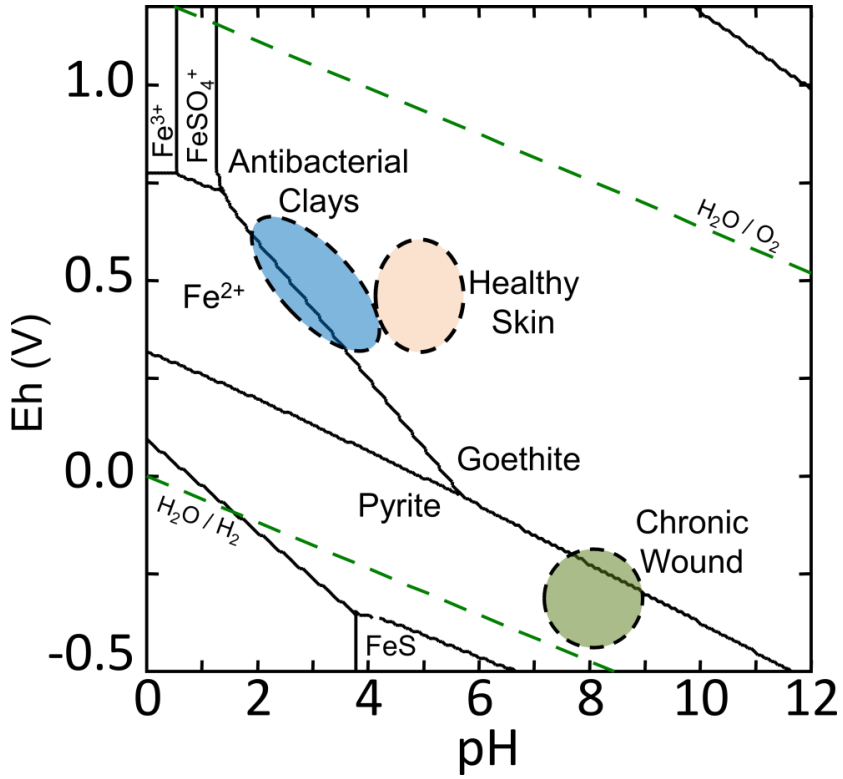

Figure 6.1. Chronic wound pH and Eh. Eh and pH mineral stability diagram of the Fe-S-O-H system. Iron and sulfur concentrations were 2 and 4 mM respectively. Dashed ovals represent the Eh and pH values found in chronic non-healing wounds (green), healthy skin (pink) and antibacterial clays (blue) (Leveen et al., 1973; Gethin, 2007; Bullen et al., 2006).

Antibacterial samples from the OMT deposit may shift the pH and Eh in chronic non-healing wounds to a range that favors healing while killing invading pathogens. The pH buffering capacity of mineral suspensions from the Open Pit mine were determined using NaOH titration of 100 mg/ml bulk clay suspensions. Titration curves for each sample are shown in Fig. 6.2. The titration curves demonstrate the ability of the antibacterial clays to buffer pH, whereas the non-antibacterial sample (red oxidized zone) does not contain an effective mineralogical buffer (Fig. 6.2). Clays containing antibacterial mineral assemblages that buffer solutions to healthy skin pH, Eh conditions and produce soluble Fe^{2+} and Al^{3+} could be a viable treatment option for chronic (non-healing) wounds infected with antibiotic-resistant bacteria.

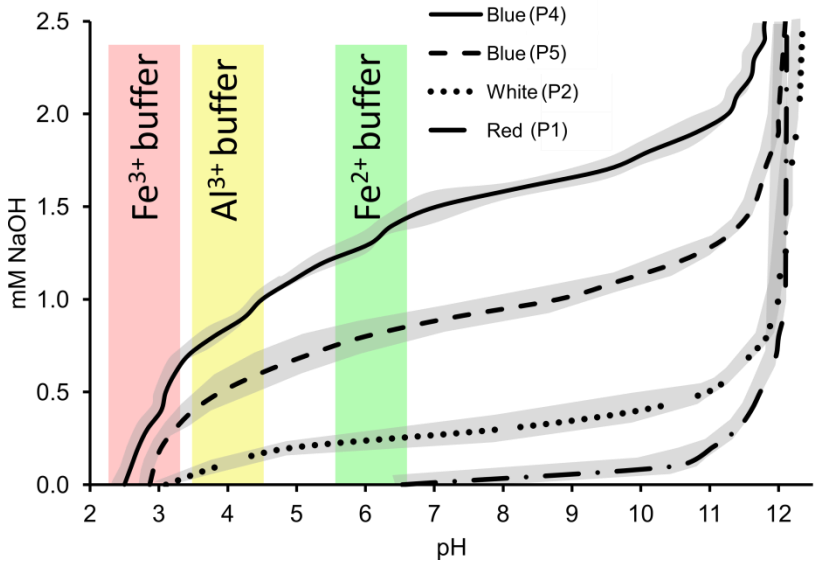

Figure 6.2. Mineral titrations. Titrations of 100 mg/mL mineral suspensions with NaOH (0.1 N). Gray regions outlining the titration curves represent the standard deviation of each sample run in triplicate. Zones for Fe^{2+}, Fe^{3+} and Al^{3+} buffering capacity shown in shaded regions (Dold, 2005; Totsche et al., 2006).

6.3. Discovery of New Antibacterial Deposits

The main goal of this research is to characterize the mineralogical and geochemical variables that relate to antibacterial effectiveness in hydrothermal clay deposits, providing a framework for identifying new antibacterial clay deposits. Such natural deposits may provide cost-effective topical antibacterial treatments, or lead to discovery of new antibacterial mechanisms that may ultimately benefit the health care industry and developing nations by providing a low cost topical antibacterial agent that is a product of natural hydrothermal alteration of volcanic deposits.

Porphyry alteration systems associated with subduction zones and arc volcanoes are prevalent worldwide, producing the hydrothermal alteration of large volumes of rock > 3 km away from the intrusive heat source (Singer et al., 2005; Pirajno, 2009) (Fig. 6.3). Porphyry deposits form at high temperatures (400°-7500°C) closer to the magmatic intrusion (2-6 km depth), forming mineralized stocks with porphyritic texture (Seedorff et al., 2005). Potassic alteration produces metal rich stockwork containing a range of disseminated sulfides (Fe, Cu, Mo, Pb, Zn) in addition to native Au, W, Bi and Sn (Pirajno, 2009). These potassic zones produce economically viable deposits with high grade ore at distances up to ~ 0.5 km from the intrusive body, with hydrothermal alteration extending laterally for several kilometers (Singer et al., 2005; Pirajno, 2009). Volcanic ash deposits may also be important sources of hydrothermally altered clays (Williams et al., 2008).

At greater distances from the magmatic heat source, potassic alteration transitions to zones of lower grade ore. These zones are characterized by, phyllic, argillic and propylitic alteration, resulting in clay minerals, quartz and sulfides (Meunier, 2005;

Pirajno, 2009) (see Chapter 3, Table 3.1 for alteration descriptions). Antibacterial clays may be present in many of these alteration zones more distant from the intrusive body and represent a novel economic use for these minerals. Using the OMT deposit as a model system for antibacterial clays we propose a simple and rapid sampling method using pH and Eh measurements to identify potential antibacterial clay zones for testing.

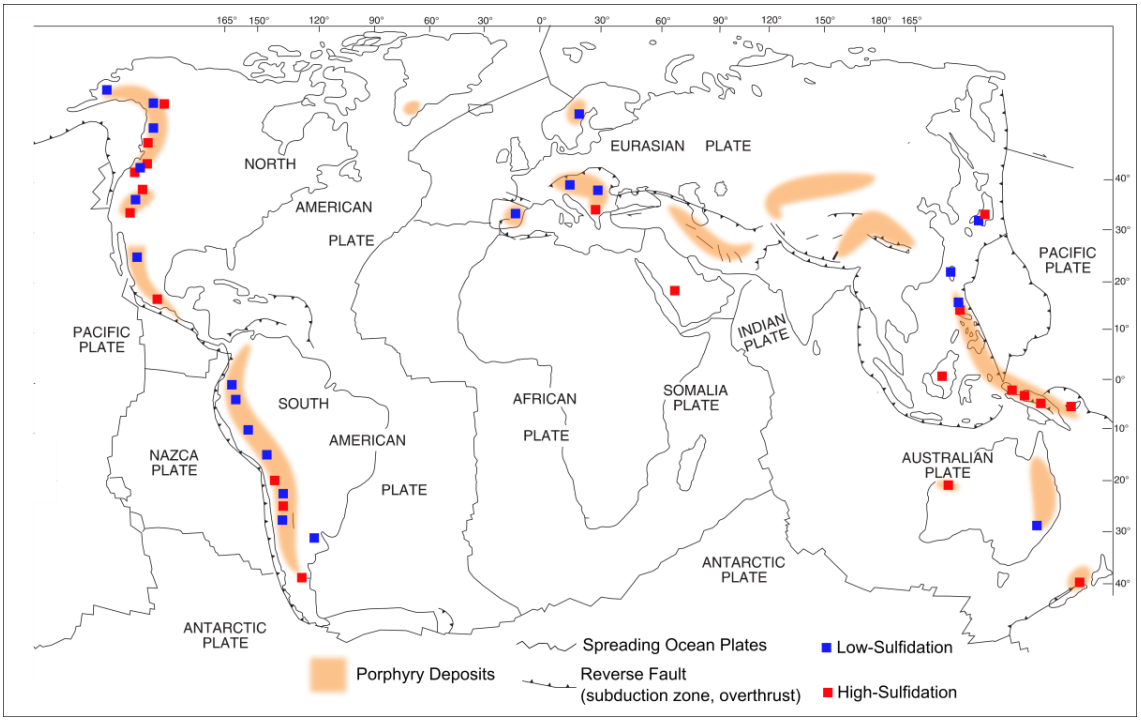

Figure 6.3. Global porphyry deposits. Zones of porphyry alteration and sulfidation states associated with the hydrothermal alteration (figure modified from Pirajno, 2009 and Seedorff et al., 2005). Locations of high and low-sulfidation alteration were gathered from Goodfellow, 2007.

The antibacterial clay zones identified in the OMT deposit formed from both high and low-sulfidation alteration, producing intermediate argillic clay zones containing illite-smectite (I-S), pyrite and quartz. The antibacterial activity depends on the pH and

Eh of the re-hydrated clays (100 mg/ml), which promotes mineral dissolution, oxidation and the release of soluble Fe^{2+}, $Fe^{3+}$and Al^{3+}. Hydrogen peroxide is also generated from the oxidation of pyrite and Fe^{2+}.

The most effective antibacterial clay zones formed under high-sulfidation alteration (Sulfur Mine black clays), killing 100% of a broad spectrum of human pathogens including antibiotic resistant strains. These zones contained high concentrations of < 20 µm disseminated pyrite (10-18%) along with I-S (70% illite) and quartz. Re-hydration of these clays resulted in low pH (~2) and high Eh (600-750 mV) solutions that released high levels of Fe^{2+}, Fe^{3+} and Al^{3+} (10-20 mM), generating up to 1.5 mM H_2O_2. The very low pH of these clays may damage skin tissue, so more work is needed to investigate how much pyrite is tolerable in human tissues, and other potential side-effects.

The blue antibacterial clays, formed from low-sulfidation alteration (pyrite 4-6%, rectorite and quartz), also killed antibiotic resistant bacteria (100%) when pH values and Eh values were < 4.2 and > 450 mV, respectively. The bactericidal samples from these zones occurred directly below oxidized surface layers where pyrite oxidation and mineral dissolution released 5-10 mM Fe and Al, while generating up to 0.6 mM H_2O_2. These milder conditions may be the right 'Goldie-locks zone' for killing bacteria, yet not damaging human tissue.

Samples collected at greater depth (> 1 m) in this zone had elevated pH (4.2-4.7) and low Eh (< 400 mV) and only inhibited bacterial growth, releasing < 1 mM Fe and Al. The complete oxidation of pyrite to goethite along with the presence of carbonates in the

mineral assemblage eliminated the antibacterial effect. These zones had neutral pH and Eh values < 400 mV when re-hydrated and released only µM amounts of Fe and Al.

Our research shows that pH and Eh measurements of rehydrated clay samples provides a simple reliable method to rapidly screen hydrothermal alteration zones for potential antibacterial activity. Samples can be collected, rehydrated (100 mg/ml) and measured directly in the field or dried (60°C) and measured later in the lab. Samples in the correct pH and Eh range can then be rapidly screened for antibacterial activity using the bacterial zone of inhibition method (Chapter 7.2.1). Table 6.1 outlines the protocol for identifying antibacterial clay zones based on the observed mineral assemblages, pH and Eh measurements.

Table 6.1.Protocol for identifying antibacterial clay zones in hydrothermal deposits. Mineral samples were rehydrated with deionized water using a 100 mg/ml mineral/fluid ratio.

Antibacterial Activity	Alteration Type	Mineral Assemblage	pH	Eh (mV)
Bactericidal	High, Low-sulfidation	Pyrite (>4%), Illite-smectite, Quartz	< 4.2	> 450
Growth Inhibition	Low-sulfidation	Pyrite (4-6%), Illite-smectite, Quartz	4.2 - 4.7	> 400
Growth Inhibition	Low-sulfidation, Leached White Zone	Illite-smectite, Quartz	4.2 - 4.7	> 400
Non-Antibacterial	Low, High-sulfidation, Carbonate Zones, Oxidized Surface Zones	Carbonate, Goethite	5 – 7	< 400

Chapter 7

METHODS

7.1 Mineralogy and Solution Chemistry

7.1.1 X-ray Diffraction

X-ray diffraction was performed using a Siemens D5000 diffractometer (ASU LeRoy Center for Solid State Science) using CuK_{α} radiation. Clay fractions (<2.0 μm) were separated to make oriented clay slides for XRD. Bulk samples (5 g) were crushed and passed through a 500 μm sieve. The crushed samples were then placed in 50 ml of de-ionized water (DIW) and sonicated for 1 minute to disperse the clay minerals. Samples were then centrifuged with a swinging bucket centrifuge at 1200 rpm for 3 minutes to separate the <2 μm fraction (Moore and Reynolds, 1997). The supernatants containing the <2 μm fraction were transferred into a 1000 ml flask. This procedure was repeated until supernatants were clear after centrifugation, indicating that the majority of the clays had been separated. The clay fractions collected in the 1000 ml (~500 ml) flask were then mixed with 500 ml of a 1 M NaCl solution which causes the clays to flocculate. The deposited clays were then exchanged with 1 M NaCl three times. The Na-exchanged clays were then transferred into dialysis tubing (3500 molecular weight cutoff) and rinsed with DIW to remove excess salts. Oriented clay samples were prepared (<2.0 μm Na-exchanged) by pipetting a clay suspension (20 mg/ml) onto a glass slide and air drying. The clay slides were then saturated with ethylene glycol in a sealed container at 60°C overnight (Moore and Reynolds, 1997). XRD patterns of mixed-layered clay minerals were calculated using Sybilla© modeling software (Chevron proprietary, cf. McCarty et al., 2008).

Bulk samples, prepared for quantitative random powder XRD, followed procedures reported by Eberl (2009). Samples were crushed after drying at 60 °C overnight, and passed through a 250 μm sieve. Sieved samples were spiked with 20% αAl_2O_3 as an internal standard and micronized in ethanol using a McCrone Mill then dried at 60 °C overnight. The micronized samples were then saturated with Vertrel® to promote random orientation, sieved and side-loaded into an XRD mount. All powdered samples were analyzed using a Siemens D-5000 XRD, using a scintillation detector with 1° divergence and receiving slits using CuK_α radiation, scanning from 5° to 65° at 0.02° 2θ steps with a 2 second per step count time. Quantitative mineralogy was calculated using the full pattern peak fitting program RockJock 11 (Eberl, 2009). The degree of fit between the measured and calculated XRD patterns was determined using equation 1 shown below. XRD patterns were fit from 19-64.5° 2θ and all degrees of fit were <0.1 which corresponds > 95% convergence of the fit (Appendix A1).

$$Degree\ of\ Fit = \sum \frac{(Measured - Calculated)^2}{Calculated} \qquad (1)$$

7.1.2 X-ray Fluorescence

Elemental analysis was performed on borate glass fusions of bulk rock samples (Baedecker, 1987) using a Siemens SRS 300 AS XRF spectrometer (USGS, Boulder CO). Samples (2 g) were heated to 925°C for 2 hours, cooled and mixed with lithium tetraborate-metaborate (66% tetraborate, 33% metaborate) in a 1:10 ratio. Borate glass fusions were prepared using an automated XRF fusion machine (XRF scientific). Samples were transferred to platinum/gold crucibles and progressively heated to 1100°C

under constant mixing and poured into casting molds to cool. The sum of all major element oxides which are not volatile at 1100°C, were calibrated with reference standards, totaled 97-98%.

7.1.3 Secondary Ion Mass Spectrometry

Microanalysis of $\delta^{18}O$ isotope ratios in quartz was performed to help resolve the sources of hydrothermal fluid (magmatic, meteoric or mixed) that lead to the formation of the OMT clay alteration zones. The open pit blue zone and oxidized white zone were sampled, along with the black clay zones in the sulfur mine. The open pit major mineral assemblage (quartz, pyrite, rectorite) is characteristic of low-sulfidation epithermal alteration where magmatic and meteoric fluids potentially mixed. The sulfur mine alteration minerals (quartz, pyrite, S^0, and I-S 70% illite) are consistent with higher temperature fluids, but whether they had a magmatic or meteoric origin is indicated by the mineral O-isotope composition, reflecting isotopic equilibrium with the fluid.

The clay size fraction was removed from samples to concentrate quartz crystals that were disseminated through the alteration zones. Bulk samples were dispersed in DDI water and sonicated to break apart mineral aggregates. The larger quartz crystals (50-100 μm) rapidly settled out of solution, leaving the remaining clay fraction in solution. The suspended clays were decanted and the remaining coarse sample fraction was dried. Quartz crystals were selected under a microscope and epoxy grain mounts were made using a low volatile epoxy (Buehler Epoxy-Cure) and polished to 1μm flatness (Hervig et al., 1992; 1995). The mounts were rinsed in a sonic bath with DDI water to remove

polishing material, dried at 60°C and Au-coated for charge compensation during solid-state isotope analysis.

Oxygen isotope measurements were made using a Cameca IMS 6f secondary ion mass spectrometer (SIMS) (ASU National SIMS Facility). SIMS microanalysis of oxygen isotopes in quartz was performed according to the methods of (Hervig et al., 1992; 1995), which are optimized for measuring oxygen isotopes in silicate minerals. A 10 kV Cs^+ ion beam with a 5 to 10 nA current was focused into a 20-40 μm spot for analysis of the polished quartz grains. The spectrometer was set to a mass resolving power of ~2100. The buildup of positive charge from Cs^+ ion bombardment of the quartz surface was offset by the use of a normal incidence electron gun, which focuses high-energy electrons (~ 3000 eV) on the sample surface (Hervig et al., 1992) for charge compensation. Extreme energy filtering of the negative secondary ions sputtered from the quartz was achieved using a -350 eV offset, which only allows secondary ions with > 350 eV to pass into the mass spectrometer, and eliminates interferences from molecular ions (Hervig et al., 1992; 2006). The combination of extreme energy filtering and lower mass resolving power provides high ion yields, removes interferences and avoids the lower transmission and ion counts associated with high mass resolution analysis alone (Hervig et al., 2006). The standard error for multiple measurement of a single crystal (4-8 analyses) ranged from 1.0-1.8‰, 1σ.

All $^{18}O/^{16}O$ ratios were standardized to the $^{18}O/^{16}O$ ratio of standard mean ocean water (SMOW, 2.0052E-3) and verified using an internal quartz standard (Arkansas quartz, +18.5‰ $\delta^{18}O$; Baertschi, 1976). Quartz standard $^{18}O/^{16}O$ ratios were measured before and after the analysis of each sample to correct for changes in instrumental mass

fractionation due to instrument drift (Hervig et al., 2006). All oxygen isotope ratios are expressed using delta (δ) notation (eq. 1), and reported in parts per thousand (‰) (Faure, 1998).

$$\delta = \left(\frac{R\left(\frac{O^{18}}{O^{16}}\right) Sample}{R\left(\frac{O^{18}}{O^{16}}\right) Standard} - 1 \right) \text{x } 1000 \text{ ‰} \qquad (1)$$

7.1.4 Cation Exchange Capacity

Cation exchange capacity (CEC) is a standard measure of the quantity of exchangeable cations that each clay sample can hold (Meunier, 2003). CEC measurements were determined using cobaltichexamine chloride (Co(III)-hexamine) absorbance at 470 nm following methods of Aran et al. (2008) and Derkowski and Bristow (2012). First, bulk mineral powders were placed in dialysis tubing and rinsed with ~2 L of distilled-deionized (DDI) water 10 times to remove excess cations. Samples were dried (120 °C overnight) prior to measurement, then 0.5-1 g portions were mixed with 25 mL of Co(III)-hexamine solutions (14.95 mM for clay standards and 7.48 mM for samples) (Derkowski and Bristow, 2012). Samples were then sonicated for 2 minutes, shaken for 1 hour and centrifuged (13,000 rpm, 10 min). The Co(III)-hexamine replaces exchangeable cations on mineral surfaces. Absorbance of supernatant solutions (at 470 nm) allowed measurement of molar concentrations of Co(III)-hexamine absorbed by clays to be deterined. All CEC values are reported as milli-equivalents of charge per 100 g of sample (meq/100g).

7.1.5 Leachate Elemental Analysis

Prior application of antibacterial clay poultices exhibited bactericidal activity over 24 hour time periods and were changed daily (Williams et al., 2004). Clay mineral leachates were also prepared to determine the role that soluble cations may be playing in the antibacterial process (Williams et al., 2011). Aqueous clay leachates were prepared by ultra-sonicating 100 mg/mL of bulk clay samples with deionized water (1 min), followed by shaking (24 hrs) to chemically equilibrate to the same degree represented by poultice applications, and finally centrifuged (13,000 rpm, 1 hr) to separate minerals from the leachate. Elemental analyses of mineral leachates were performed using a Thermo X-Series quadrupole ICP-MS (ASU, W.M. Keck Laboratory for Environmental Biogeochemistry). Samples were acidified (nitric acid, 2 %) prior to analysis. Dilutions of 1:10 and 1:100 were analyzed along with undiluted samples and calibrated to multi-element reference standards. Elemental concentrations were determined for: Na, Mg, Al, P, K, Ca, Ti, V, Cr, Mn, Fe, Co, Ni, Cu, Zn, As, Se, Rb, Sr, Mo, Cd, Cs, Ba, Hf, W, Ag, Hg, Pb, and U. Certain elements (e.g., Si and S) are not ionized efficiently by ICP-MS or have interferences, therefore were not included in the analyses.

7.1.6 Ferric and Ferrous Iron Assay

Mineral leachates were measured for Fe^{2+}, Fe^{3+} and total iron immediately after centrifugation to remove minerals, using a phenanthroline method modified from Anastácio et al., (2008). The measurement of Fe^{2+} was performed under red photographic bulbs to prevent the photochemical reduction of the binuclear Fe^{3+}-phenanthroline complex to the Fe^{2+}-phenanthroline complex (Komadel and Stucki, 1988). For the

measurement of Fe^{2+} a 50-500 µL aliquot of leachate was added to 1 ml of 2.5 wt. % 1,10 phenanthroline (dissolved in 95% ethanol). The solutions were then diluted with 1 wt. % sodium citrate. Absorbance was measured with a spectrophotometer at 510 nm wavelength after 15 min for color development. Measurement of Fe^{3+} was achieved in a similar manner using 200 µL of 10 wt. % hydroxylamine hydrochloride as a reducing reagent. Stock solutions of ferrous ammonium sulfate hexahydrate and ferric chloride (200 mg/l) were prepared and acidified using 3.6 N sulfuric acid, producing linear standard curves at concentrations ranging from 1-8 mg Fe per liter.

7.17 Hydrogen Peroxide Assay

H_2O_2 levels were measured for metal solutions, mineral leachates and mineral suspensions reacted with *E. coli* growing in MSA and LB media using a method modified from Cohn et al., 2005. Aliquots were sampled over a 24h period and centrifuged at 13,000rpm for 2min. Supernatants (500-20µl) were transferred into micro centrifuge tubes with the addition of 50mM EDTA. Buffer solution (1M KH_2PO_4, pH 4.2) was added to a final volume of 1400µl. Then 50µl of 5mM leuco crystal violet was added followed by 50µl of horseradish peroxidase type II (14.4 units/ml). Absorbance was measured with a spectrophotometer at 590 nm wavelength after 15 min for color development. Hydrogen peroxide standard curves ranging from 0.5-25µM were prepared in the same manner.

7.1.8 pH, Eh and Mineral Titrations

All Eh, pH and mineral titrations were measured using an Orion Dual Star pH, Eh meter (LE501 ORP and LE409 pH electrodes). The platinum Ag/AgCl (4 M KCl) Eh electrode was calibrated using Zobel solution resulting in a +220 mV offset with respect to a standard hydrogen electrode (Nordstrom, 1977). All titrations were run in triplicate using 20 ml of a 100 mg/ml mineral suspension which was continually stirred and titrated with 0.1 N NaOH in 1 mL increments to a total of 50 mL using a burette. The pH meter was allowed to stabilize 1-5 minutes between each addition of NaOH.

7.1.9 Speciation Modeling

Stability diagrams for the Fe-S-O-H, Al-S-O-H and S-O-H system were calculated using the MEDUSA program (Puigdomenech, 2004). Concentrations of Fe and Al were set at 2 mM, with 4 mM S levels. These values were chosen to reflect the chemistry of bactericidal samples in the OMT deposit. Bactericidal concentrations of leachate Fe and Al occur at ~ 1 mM concentrations, and the 2 mM concentrations modeled are well into the bactericidal levels. Williams (2011) measured the chemistry of anions leached from the OMT blue clays and sulfate was the major anion species. Sulfate concentrations (mM) were ~2 times greater than Fe, and this ratio was used for the calculations. Equilibrium constants for the plotted reactions are reported in Table A2.

7.2 Microbiology

7.2.1 Agar Diffusion Antibacterial Testing

A disc diffusion method was developed to rapidly screen a large sample set from different alteration zones for antibacterial effectiveness. This method provides a qualitative measure of antibacterial activity that we used to screen a large sample set. Cell viability plating (section 6.2.2) was then preformed on antibacterial samples identified using this method to determine if cell death or growth inhibition occurred. Antibacterial zones of inhibition were measured by a modification of the traditional Kirby-Bauer disc diffusion method of antibacterial testing (Bauer et al., 1966) described below. The antibacterial activity of the OMT deposit was determined by testing against antibiotic susceptible and resistant strains of Gram-positive and Gram-negative bacteria: *Escherichia coli* (ATCC 25922), (β-lactam resistant) BL *Escherichia coli* ATCC 35218 *Staphylococcus epidermidis* (ATCC 14990), methicillin-resistant *S. epidermidis* (MRSE) (ATCC 35948). Antibiotic susceptible strains (ATCC 25922 and 14990) were incubated (37°C) in Luria Broth (LB), grown to stationary phase (18 h) using a rotary shaker (200 rpm). The cells were diluted to ~10^8 CFU/ml before plating. Antibiotic resistant strains were grown for 48 h at 30°C without shaking to establish biofilms. After 24 h LB was removed from the culture tubes by pipette and a fresh aliquot of media was added. After 48 h planktonic cells were decanted and biofilms were scraped from the sides of the tube and shaken on a vortex mixer for 2 min and diluted to ~10^8 CFU/ml before plating. Next 100 µl of culture was spread over LB-agar plates (10 g/l) and four 8 mm diameter x 4mm deep wells were punched into LB-agar plates using a flame sterilized brass tube.

Bulk mineral samples were dried at 60°C, crushed in a mortar and pestle, passed through a 250μm sieve and autoclaved (121°C, 15psi, 30min) to sterilize. Mineral suspensions (100mg/ml) were prepared and sonicated for 1min to disperse the clays. The wells in the inoculated LB-agar plates were filled with 200μl of a 100mg/ml mineral suspension and incubated (37°C) for 24 hr. Elements leached from the clays diffuse into the agar creating a zone of growth inhibition that can be quantified by measuring the diameter of the zone. Each sample was analyzed in quadruplicate.

7.2.2 Antibacterial Susceptibility Spot Plating

Determination of bacterial growth inhibition vs. bactericidal activity of samples was achieved by spot plating serial dilutions of clay suspensions and cells. Colony forming units (CFU/ml) determined for *E. coli* ATCC 25922 and *S.epidermidis* ATCC 14990 using methods modified from (Miles and Misra, 1938; Hedges, 2002). The spot platting method produces only minor increases in standard error ~$4x10^7$ CFU/ml compared to traditional spread plating (~$2x10^6$ CFU/ml) (Hedges, 2002). Cultures were grown to log-phase and diluted to ~10^8 CFU/mL in LB. Mineral suspensions (200mg/ml) were then prepared and sonicated for 1min. Clays and bacteria were reacted in a 1:1 ratio containing a clay content of 100mg/ml and 10 g/l LB. Samples were incubated in a 96-well plate for 24 h on a rocking shaker. Serial dilutions of the samples (10^0-10^{-7}) were spot plated (10 μl) onto rectangular LB agar plates in quadruplicate using a multi-pipette and incubated at 37°C for 24 hr. Cells were counted using a magnified backlight. Growth inhibition values were defined by a 10^3 CFU/ml reduction in cells. Samples were considered bactericidal only if they killed 100% of cells in the undiluted sample.

7.2.3 *E. coli* Metal Toxicity

E. coli (ATCC 25922) metal toxicity measurements were performed in two different growth media, Luria broth and minimal salts and amino acids (LB, MSA) to evaluate effects of minimal and rich media on pH, metal solubility, and toxicity. The MSA media, modified from (Teitzel and Parsek, 2003), contained 1 g $(NH_4)_2SO_4$, 0.06 g $MgSO_4 \cdot 7\ H_2O$, 0.06 g $CaCl_2$, 0.02 g KH_2PO_4, 0.03 g Na_2HPO_4, 2.383g 4-(2-hydroxyethyl)-1-piperazineethanesulfonic acid (HEPES), 1 ml $FeSO_4$ (10 mM), 1% casein amino acids and 0.4 % glucose per liter. Rich (LB) consisted of 20 g per liter Luria Broth (LB) and 0.4 % glucose per liter. Overnight cultures of *E. coli* grown in 20 g per liter LB were diluted in MSA or LB media (1:50, 5 x 10^8 cells) and incubated at 37°C for 30 min. Aliquots (0.5 ml) of mineral leachates, metal solutions (Fe^{2+}, Fe^{3+}, Al^{3+} and Ca^{2+}) or metal mixtures of Fe^{2+} : Fe^{3+} : Al^{3+} (1.0 : 0.6 : 0.7 ratio) simulating the clay leachate proportions were then mixed with *E. coli* cultures (0.5 ml) in a 48 well plate (1:1 ratio of media: metal). Plates were incubated 37°C on a rocker plate for 24h.

Metal precipitation can prevent the accurate measurement of MIC values using visible wavelength spectroscopy Optical Density (OD) at 600nm. A method to remove excess metal precipitates without cell lysis was performed using an oxalic acid-EDTA mixture (Tovar-Sanchez et al., 2003; Williams et al., 2011). The oxalic acid-EDTA (Ox-EDTA) mixture consisted of 1.86g EDTA-Na_2-H_2O, 1.47g sodium citrate, 0.074g KCl, 0.5g NaCl and 1.26g oxalic acid adjusted to pH 8 with 10M NaOH. After 24 h of incubation with leachates or metals, 0.5 ml of culture was added to 0.5 ml of the Ox-EDTA reagent and reacted for 30 min. at room temperature. Cells were then pelleted and

re-suspended in 1ml Ox-EDTA reagent, reacted for 30 min., pelleted and re-suspended in 0.5 ml isotonic NaCl (0.9%). Metal rinsed cells were then transferred into a 98 well microplate and cell growth was measured at 600 nm with a microplate reader. MBC concentrations were determined by plating 50µl of culture in triplicate on LB-agar plates after 24h incubation at 37°C.

7.2.4 Metal Solubility

The effect of bacterial growth media on metal precipitation was investigated to determine the actual soluble metal content compared to the amount added in the first hour of incubation. This is not commonly done in the testing of bacterial metal toxicity (Nies, 1999; Harrison et al., 2005), but is important for determining lethal amounts of metals. Cultures of stationary *E. coli* were inoculated in LB and MSA media (~10^8 CFU/ml) and incubated for 30 min. Mineral leachates or metal solutions were then reacted with *E. coli* in MSA or LB media at a 1:1 ratio and incubated for 24 h at 37°C. Samples were then transferred into 1.5 ml centrifuge tubes and centrifuged for 30 min. at 13,000 rpm to concentrate any solids. This removes metal precipitates and particles down to ~ 20 nm. Supernatant solutions were separated and diluted with 6M nitric acid (1:2) to prevent metal precipitation before analysis. Metal content was measured using ICP-MS after dilution in 2% nitric acid.

7.2.5 Protein Carbonylation

Oxidation of proteins can occur as reactive oxygen species and metals react with exposed amino acid side chains. Carbonyls (mainly aldehydes) form as a result, which can be quantified, and can be used to determine if the OMT clays are capable of damaging bacterial proteins. *E. coli* overnight cultures (5ml) grown in LB (20g/l) were pelleted by centrifugation at 3,000 rpm for 10 min. Pellets were then resuspended in 2.5 ml MSA media and reacted with 2.5 ml of mineral leachate or metal mixture and incubated at 37°C for 24 h. Samples were pelleted and re-suspended in 5 ml lyse buffer (1mM EDTA, 10mM TRIS Buffer) 3 times and placed on ice. DNase I (enzymatically cleaves DNA) and PMSF (phenylmethane sulfonylfluoride, serine protease inhibitor) (0.1 mM) were added to break apart the nucleoid and lower protein degradation from proteases prior to cell lyses using a French pressure cell. Lysed cells were then centrifuged at 3,000 rpm for 10 min. to remove cell debris. Membrane and soluble protein fractions were separated by ultra-centrifugation under vacuum (40,000rpm, 4°C) for 1h. Nucleic acids were removed from the soluble protein fraction (supernatant) using a nucleic acid removal kit (ProFoldin, NAR911). Soluble proteins were transferred into centrifuge tubes and sodium dodecyl sulfate (SDS) was added to a concentration of 10%. Membrane fractions were resuspended in 10% SDS and placed in a 42°C water bath for 10min. Splits of each protein fraction were reacted with 10mM dinitrophenyl hydrazine (DNPH) in 2.5N HCl (carbonyl content) or 2.5N HCl (control) at room temperature for 30min. Proteins were pelleted using 10% ice cold trichloroacetic acid and centrifuged at 13,000 rpm for 30 min. in a cold room (4°C). Proteins were then re-suspended in ethanol-ethylacetate (1:1) for 30 min. and pelleted (x3) to remove excess DNPH. Protein pellets

were dried and re-suspended in 6M guanidine hydrochloride and absorbance was measured at 370 nm (subtracting control absorbance). Carbonyl content was calculated using the molar extinction coefficient for DNPH (22,000 M^{-1} cm^{-1}). Protein content was determined using the Bradford protein assay kit (Pierce Coomassie Protein Assay™) and calibrated with bovine serum albumin. Results are expressed as nmol-carbonyl/mg protein (nmol carbonyl/mg) (Levine, 1990).

7.2.6 Genetic Stress Responses

Determination of bacterial stress responses to envelope damage and genotoxicity were carried out using *sulA*::*lacZ* (SOS-response) and *rpoHP3*::*lacZ* (σE-response) LacZ fusions, respectively. β-galactosidase activity was measured using 4-methyl-lumbelliferyl β-D-galactopyranoside (MUG) fluorescence (Vidal-Aroca et al., 2006). *E. coli* uses β-galactosidase to cleave the glycosidic bonds present in disaccharides (eg. galactose, lactose). MUG contains a β-D-galactopyranoside moiety linked by a glycosidic bond that can be cleaved by β-galactosidase. This process produces 4-methylumbelliferone (MUB) which fluoresces at 460 nm, thus providing a quantitative measure of enzyme activity and genetic response (Vidal-Aroca et al., 2006). Mineral leachates and metals were reacted in MSA media (1:1 ratio) for 3h (37°C), with 1-10 mg/ml leachate concentrations and 100-1000μM metal concentrations. These concentration ranges approach levels that inhibit growth while still allowing the stress response to be measured. Samples were removed from the incubator and placed on ice for 10min. The MSA media did not result in visible metal precipitation at leachate and metal concentrations less than 10mg/ml and 1000μM, respectively. Cell growth was measured (OD 600 nm) after transferring 200μl of culture

to a 96 well plate. Then 200µl of culture was transferred into 800µl of freshly prepared Z-buffer. Next 250µl of MUG (1 mg/ml) was added and incubated at room temperature for exactly 30 min. at which time 300µl of $NaCO_3$ (1M) was added to stop the reaction. Fluorescence was measured (Cary eclipse fluorescence spectrophotometer) using an excitation wavelength of 360 nm and an emission wavelength of 455nm. β-gal units were calculated using the equation below, which normalizes the MUG fluorescence at 460 nm to incubation time (*t*) and cell density A (OD 600):

β-Gal Units = Fluorescence (460nm) / *t* x A

7.3 Bioimaging

7.3.1 Transmission Electron Microscopy

TEM imaging of bacteria, performed in a time series after mixing cultures with mineral suspensions, provided visual evidence for physical changes to bacterial cellular membranes and internal structures as cells succumb to the clay-mediated antibacterial processes. Mineral suspensions were prepared by mixing bulk blue clay (sample P1, 100 mg/ml) in deionized water, followed by shaking for 24 hrs. Mineral suspensions were allowed to settle for 30 min. to form a dilute mineral suspension. The reason for leaving some minerals in suspension was to look for attraction between minerals and bacterial cells. Bacteria (*E. coli* ATCC 25922 and *S. epidermidis* ATCC 14990) were used for the bioimaging experiments. Cultures (10 ml) of *E. coli* and *S. epidermidis* grown to log-phase (~$5x10^7$ CFU/ml) were pelleted by centrifugation (5000 rpm for 5 min.), re-suspended in isotonic sodium chloride (0.85% NaCl) to remove excess LB-broth and re-

pelleted. The pelleted cells were then exposed to 10 mL of the dilute mineral suspension in and 2 mL aliquots were sampled after 2 hrs, 8 hrs and 24 hrs.

Aliquots of the reacted bacterial mineral suspensions were pelleted and chemically fixed using a 2.5 % glutaraldehyde solution buffered with PBS and stored at 4 °C overnight (Lawrence et al., 2003; Liss et al., 1996). Cells were then pelleted in 0.8 % low-melting point agarose to maintain the cells in dense aggregates. The cell pellets were subsequently fixed for 2 hours using PBS-buffered 1 % osmium tetroxide, block-stained with aqueous 0.5 % uranyl acetate (overnight) and thoroughly washed in de-ionized water three times to remove all salts. The cells were slowly dehydrated using anhydrous acetone. Spurr's low viscosity epoxy resin (Spurr, 1969) was used to infiltrate and embed the cells. The cells were then transferred into silicon molds and polymerized at 70 °C for 8 hours. The resin blocks were sectioned using a Leica Ultracut-R ultramicrotome and a diamond knife. Ultrathin sections were cut to 60 to 70 nm thickness and mounted on Formvar coated TEM grids (Lawrence et al., 2003; Liss et al., 1996). A final staining with 2 % uranyl acetate and Sato's lead citrate (Hanaichi et al., 1986) was performed prior to imaging. TEM images were collected using a Philips CM12 transmission electron microscope operated at 80 kV (Arizona State University, Bio-imaging Facility).

7.3.2 Scanning Transmission Electron Microscopy

Bacteria–mineral suspensions were also imaged using STEM and electron energy loss spectroscopy (EELS) to determine the elemental composition of intracellular precipitates. Aliquots of the bacterial-mineral suspensions were pelleted after reacting for 24 hours at 37 °C. Samples were then fixed using a BalTec HPM010 high-pressure

freezer and freeze substituted using 2 % osmium tetroxide, embedded in Spurr's resin, sectioned (60 nm) and mounted on Cu TEM grids (Spurr, 1969; Walther and Ziegler, 2002). Osmium tetroxide was the only stain used during fixation to avoid additional electron scatter from commonly used lead citrate and uranyl acetate during EELS analysis. STEM images and EELS were collected using a JEOL 2010F TEM/STEM at 200 kV and focused to achieve a resolution of 0.5 eV to image O-K edge and Fe-$L_{2,3}$ and 0.3 eV to determine the redox state of the Fe-$L_{2,3}$ edges (Arizona State University, LeRoy Eyring Center for Solid State Science).

7.3.3 Scanning Transmission X-ray Microscopy

STXM images were measured at the Advanced Light Source (Berkeley, CA) using the 11.0.2 beamline. Data processing was performed using the aXis2000 software package (http://unicorn.mcmaster.ca). Again, a 100mg/ml mineral suspension was shaken for 24h and allowed to flocculate 30 min. forming a dilute mineral suspension. An overnight culture of 2ml *E. coli* grown in LB (20g/l) was pelleted, re-suspended in the dilute mineral suspension (2ml) and incubated (37˚C) on an orbital shaker. Aliquots (0.5 µl) were sampled and pipetted onto a silicon nitride window (Si_3N_4 75nm thick). A second Si_3N_4 window was placed on top of the first window, sealed with epoxy and placed into the STXM sample chamber and purged with helium. Scans of Fe, C, K and Ca were measured using a 1ms dwell time and 0.2eV steps to avoid radiation damage (Warwick et al., 1998). Transmitted signals were converted to optical density by obtaining the incident flux through a portion of the Si_3N_4 cell with no bacteria. Elemental component maps were generated by identifying target spectra using cluster analysis

followed by principal component analysis to identify the spectral features in the image. Reference spectra (Dynes et al., 2006) for $Fe^{2+}Cl_2$ and $Fe^{3+}Cl_3$ were used for quantitative analysis of each target spectra. The energy scale (eV) for Fe^{2+}- and Fe^{3+}-rich target spectra was normalized to the Fe reference compounds (Fe^{2+} at 707.8eV and Fe^{3+} at 709.8eV) (Garvie and Buseck, 1998). Spectral intensities were normalized to the Fe reference spectra and linear regression stack fitting was performed to quantitatively measure the percentages of Fe^{2+} and Fe^{3+} associated with each spectrum (Dynes et al., 2006; aXis2000 software package).

7.3.4 Nano Secondary Ion Mass Spectrometry

E. coli cells, reacted as described above, were sampled after 12h and pelleted by centrifugation. Cells were then fixed in 2.5% glutaraldehyde for 2h, re-pelleted, dehydrated in 50%, 75% and 100% ethanol then dried onto silicon wafers. Isotopic imaging was done using a Cameca (Ametek) NanoSIMS 50L with a 16keV Cs^+ primary ion beam at ~2pA current (~50nm probe size using 300µm D1-2 apertures). This beam was rastered over a 12µm^2 region containing *E. coli* cells with a dwell time of 10msec/pixel (256^2 pixels) for 8 layers (1.5h measurement). Secondary negative ions of $^{12}C^-$, $^{27}Al_2^-$, and $^{56}Fe^-$ were collected simultaneously using electron multiplier detectors. Mass resolution was set to separate isobaric interferences of $^{54}Fe^-$ from $^{27}Al_2^-$ (which makes more negative ions than $^{27}Al^-$) and $^{40}Ca^{16}O^-$ from $^{56}Fe^-$ and was achieved using a 220µm entrance slit.

REFERENCES

Ades SE. (2004). Control of the alternative sigma factor σ^E in *Escherichia Coli*. *Curr. Opin. Microbiol.* **7**:157-162.

Alba BM, Gross CA. (2004). Regulation of the *Escherichia Coli* σ^E dependent envelope stress response . *Mol. Microbiol.* 52:613-619.

Alleva R, Nasole E, Di Donato F, Borghi B, Neuzil J, Tomasetti M. (2005). α-Lipoic acid supplementation inhibits oxidative damage accelerating chronic wound healing in patients undergoing hyperbaric oxygen therapy. *Biochemical and Biophysical Research Communications.* 300:404-410.

Anastácio AS, Harris B, Yoo H, Fabris JD, Stucki JW. (2008). Limitations of the ferrozine method for quantitative assay of mineral systems for ferrous and total iron. *Geochimica et Cosmochimica Acta.* 72:5001-5008.

Andrews SC, Robinson AK, Rodríguez-Quiñones F. (2003). Bacterial iron homeostasis. *FEMS Microbiol. Rev.* 27:215-237.

Aran D, Maul A, Masfaraud J. (2008). A spectrophotometric measurement of soil cation exchange capacity based on cobaltihexamine chloride absorbance. *C.R. Geoscience*. 340:865-871.

Aruoma OI, Halliwell B, Laughton MJ, Quinlan GJ, Gutteridge JMC. (1989). The mechanism of interaction of lipid peroxidation. Evidence against a requirement for an iron(II)-iron(III) complex. *Biochem. J.* 258:617-620.

aXis2000 software written in Interactive Data Language (IDL) is available free for noncommercial use from http://unicorn.mcmaster.ca/aXis2000.html.

Bacon CR and Nathenson M. (1996). Geothermal resources in the Crater Lake area, Oregon. *U.S. Geological Survey Open-File Report* 96–663.

Bacon CR. (2008). Geologic map of Mount Mazama and Crater Lake caldera, Oregon. *U.S. Geological Survey Scientific Investigations Map*, 2832:1-47.

Baedecker PA. (1987). Methods for geochemical analysis. *U.S. Geological Survey Bulletin* 1770.

Baertschi P. (1976). Absolute ^{18}O content of standard mean ocean water. *Earth and Planetary Science Letters*. 31:341-344.

Bargar KE, Keith TE. (1999). Hydrothermal mineralogy of core from geothermal drill holes at Newberry volcano, Oregon. *U.S. Geological Survey Professional Paper*. 1578.

Barnes HL. (1997). *Geochemistry of hydrothermal ore deposits*. John Wiley & Sons, Inc. New York.

Bauer AW, Kirby WMM, Sherris JC, Turck M. (1966). Antibiotic susceptibility testing by a standardized single disk method. *Amer. J. Clin. Pathol*. 45: 493-496.

Beaty DW, Hugh PT. (1988). An oxygen isotope study of the Kidd Creek, Ontario, volcanogenic massive sulfide deposit: evidence for a high ^{18}O ore fluid. *Economic Geology*. 83:1-17.

Beveridge TJ, Koval F. (1981). Binding of metals to cell envelopes of *Escherichia coli* K-12. *Appl. Environ. Microbiol*.42:325-335.

Bhowal S, Chakraborty R. (2011). Five novel acid-tolerant oligotrophic thiosulfate-metabolizing chemolithotrophic acid mine drainage strains affiliated with the genus *Burkholderia* of *Betaproteobacteria* and identification of two novel soxB gene homologues. *Research in Microbiology*. 162:436-445.

Bindeman H. (2008). Oxygen isotopes in mantle and crustal magmas as revealed by single crystal analysis. *Reviews in Mineralogy & Geochemistry*. 69:445-478.

Bons PD. (2001). The formation of large quartz veins by rapid ascent of fluids in mobile hydrofractures. *Tectonophysics.* 336:1-17.

Borrok D, Fein JB, Tischler M, O'Loughlin E, Meyer H, Liss M, Kemner KM. (2004). The Effect of Acidic Solutions and Growth Conditions on the Adsorptive Properties of Bacterial Surfaces. *Chemical Geology*. 209**:**107–119.

Brunet de Courrsou L. (2002). Study Group Report on Buruli Ulcer Treatment with Clay, 5th WHO Advisory Group Meeting on Buruli Ulcer, Geneva, Switzerland.

Bullen JJ, Rogers HJ, Spalding PB, Ward CG. (2006). Natural resistance, iron and infection: a challenge for clinical medicine. *Journal of Medical Microbiology*. 55:251-258.

Carretaro MI. (2002). Clay minerals and their beneficial effects upon human health: A review. *Applied Clay Science*. 21:155-163.

Cabiscol E, Tamarit J, Ros J. (2000). Oxidative stress in bacteria and protein damage by reactive oxygen species. *Internatl Microbiol*. 3:3-8.

Cadet J, Delatour T, Douki T, Gasparutto D, Pouget JP, Ravanat JL, Sauvaigo S. (1999). Hydroxyl radicals and DNA base damage. *Mutation Research*. 424:9-21.

Church CD, Wilkin RT, Alpers CN, Rye RO, McCleskey RB. (2007). Microbial sulfate reduction and metal attenuation in pH 4 acidic mine water. *Geochemical Transictions*, 8:1-14.

Cohn CA, Pak A, Strongin D, Schoonen MAA. (2005). Quantifying hydrogen peroxide in iron containing solutions using leuco crystal violet. *Geochem. Trans.* 6:47-51.

Cohn CA, Laffers R, Simon SR, O'Riordan T, Schoonen MAA. (2006). Role of pyrite in formation of hydroxyl radicals in coal: possible implications for human health. *Particle and Fibre Toxic*. 3:article 16.

Craig H. (1961). Isotopic variations in meteoric waters. *Science*. 133:1702-1703.

Cunningham TB, Koehl JL, Summers JS, Haydel SE. (2010). pH-dependent metal ion toxicity influences the antibacterial activity of two natural mineral mixtures. *PLoS-ONE*. 5:e9456.

Delmelle P, Bernard A, Kusakabe M, Fischer TP, Takano B. (2000). Geochemistry of the magmatic-hydrothermal system of Kawah Ijen volcano, East Java, Indonesia. *Journal of Volcanology and Goethermal Research*. 97:31-53.

Derkowski A, Bristow TF. (2012). On the problems of total specific surface area and cation exchange capacity measurements in organic-rich sedimentary rocks. *Clays and Clay Minerals*. 60:348-362.

Dold B. (2005). Basic concepts in environmental geochemistry of sulfide mine-waste, Del 22 de Agosto al 2 de Sept. XXIV Curso Latinoamericano de Metalogenia UNESCO-SEG.

Dynes JJ, Tyliszczak T, Araki T, Lawrence JR, Swerhone GD, Leppard GG, Hitchcock AP. (2006). Speciation and quantitative mapping of metal species in microbial biofilms using scanning transmission X-ray microscopy. *Environ. Sci. Technol.* 40:1556-1565.

Eberl DD. (1978). Reaction series for dioctahedral smectites. *Clays and Clay Minerals*. 26:327-340.

Eberl DD. (2009). User's guide to rockjock: A program for determining quantitative mineralogy from powder X-ray diffraction data. *U.S. Geological Survey*, Open-file report 03-78.

Evangelou VP. (1995). *Pyrite Oxidation and its Control*. New York, CRC Press.

Exley C. (2004) The pro-oxidant activity of aluminum. *Free Radical Bio. Med.* 36:380-387.

Fang FC. (2004). Antimicrobial reactive oxygen and nitrogen species: concepts and controversies. *Nature Reviews:Microbiology.* 2:820-832.

Faure G. (1998). *Principles and applications of geochemistry 2nd edition*. Prentice-Hall, Inc. New Jersey.

Fein JB, Daughney CJ, Yee N, Davis TA. (1997). A chemical equilibrium model for metal adsorption onto bacterial surfaces. *Geochim. Cosmochim. Acta.* 61:3319-3328.

Ferrell RE. (2008). Medicinal clay and spiritual healing. *Clays and Clay Minerals*. 56:751-760.

Ferrero T. (1992). Geologic mapping and sampling project, Foster Creek sulfur deposit. Company Report, Ferrero Geologic, 340 Avery St. Ashland Oregon, 97520.

Fiebelkorn RB, Walker GW, Macleod NS, McKee EH, Smith JG. (1983). Index to K-Ar age determinations for the state of Oregon. *Isochron/West*. 37:3-60

Galan E, Carretero MI, Fernandez-Caliani JC. (1999). Effects of acid mine drainage on clay minerals suspended in the Tinto River (Río Tinto, Spain): An experimental approach. *Clay Minerals*. 34:99-108.

Garrels RM, Thompson ME. (1960). Oxidation of pyrite by iron sulfate solutions. *Amer. Jour. Sci.* 258-A:57-67.

Garvie LAJ, Buseck PR. (1998). Ratios of ferrous to ferric iron from nanometer-sized areas in minerals. *Nature*. 396:667-670.

Gethin GT. (2007). The significance of surface pH in chronic wounds. *Wounds UK*. 3: 52-56.

Gethin GT, Cowman S, Conroy RM. (2008). The impact of Manuka honey dressings on the surface pH of chronic wounds. *International Wound Journal*. 5:185-194.

Goodfellow WD. (2007). Mineral deposits of Canada—A synthesis of major deposit-types, district metallogeny, the evolution of geological provinces, and exploration methods. *Geological Association of Canada, Mineral Deposits Division, Special Publication No. 5.*

Götz F. (2002). *Staphylococcus* and biofilms. *Molecular Microbiology.* 43:1367-1378.

Gutteridge JMC. (1995). Lipid peroxidation and antioxidants as biomarkers of tissue damage. *Clin. Chem*. 41:1819-1828.

Halliwell B, Chirico S. (1993). Lipid peroxidation: its mechanism, measurement, and significance. *Am. J. Clin. Nutr*. 57:715s-725s.

Hammond PE. (1979). A tectonic model for evolution of the Cascade range. Pacific Coast Paleogeography Symposium 3: Cenozoic Paleogeography of the Western United States.

Harrison JJ, Turner RJ, Ceri H. (2005). High-throughput metal susceptibility testing of microbial biofilms. *BMC Microbiol* .5:1471-2180.

Hanaichi T, Sato T, Iwamoto T, Malavasi-Yamashiro J, Hoshing M, Mizuno N. (1986). A Stable Lead by Modification of Sato's Method. *Journal of Electron Microscopy*, 35, 304-306.

Hedenquist JW, Lowenstern JB. (1994). The role of magmas in the formation of hydrothermal ore deposits. *Nature*. 370:519-527.

Hedges AJ. (2002). Estimating the precision of serial dilutions and viable bacterail counts. *International Journal of Food Microbiology*. 76:207-214.

Hervig RL, Williams P, Thomas RM, Schauer SN, Stelle IM. (1992). Microanalysis of oxygen isotopes in insulators by secondary ion mass spectrometry. *International Journal of Mass Spectrometry and Ion Processes*. 120:5-63.

Hervig RL, Williams LB, Kirkland IK, Longstaffe FJ. (1995). Oxygen isotope microanalysis of diagenetic quartz: possible low temperature occlusions of pores. *Geochimica et Cosmochimica Acta*. 59:2537-2543.

Hervig RL, Mazdab FK, Williams P, Guan Y, Huss GR, Leshin LA. (2006). Useful ion yields for Cameca IMS 3f and 6f SIMS: limits on quantitative analysis. *Chemical Geology*. 227:83-99.

Huisman O, D'Ari D, Gottesman S. (1984). Cell-division control in *Escherichia coli*: specific induction of the SOS function SfiA protein is sufficient to block septation. *Proc. Natl. Acad. Sci.* 81:4490-4494.

Hutchinson IPG, Ellison RD. (1992). *Mine Waste Management*. Lewis publishers, Inc. 121 S. Main St. Chelsea, Michigan.

Imlay JA, Chin SM, Linn S. (2008). Toxic DNA damage by hydrogen peroxide through the Fenton reaction in vivo and in vitro. *Science*. 240:640-642.

Kaufman T, Eichenlaub EH, Angel MF, Levin M, Futrell JW. (1985). Topical acidification promotes healing of experimental deep partial thickness skin burns: a randomized double-blind preliminary study. *Burns*. 12:84-90.

Keith TC, Bargar KE. (1988). Petrology and hydrothermal mineralogy of the U.S. Geological Survey Newberry 2 drill core from Newberry caldera, Oregon. *Journal of Geophysical Research*. 93:10174-10190.

Kohn MJ, Miselis JL, Fremd TJ. (2002). Oxygen isotope evidence for progressive uplift of the Cascade Range, Oregon. *Earth and Planetary Science Letters*. 204:151-165.

Komadel P, Stucki JW. (1988). Quantitative assay of minerals for Fe^{2+} and Fe^{3+} using 1,10-phenanthroline: III. A rapid photochemical method. *Clays and Clay Minerals.* 36:379-381.

Kostka JE, Dalton DD, Skelton H, Sherry D, Stucki JW. (2002). Growth of iron(III)-reducing bacteria on clay minerals as the sole electron acceptor and comparison of growth yields on a variety of oxidized iron forms. *Appl. Environ. Microbio.* 68:6256-6262.

Lambers H, Piessens S, Bloem A, Pronk H, Finkel P. (2006). Natural skin surface pH is on average below 5, which is beneficial for its resident flora. *International Journal of Cosmetic Science*. 28:359-370.

Lawrence JR, Swerhone GDW, Leppard GG, Araki T, Zhang X, West MM, Hitchcock AP. (2003). Scanning transmission X-ray, laser scanning, and transmission electron microscopy mapping of the exopolymeric matrix of microbial biofilms. *Appl. Environ. Microbiol*. 69:5543-5554.

Lemire JA, Mailloux R, Auger C, Whalen D, Appanna VD. (2010). *Pseudomonas fluorescens* orchestrates a fine metabolic-balancing act to counter aluminum toxicity. *Env. Microbiol.* 12:1384-1390.

Lemire JA, Harrison JJ, Turner RJ. (2013). Antimicrobial activity of metals: mechanisms, molecular targets and applications. *Nature Reviews.*11:371-384.

Leveen HH, Falk G, Borek B, Diaz C, Lynfield Y, Wynkoop BJ, Mabunda GA, Rubricius JL, Christoudias GC. (1973.) Chemical acidification of wounds: An adjuvant to healing and the unfavorable action of alkalinity and ammonia. *Ann. Surg.* 178:745-753.

Levine RL, Garland D, Oliver CN, Amici A, Climent I, Lenz A, Ahn B, Shaltiel S, Stadtman ER. (1990). Determination of carbonyl content in oxidatively modified proteins. *Method Enzymol.* 186:464-478.

Liss SN, Droppo IG, Flannigan DT, Leppard GG. (1996). Floc architecture in wastewater and natural riverine systems. *Environ. Sci. Technol*. 30:680-686.

Liu Y, Kalen A, Risto O, Whalstrom O. (2002). Fibroblast proliferation due to exposure to a platelet concentrate in vitro is pH dependent. *Wound Repair and Regeneration*. 10:336-340.

Matthews A. Beckinsale RD. (1979). Oxygen isotop equilibrium systematics between quartz and water. *American Mineralogist.* 64: 232-240.

McCarty DK, Sakharov BA, Drits VA. (2008). Early clay diagenesis in Gulf Coast sediments: New insights from XRD profile modeling. *Clays and Clay Minerals*. 56:359–379.

Meunier A. (2005). *Clays.* Springer Berlin Heidelberg, New York.

Miles AA, Misra SS. (1938). The estimation of the bactericidal power of the blood. *The Journal of Hygiene*. 38: 732-749.

Moore DM, Reynolds RC. (1997). *X-ray diffraction and the identification and analysis of clay minerals 2nd edition*. Oxford University Press, New York.

Morgan B, Lahav O. (2007). The effect of pH on the kinetics of spontaneous Fe(II) oxidation by O_2 in aqueous solution – basic principles and a simple heuristic description. *Chemosphere*. 68:2080-2084.

Morrison KD, Underwood JC, Metge DW, Eberl DD, Williams LB. (2014). Mineralogical variables that control the antibacterial effectiveness of a natural clay deposit. *Environ. Geochem. Health.* 36:613-631.

Moses CO, Herman JS. (1991). Pyrite oxidation at circumneutral pH. *Geochimica et cosmochimica acta.* 55:471-482.

Mullen M D, Wolf DC, Ferris F, Beveridge TJ, Flemming CA, Bailey GW. (1989). Bacterial sorption of heavy metals. *Applied Environmental Microbiology*. 55:3143-3149.

Murad E, Rojik P. (2003). Iron-rich precipitates in a mine drainage environment: influence of pH on mineralogy. *American Mineralogist*. 88:1915-1918.

Murad E, Rojik P. (2005). Iron mineralogy of mine drainage precipitates as environmental indicators: review of the current concepts and a case study from the Sokolov Basin, Czech Republic. *Clay Minerals*. 40:427-440.

Musk DJ, Banko DA, Hergenrother PJ. (2005). Iron salts perturb biofilm formation and disrupt existing biofilms of *Pseudomonas aeruginosa*. *Chemistry & Biology*. 12:789-796.

Naumov VB, Dorofeeva VA, Mironova OF, Prokof'ev VY. (2015). Sources of high-pressure fluids involved in the formation of hydrothermal deposits. *Geochemistry International*. 50:590-606.

Newman DJ, Cragg GM. (2007). Natural products as sources of new drugs over the last 25 years. *J. Natural Products*. 70:461-77.

Nies DH. (1999). Microbial heavy-metal resistance. *Appl. Microbiol. Biotechnol*. 51:730-750.

Nies DH. (2003). Efflux-mediated heavy metal resistance in prokaryotes. *FEMS Microbiology Reviews*. 27:313-339.

Nordstrom K. (1977). Thermochemical redox equilibria of ZoBell's solution. *Geochimica et Cosmochimica Acta*. 41:1835-1841.

Pearson RG. (1966). Acids and bases. *Science.* 151:172-177.

Pirajno F. (2009). *Hydrothermal processes and mineral systems*. Springer, Berlin. 1-1250.

Power SG, Field CW, Armstrong RL, Harakal JE. (1981). K-Ar ages of plutonism and mineralization, western Cascades, Oregon and southern Washington. *Isochron/West*. 31:27-29.

Priest GR. (1990). Volcanic and tectonic evolution of the Cascade volcanic arc, central Oregon. *Journal of Geophysical Research*. 95: 19583-19599.

Puigdomenech I. (2004). Hydra/Medusa Chemical Equilibrium Database and Plotting Software. Stockholm: KTH – Royal Institute of Technology.

Raivio TL. (2005). Envelope stress responses and Gram-negative bacterial pathogenesis. *Mol. Microbiol.* 56:1119-1128.

Ratledge C, Dover LG. (2000). Iron metabolism in pathogenic bacteria. *Annu. Rev. Microbiol*. 54:881-941.

Reyes AG. (1990). Petrology of Philippine geothermal systems and the application of alteration mineralogy to their assessment. *Journal of Vocanology and Geothermal Research*. 43:279-309.

Reynolds RC. (1980). Interstratified clay minerals: in Brindley, GW and Brown, G. *Crystal Structures of Clay Minerals and Their X-ray Identification*: Monograph No. 5, Mineralogical Society London. 249-303.

Rimstidt JD, Vaughan DJ. (2003). Pyrite oxidation: a state of the art assessment of the reaction mechanism. *Geochimica et cosmochimica act.* 67:873-880.

Roth RN, Weiss LD. (1994). Hyperbaric oxygen and wound healing. *Clinics in Dermatology*. 12:141-156.

Roy S, Khanna S, Nallu K, Hunt TK, Sen CK. (2006). Dermal wound healing is subject to redox control. *Mol Ther*. 1:211-220.

Schneider LA, Korber A, Grabbe S, Dissemond J. (2007). Influence of pH on wound-healing: a new perspective for wound therapy? *Arch. Dermatol. Res*. 298:413-420.

Schoonen MAA, Harrington AD, Laffers R, Strongin DR. (2010). Role of hydrogen peroxide and hydroxyl radical in pyrite oxidation by molecular oxygen. *Geochimica et Cosmochimica Acta*. 74:4971-4987.

Seedorff E, Dilles JH, Proffett JM, Einaudi MT. Porphyry deposits: Characteristics and orgin of hypogene features. *Economic Geology 100th Anniversary Volume*:251-298.

Shaw SA, Hendry MJ. (2009). Geochemical and mineralogical impacts of H_2SO_4 on clays between pH 5.0 and 3.0. *Applied Geochemistry*. 24:333-345.

Sherrod DR, Smith JG. (2000). Geologic map of upper eocene to holocene volcanic and related rocks of the cascade range, Oregon. *U.S. Geological Survey Scientific Investigations Map* I-2569.

Silhavy TJ, Kahne D, Walker S. (2010). The bacterial cell envelope. *Cold Spring Harbor Perspectives in Biology.* doi:10.1101/cshperspect.a000414.

Singer DA, Berger VI, Moring BC. (2005). Porphyry copper deposits of the world: Database, map, and grade and tonnage models. *U.S. Geological Survey Open-File Report* 2005-1060.

Singer PC, Stumm W. (1970). Acid mine drainage the rate determining step. *Univ of Toronto Stud. Geol. Sur*. 44:83-93.

Smith JL. (2004). The physiological role of ferritin like compounds in bacteria. *Clinical Reviews in Microbiology*. 30:173-185.

Spurr AR. (1969). A low-viscosity epoxy resin embedding medium for electron microscopy. *Journal of Ulrastructural Research*. 26:31-43.

Środoń J. (1980). Precise identification of illite/smectite interastratifications by X-ray powder diffraction. *Clays and Clay Minerals*. 28:401-411.

Stumm W, Morgan JJ. (1996). *Aquatic Chemistry*: *Chemical equiilibria and rate constants in natural waters, 3rd edition*. John Wiley & Sons, Incorporated, New York.

Susse C, Epain R, Vodar B. (1966). Determination de la courbe de fusion de soufre sous pression jusqu' a 90 kbars. *Journal de Chimie Phisique*. 11-12:1502-1506.

Tang L, Zhang Y, Qian Z, Shen X. (2000). The mechanism of Fe^{2+}-initiated lipid peroxidation in liposomes: the dual function of ferrous ions, the roles of the pre-existing lipid peroxides and the lipid peroxyl radical. *Biochemical Society Journal*. 352:27-36.

Tanner D, Henley RW, Mavrogenes JA, Holden P, Mernagh TP. (2015). Silica hydrate preserved with $\delta^{18}O$-rich quartz in high-temperature hydrothermal quartz in the high sulfidation copper-gold deposit at El Indio, Chile. *Chemical Geology*. 391:90-99.

Taylor BE, Huston DL. (1998). Hydrothermal alteration of oxygen isotope ratios in quartz phenocrysts, Kidd Creek mine, Ontario: magmatic values preserved in zircons, comment. *Geology*. 26:763-764.

Taylor JE, Laity PR, Hicks J, Wong SS, Norris K, Khunkamchoo P, Johnson AF, Cameron RE. (2005). Extent of iron pick-up in deforoxamine-coupled polyurethane materials for therapy of chronic wounds. *Biomaterials*. 26:6024-6033.

Teitzel GM, Parsek MR. (2003). Heavy metal resistance of biofilm and planktonic *Pseudomonas aeruginosa*. *Appl. Environ. Microbiol.* 69:2313-2320.

Totsche O, Fyson A, Kalin M, Steinberg CEW. (2006). Titration curves-A useful instrument for assessing the buffer systems of acidic mining waters. *Environ Sci Pollut Res*. 13:215-224.

Tovar-SanchezA, Saundo-Wilhelmy SA, Garcia-Vargas M, Weaver RS, Popels LC, Hutchins DA. (2003). A trace metal clean reagent to remove surface bound iron from marine phytoplankton. *Mar. Chem*. 82:91-99.

Urrutia MM and Beveridge TJ. (1995) Formation of short-range ordered aluminosilicates in the presence of a bacterial surface (Bacillus subtilis) and organic ligands. *Geoderma.* 65:149-165.

Utada M. (1980). Hydrothermal alteration related to igneous acidity in Cretaceous and Neogene formations of Japan. *Mining Geology Japan Special Issue*. 8:67-83.

Valverde A, Delvasto P, Peix A, Velazquez E, Santa-Regina I, Ballester A, Rodriguez-Barrueco C, Garcia-Balboa C, Igual JM. (2006). Burkholderia ferrariae sp. Nov., isolated from an iron ore in Brazil. *International Journal of Systematic and Evolutionary Microbiology*. 56:2421-2425.

Velde B. (1995). *Orgin and Mineralogy of Clays*. Springer Berlin Heidelberg, New York.

Vidal-Aroca F, Giannattasio ME, Brunelli E, Vezzoli A, Plevani P, Muzi-Falconi M, Bertoni G. (2006). One-step high-throughput assay for quantitative detection of β-galactosidase activity in intact gram-negative bacteria, yeast, and mammalian cells. *Bio. Tech*. 40:433-440.

Walker GW, Macleod NS. (1991). Geologic map of Oregon. U.S. Geological Survey. 2 plates, scale 1:500,000.

Walther P, Ziegler A. (2002). Freeze substitution of high-pressure frozen samples: the visibility of biological membranes is improved when the substitution medium contains water. *Journal of Microscopy*. 209:3-10.

Walsh C. (2000). Molecular mechanisms that confer antibacterial drug resistance. *Nature.* 406:775-781.

Warwick T, Franck K, Kortright JB, Meigs G, Moronne M, Myneni S, Rotenberg E, Seal S, Steele WF, Ade H, Garcia A, Cerasari S, Denlinger J, Hayakawa S, Hitchcock AP, Tyliszczak T, Kikuma J, Rightor EG, Shin HJ, Tonner BP. (1998). A scanning transmission X-ray microscope for materials science spectro-microscopy at the Advanced Light Source. *Rev. Sci. Instrum*. 69:2964-2973.

Weller R, Price RJ, Ormerod AD, Benjamin N, Leifert C. (2001). Antimicrobial effect of acidified nitrite on dermatophyte fungi. *Candida* and bacterial skin pathogens. *Journal of Applied Microbiology*. 90:648-652.

Weller R, Finnen MJ. (2006). The effects of topical treatment with acidified nitrite on wound healing in normal and diabetic mice. *Nitric Oxide*: 15:395-399.

Williams LB, Holland M, Eberl DD, Brunet T, Brunet de Courrsou L. (2004). Killer clays! Natural antibacterial clay minerals. *Min. Soc. Bull*. 139:3-8.

Williams LB, Haydel SE, Giese RF, Eberl DD. (2008). Chemical and mineralogical characteristics of French green clays used for healing. *Clays and Clay Mins*. 56:437-452.

Williams LB, Haydel SE. (2010). Evaluation of the medicinal use of clay minerals as antibacterial agents. *International Geology Review*. 52:745-770.

Williams LB, Metge DW, Eberl DD, Harvey RW, Turner AG, Prapaipong P, Poret-Peterson A. (2011). What Makes a Natural Clay Antibacterial? *Environ. Sci. Technol*. 45:3768-3773.

Williams RJP. (1999). What is wrong with aluminium? The J.D. Birchall memorial lecture. *Journal of Inorganic Biochemistry*. 76:81-88.

Wilson E, Henry DA, Smith JA. (1990). Disk elution method for MICs and MBCs. *Antimicrobial Agents and Chemotherapy*. 34:2128-2132.

Winterbourn CC. (2008). Reconciling the chemistry and biology of reactive oxygen species. *Nature Chem. Biol.* 4:278-286.

Yariv S. (1992). The effect of tetrahedral substitution of Si by Al on the surface acidity of the oxygen plane of clay minerals. *Int. Rev. Phys. Chem*. 11:345-375.

Yariv S, Cross H. (2002). *Organo-Clay Complexes and Interactions*. New York, Marcel Dekker, Inc. 1-38.

APPENDIX A

QUANTITATIVE XRD FITS

RockJock11 quantitative XRD pattern fits from representative zones in the OMT deposit are shown below, with calculated patterns (red) shown in front of the measured XRD pattern (blue) (Eberl, 2009). The light grey line shows the residual error of the fit (see Tables 3.3-3.6 for sample identifications).

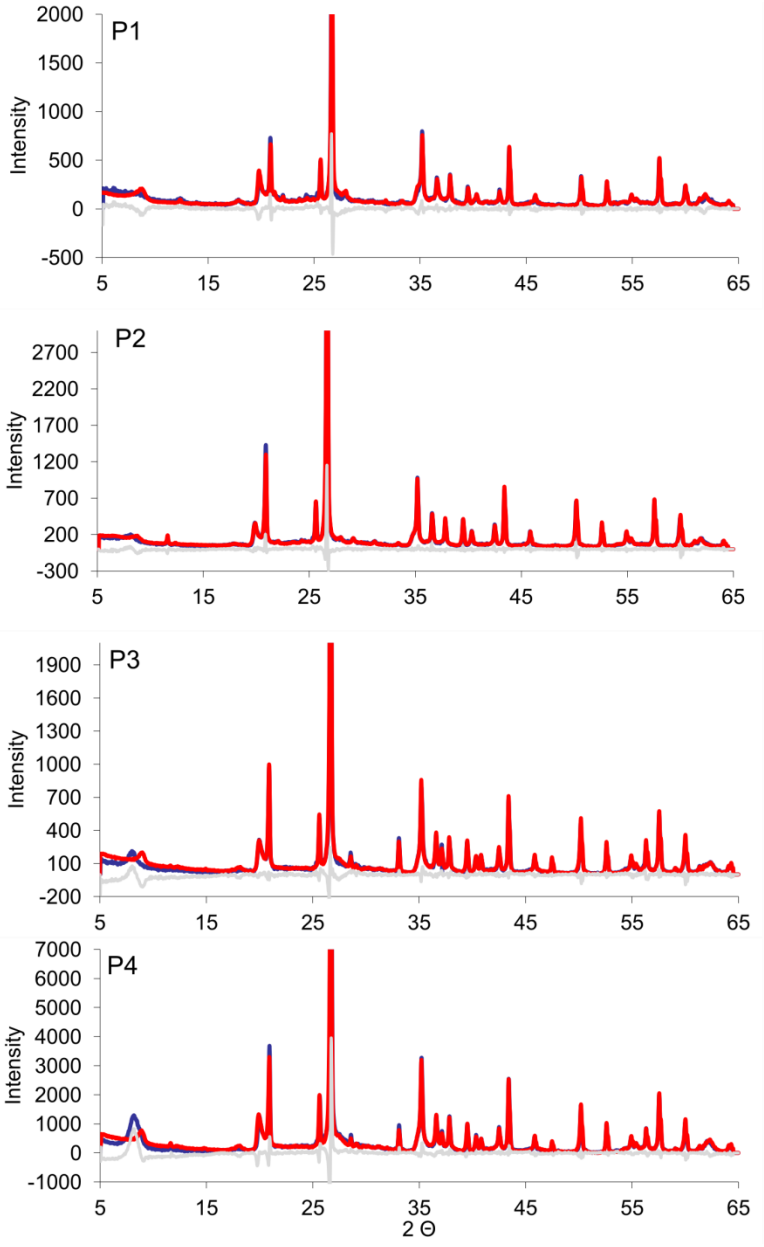

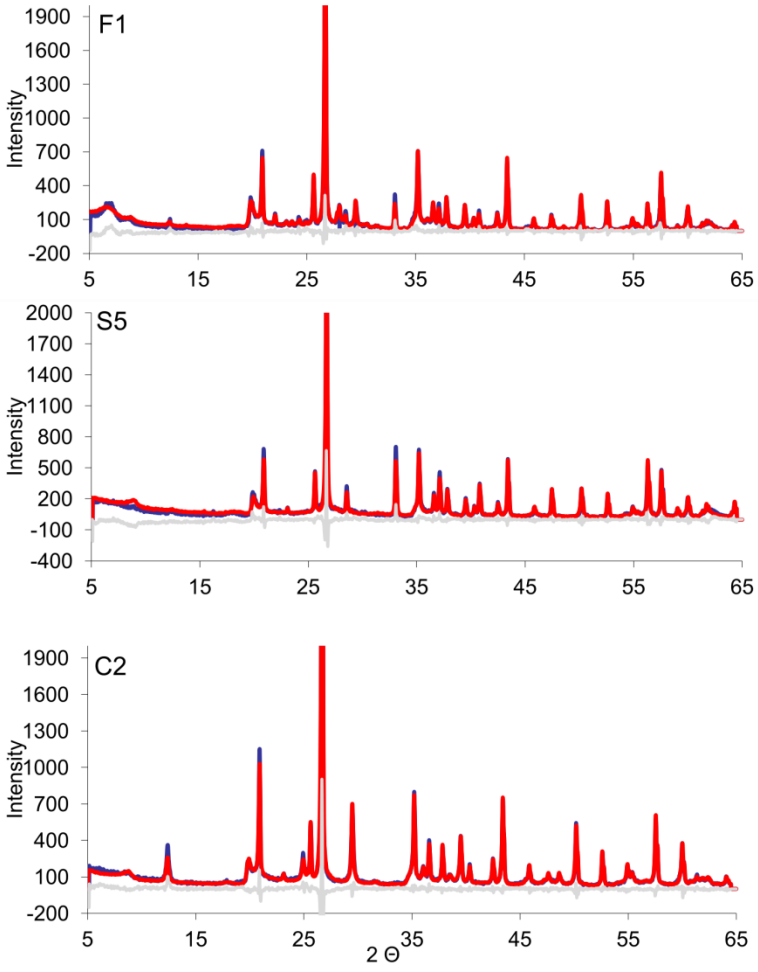
F1
Intensity
1900
1600
1300
1000
700
400
100
-200
5
15
25
35
45
55
65
S5
Intensity
2000
1700
1400
1100
800
500
200
-100
-400
C2
Intensity
2 Θ

APPENDIX B

QUARTZ TEMPERATURE CALCULATIONS

Quartz formation temperatures were calculated using the quartz-water $\delta^{18}O$ equilibrium fractionation equation (Matthews and Beckinsale, 1979) (equation 1). Theoretical $\delta^{18}O_{water}$ values were used for the calculations based on mineralogical constraints described in section 3.3.7.

$$10^3 \ln (\delta^{18}O_{quartz} - \delta^{18}O_{water}) = 3.05 \times 10^6 T^{-2} - 2.09 \qquad (1)$$

Table B1. Quartz $\delta^{18}O$ data. SIMS $\delta^{18}O$ analysis of quartz crystals form the Sulfur Mine black clay (S4), Open Pit blue (P4) and white (P2) clay zones. The number of analyses and standard error for each measurement are reported. Lower limit temperatures of formation were calculated from the average quartz $\delta^{18}O$values using theoretical water compositions. (see section 3.3.7. for details).

Sulfur Mine Black	$\delta^{18}O$ ‰	Standard Error
1	24.6	1.4
2	21.2	1.4
3	21.1	1.7
4	23.4	1.6
5	22.1	1.5
6	22.8	1.7
7	25.2	1.6
Average	22.9	
Standard Deviation	1.6	
Temperature ($\delta^{18}O_{water}$ +10‰)	178°C	
Open Pit Blue		
1	15.7	1.6
2	14.2	1.4
3	15.8	1.4
4	12.5	1.0
5	12.5	1.4
6	16.1	1.1
7	16.4	1.2
Average	14.7	
Standard Deviation	1.7	
Temperature ($\delta^{18}O_{water}$ 0 ‰)	153°C	
Open Pit White		
1	6.8	1.5
2	4.3	1.4
3	4.3	1.5
4	4.0	1.7
Average	4.9	
Standard Deviation	1.3	
Temperature ($\delta^{18}O_{water}$ -15 ‰)	99°C	

APPENDIX C

ANTIBIOTIC RESISTANT STRAINS

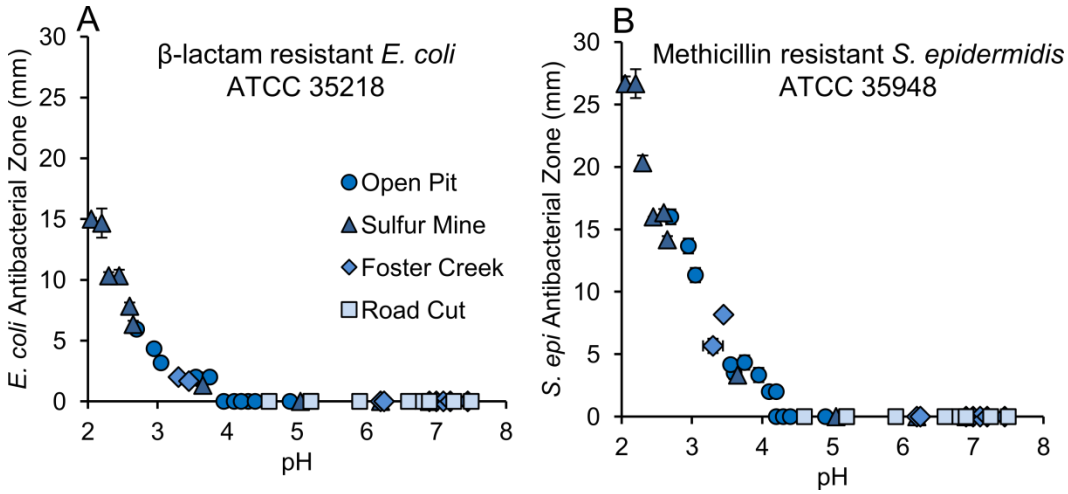

Antibiotic resistant strains. Antibacterial zone of inhibition testing of (A) Beta-lactam resistant *E. coli* and (B) Methicillin resistant *S.epidermidis*.

APPENDIX D

ZONE OF INHIBITION TESTING

Table D1. Antibacterial zone of inhibition testing of clay zones from the Open Pit (P) and Sulfur Mine (S) sampling sites. The diameter (mm) of the growth inhibition zone was measured to quantify the antibacterial activity of each sample.

	Escherichia coli Zone of Inhibition (mm)				*Staphylococcus epidermidis* Zone of Inhibition (mm)			
Sample	ATCC 25922	Std. Dev.	ATCC 35218	Std. Dev.	ATCC 14990	Std. Dev.	ATCC 35948	Std. Dev.
P1	0.0	---	0.0	---	0.0	---	0.0	---
P2	0.0	---	0.0	---	0.0	---	0.0	---
P3	**8.0**	**0.0**	**5.9**	**0.1**	**16.0**	**0.6**	**12.7**	**0.6**
P4	**8.2**	**0.3**	**4.3**	**0.3**	**13.7**	**0.6**	**13.0**	**0.0**
P5	**6.0**	**0.0**	**3.2**	**0.3**	**11.3**	**0.6**	**8.8**	**0.3**
P6	**2.7**	**0.6**	**1.8**	**0.3**	**3.5**	**0.5**	**2.3**	**0.6**
P7	**2.0**	**0.0**	**2.0**	**0.0**	**4.2**	**0.4**	**2.7**	**0.6**
P8	**2.3**	**0.6**	**2.0**	**0.0**	**4.3**	**0.6**	**3.3**	**0.6**
P9	**2.0**	**0.0**	**0.0**	**0.0**	**3.3**	**0.6**	**2.3**	**0.6**
P10	0.0	---	0.0	---	**2.0**	**0.0**	**1.0**	**0.0**
P11	0.0	---	0.0	---	0.0	---	0.0	---
P12	0.0	---	0.0	---	**2.0**	**0.0**	**2.3**	**0.6**
P13	0.0	---	0.0	---	0.0	---	0.0	---
P14	0.0	---	0.0	---	0.0	---	0.0	---
P15	0.0	---	0.0	---	0.0	---	0.0	---
S1	0.0	---	0.0	---	0.0	---	0.0	---
S2	**2.0**	**0.0**	**1.3**	**0.6**	**3.3**	**0.6**	**2.3**	**0.6**
S3	**12.5**	**0.5**	**10.3**	**0.3**	**16.0**	**0.0**	**13.7**	**0.6**
S4	**17.1**	**0.1**	**15.0**	**0.0**	**26.7**	**0.6**	**21.3**	**1.2**
S5	**12.2**	**0.3**	**10.3**	**0.6**	**20.3**	**0.6**	**18.0**	**0.0**
S6	**8.3**	**0.3**	**6.3**	**0.6**	**14.2**	**0.3**	**13.3**	**0.6**
S7	**17.0**	**1.2**	**14.7**	**0.3**	**26.7**	**1.2**	**23.7**	**0.6**
S8	**10.2**	**0.3**	**7.8**	**0.3**	**16.3**	**0.3**	**14.7**	**0.6**
S9	0.0	---	0.0	0.0	0.0	---	0.0	---
S10	0.0	---	0.0	0.0	0.0	---	0.0	---

Table D2. Antibacterial zone of inhibition testing of clay zones from the Foster Creek (F) and Road Cut (C) sampling sites. The diameter (mm) of the growth inhibition zone was measured to quantify the antibacterial activity of each sample.

	Escherichia coli				*Staphylococcus epidermidis*			
	Zone of Inhibition (mm)				Zone of Inhibition (mm)			
Sample	ATCC 25922	Std. Dev.	ATCC 35218	Std. Dev.	ATCC 14990	Std. Dev.	ATCC 35948	Std. Dev.
F1	0.0	---	0.0	---	0.0	---	0.0	---
F2	0.0	---	0.0	---	0.0	---	0.0	---
F3	0.0	---	0.0	---	0.0	---	0.0	---
F4	0.0	---	0.0	---	0.0	---	0.0	---
F5	0.0	---	0.0	---	0.0	---	0.0	---
F6	0.0	---	0.0	---	0.0	---	0.0	---
F7	0.0	---	0.0	---	0.0	---	0.0	---
F8	**2.7**	**0.1**	**2.0**	**0.0**	**5.7**	**0.6**	**5.0**	**0.0**
F9	**2.7**	**0.3**	**1.7**	**0.6**	**8.2**	**0.3**	**6.3**	**0.6**
C1	0.0	---	0.0	---	0.0	---	0.0	---
C2	0.0	---	0.0	---	0.0	---	0.0	---
C3	0.0	---	0.0	---	0.0	---	0.0	---
C4	0.0	---	0.0	---	0.0	---	0.0	---
C5	0.0	---	0.0	---	0.0	---	0.0	---
C6	0.0	---	0.0	---	0.0	---	0.0	---
C7	0.0	---	0.0	---	0.0	---	0.0	---
C8	0.0	---	0.0	---	0.0	---	0.0	---
C 9	0.0	---	0.0	---	0.0	---	0.0	---

APPENDIX E

ICP-MS AND FERROUS IRON

Table E1. ICP-MS elemental analysis of mineral leachates (100 mg/ml) from the Open Pit mine and pH, Eh and H_2O_2 measurements from 100 mg/ml mineral suspensions. All element values are reported at micro-molar (µM) concentrations. Elements < 1nM are listed as below detection limit (BDL). The standard deviation for ICP-MS analysis was < 7.0 %. Ferrous iron concentrations were measured using 1, 10 phenanthroline, with standard deviation values for Fe^{2+} are reported as S.D. (Fe^{2+}).

Element	P1	P2	P3	P4	P5	P6	P7
Na	43.4	39.1	159.1	34.2	13.7	214.0	310.9
Mg	13.8	274.3	1223.7	749.2	402.2	1443.3	515.7
Al	54.4	456.3	4087.6	4599.8	3232.8	1363.8	2027.2
P	1.2	1.7	12.3	233.3	65.2	15.6	6.7
K	11.8	44.2	120.9	7.0E-01	4.2	52.9	122.8
Ca	35.8	11176.1	2444.6	3933.7	1451.7	6679.0	4228.5
Ti	2.8E-02	2.8E-01	5.3E-02	2.0E-01	6.4E-02	2.8E-02	2.1E-02
V	2.7E-02	4.7E-03	11.4	1.3	1.1	1.7E-01	4.3E-01
Cr	1.2E-02	1.2E-01	2.2	8.0E-01	4.4E-01	9.8E-02	4.3E-02
Mn	1.9E-01	11.8	181.2	30.0	6.6	52.3	17.0
Fe^{2+}	BDL	224.8	7696.6	5885.2	3285.8	1928.9	1073.8
S.D.(Fe^{2+})	---	5.8	328.2	67.0	82.3	39.4	65.0
Fe^{3+}	11.9	504.2	5608.5	5456.3	2619.4	50.2	413.9
Co	2.8E-03	4.0E-01	7.7	6.5	3.2	7.7	4.4
Ni	8.7E-03	3.8E-01	12.6	8.3	5.5	4.8	3.1
Cu	4.3E-02	1.9	14.9	11.8	4.4	5.5	10.1
Zn	9.6E-02	2.8	84.8	5.8	4.5	6.7	4.4
As	BDL	BDL	3.1E-01	1.4	2.5E-01	5.1E-02	8.1E-02
Se	BDL	4.4E-02	6.0E-01	8.0E-01	1.5E-01	1.7E-01	6.8E-01
Rb	5.9E-03	6.4E-02	0.1	3.8E-02	3.4E-02	5.9E-02	7.2E-02
Sr	1.5E-01	7.9	16.2	18.0	1.6	10.5	7.4
Zr	---	---	---	---	BDL	2.5E-03	---
Mo	2.5E-03	2.6E-02	0.0	1.0E-01	1.2E-01	1.0E-01	0.0
Cd	BDL	1.6E-03	2.7E-01	8.0E-03	4.2E-03	2.7E-02	1.6E-02
Cs	2.3E-03	5.8E-03	---	2.1E-02	3.9E-02	3.2E-02	---
Ba	1.3E-02	1.1E-01	2.3E-01	1.6E-02	1.9E-01	2.2E-01	4.8E-01
Hf	BDL	BDL	---	BDL	BDL	BDL	---
W	BDL	BDL	---	1.6E-03	1.3E-02	BDL	---
Ag	BDL	BDL	BDL	BDL	---	---	---
Hg	BDL	BDL	---	BDL	9.0E-03	1.1E-03	---
Pb	BDL	BDL	---	BDL	1.1E-01	1.1E-01	---
U	BDL	BDL	---	2.3E-03	4.1E-03	8.4E-03	---
pH	6.9	4.2	2.7	3.0	3.1	3.6	3.6
Std. Dev.	0.0	0.0	0.0	0.1	0.1	0.0	0.1
Eh (mV)	349.7	443.5	584.4	611.4	550.5	451.5	479.1
Std. Dev.	10.1	1.5	0.7	1.3	6.2	9.2	6.4
H_2O_2 (µM)	BDL	31.2	610.8	598.0	187.7	158.7	140.4
Std. Dev.	---	29.7	90.5	25.9	22.2	9.7	10.7

Table E1. Continued.

Element	P8	P9	P10	P11	P12	P13	P14	P15
Na	57.9	64.4	181.9	366.6	137.5	337.2	380.5	159.0
Mg	1270.3	1357.4	1599.3	1319.3	1191.5	149.6	68.4	89.7
Al	1993.9	637.2	584.3	224.4	441.1	22.9	13.2	1.9
P	6.2	2.3	2.0	1.1E-01	1.0	4.6	0.0E+00	6.4E-01
K	3.5	6.4	32.3	77.8	159.4	132.1	118.5	25.2
Ca	4960.7	3904.8	4633.5	4262.3	3675.0	637.4	204.4	661.4
Ti	4.7E-02	2.9E-02	2.7E-02	2.2E-02	1.2E-02	5.9E-03	1.2E-03	6.3E-03
V	4.9E-01	1.5E-01	3.6E-03	2.8E-02	2.7E-02	6.7E-03	2.1E-03	1.2E-02
Cr	1.4E-01	7.4E-02	5.2E-02	1.7E-02	4.6E-02	2.0E-02	0.0E+00	4.3E-03
Mn	37.5	26.2	28.7	21.6	28.8	7.8	2.4	7.4E-02
Fe^{2+}	1443.8	1594.3	1202.2	640.3	1429.2	225.2	30.4	BDL
S.D.(Fe^{2+})	39.7	42.4	43.0	12.0	39.3	6.7	1.9	---
Fe^{3+}	44.2	50.3	118.4	12.5	14.9	0.0E+00	24.1	1.0E-01
Co	6.7	2.9	2.8	5.6	2.4	7.6E-01	1.2E-01	1.1E-03
Ni	5.8	2.5	2.3	2.1	1.8	1.7	1.6E-01	1.0E-02
Cu	5.3	2.6	2.5	1.7	1.8	5.8E-01	1.9	9.3E-02
Zn	5.4	2.4	1.7	1.3	11.3	3.1	1.1	5.6E-02
As	5.3E-02	4.5E-02	2.4E-02	1.5E-02	2.5E-02	3.3E-02	1.8E-03	1.2E-03
Se	3.5E-01	1.1E-01	1.0E-01	2.4E-02	6.2E-02	2.1E-03	2.3E-02	1.1E-02
Rb	1.9E-02	2.5E-02	5.1E-02	7.0E-02	1.1E-01	1.0E-01	1.5E-01	1.6E-03
Sr	11.2	11.0	14.4	14.0	11.0	1.7	5.5E-01	2.0
Zr	4.3E-03	BDL	BDL	BDL	BDL	1.3E-03	---	BDL
Mo	1.7E-02	1.7E-02	1.4E-02	2.5E-03	3.7E-03	1.0E-02	2.7E-03	1.2E-02
Cd	1.3E-02	9.2E-03	5.0E-03	2.5E-03	1.0E-02	8.0E-03	1.6E-03	BDL
Cs	1.7E-02	1.7E-02	1.6E-02	1.6E-02	1.6E-02	1.7E-02	---	BDL
Ba	1.5E-01	1.2E-01	2.4E-01	3.6E-01	4.3E-01	3.2E-01	4.4E-01	5.5E-02
Hf	1.1E-03	BDL	BDL	BDL	BDL	BDL	---	BDL
W	BDL	BDL	BDL	2.9E-03	BDL	BDL	---	BDL
Ag	---	---	---	---	---	---	---	---
Hg	2.4E-03	1.8E-03	1.4E-03	1.3E-03	2.5E-03	2.2E-03	---	BDL
Pb	5.8E-02	5.8E-02	6.2E-02	1.2E-01	5.5E-01	8.5E-02	---	2.5E-02
U	1.4E-02	6.9E-03	5.0E-03	4.0E-03	5.6E-03	1.3E-03	---	BDL
pH	3.8	4.0	4.2	4.3	4.2	4.9	4.6	6.9
Std. Dev.	0.1	0.1	0.1	0.0	0.1	0.1	0.1	0.0
Eh (mV)	477.4	447.2	434.4	409.3	428.1	349.8	400.0	391.8
Std. Dev.	1.8	2.6	3.5	2.9	4.9	1.3	2.6	17.8
H_2O_2 (µM)	191.3	156.5	66.5	18.2	21.4	BDL	24.5	BDL
Std. Dev.	24.3	4.6	6.8	1.4	2.3	---	1.0	---

Table E2. ICP-MS elemental analysis of mineral leachates (100 mg/ml) from the Sulfur Mine and pH, Eh and H_2O_2 measurements from 100 mg/ml mineral suspensions. All element values are reported at micro-molar (µM) concentrations. Elements < 1nM are listed as below detection limit (BDL). The standard deviation for ICP-MS analysis was < 7.0 %. Ferrous iron concentrations were measured using 1, 10 phenanthroline, with standard deviation values reported as S.D. (Fe^{2+}).

Element	S1	S2	S3	S4	S5
Na	148.8	235.8	56.0	239.9	124.3
Mg	1419.0	389.1	2951.5	660.1	1203.2
Al	0.7	1030.8	9441.6	8208.0	12975.8
P	0.8	13.8	176.7	96.1	1.2
K	11.8	84.7	1.0	202.4	36.2
Ca	35.8	2123.5	4554.1	523.1	1153.2
Ti	1.2E-02	3.6E-02	9.9E-02	3.3E-01	1.5E-01
V	2.6E-03	4.0E-01	8.6	7.8	22.3
Cr	1.2E-03	7.8E-02	3.4	5.5	6.5
Mn	1.9E-01	18.4	351.3	120.2	188.4
Fe^{2+}	BDL	1205.5	12364.2	18137.5	18093.8
S.D.(Fe^{2+})	---	12.9	554.9	235.7	223.5
Fe^{3+}	5.8E-01	150.8	10669.1	17343.3	7557.1
Co	1.3E-02	2.6	9.7	21.2	14.7
Ni	6.9E-02	2.2	10.3	30.1	20.3
Cu	2.9E-01	2.8	23.3	35.2	2.8
Zn	6.4E-02	3.7	11.2	36.7	24.6
As	BDL	9.4E-02	1.4	1.9	2.6E-01
Se	3.8E-02	4.2E-01	8.3E-01	9.3E-01	5.3E-01
Rb	2.0E-02	8.2E-02	0.0	2.4E-01	8.6E-02
Sr	5.8	4.0	16.3	6.2	6.6
Zr	BDL	---	0.0	---	4.7E-03
Mo	5.1E-03	1.7E-02	0.1	1.3E-01	1.9E-02
Cd	BDL	1.1E-02	8.6E-02	1.6E-01	3.5E-01
Cs	BDL	---	4.0E-03	---	4.7E-03
Ba	2.3E-01	4.8E-01	1.1E-01	3.8E-01	8.2E-02
Hf	BDL	---	BDL	---	BDL
W	BDL	---	4.3E-03	---	5.7E-03
Ag	---	---	---	---	---
Hg	1.4E-0.3	---	1.2E-03	---	2.0E-03
Pb	3.8E-02	---	8.6E-02	---	1.2E-01
U	BDL	---	3.3E-02	---	4.0E-02
pH	6.9	3.7	2.5	2.1	2.3
Std. Dev.	0.0	0.1	0.1	0.1	0.0
Eh (mV)	398.5	450.7	630.5	724.0	713.9
Std. Dev.	11.8	4.0	0.5	0.4	4.8
H_2O_2 (µM)	3.7	115.6	1490.6	1531.1	1597.3
Std. Dev.	1.1	10.6	13.6	58.8	104.5

Table E2. Continued.

Element	S6	S7	S8	S9	S10
Na	193.3	207.4	27.5	101.7	335.3
Mg	1114.1	917.1	1944.1	169.8	4476.9
Al	3646.9	14821.1	8981.9	496.9	474.3
P	19.5	7.0	3.0	1.5	1.1
K	65.2	399.9	3.3	8.7	78.3
Ca	1734.5	385.4	3190.7	201.2	7695.5
Ti	5.5E-02	2.1E-01	1.0E-01	9.8E-03	4.0E-03
V	17.2	11.7	4.6	8.7E-03	1.3E-03
Cr	4.4	4.0	1.5	3.9E-02	2.8E-02
Mn	239.7	153.6445	323.6	5.4	292.3
Fe^{2+}	8283.9	18633.9	12847.2	BDL	420.7
S.D.(Fe^{2+})	161.3	341.7	353.4	---	10.1
Fe^{3+}	4136.0	21407.2	3363.1	1.1	BDL
Co	7.5	14.0	7.4	6.2	19.5
Ni	13.1	17.3	10.0	0.9	13.8
Cu	13.0	22.0	13.1	3.7	10.5
Zn	31.6	40.7	5.4	0.9	8.8
As	2.2E-01	24.3	1.6E-01	8.6E-03	5.1E-02
Se	5.3E-01	2.8E-01	3.4E-01	1.0E-01	5.5E-01
Rb	3.7E-02	7.9E-01	3.1E-02	2.6E-02	5.7E-02
Sr	12.3	7.1	46.5	0.9	15.6
Zr	---	---	3.3E-03	BDL	BDL
Mo	3.2E-02	0.2	8.2E-03	BDL	2.7E-03
Cd	4.4E-01	1.7E-01	1.2E-01	2.1E-03	9.6E-02
Cs	---	8.3E-02	1.5E-03	BDL	1.4E-03
Ba	1.3E-01	3.9E-01	1.6E-01	7.6E-02	3.3E-01
Hf	---	BDL	BDL	BDL	BDL
W	---	BDL	4.8E-03	3.9E-03	2.3E-03
Ag	---	---	---	---	---
Hg	---	---	1.3E-03	BDL	BDL
Pb	---	---	1.6E-01	3.9E-02	4.6E-02
U	---	---	7.0E-02	2.6E-03	5.1E-03
pH	2.7	2.2	2.6	5.1	6.2
Std. Dev.	0.1	0.0	0.0	0.1	0.1
Eh (mV)	594.6	757.6	575.4	404.2	432.6
Std. Dev.	15.0	0.4	0.7	1.0	3.7
H_2O_2 (µM)	868.9	1525.8	1503.4	BDL	7.9
Std. Dev.	63.3	94.0	1.5	---	2.5

Table E3. ICP-MS elemental analysis of mineral leachates (100 mg/ml) from Foster Creek and pH, Eh and H_2O_2 measurements from 100 mg/ml mineral suspensions. All element values are reported at micro-molar (µM) concentrations. Elements < 1nM are listed as below detection limit (BDL). The standard deviation for ICP-MS analysis was < 7.0 %. Ferrous iron concentrations were measured using 1, 10 phenanthroline, with standard deviation values reported as S.D. (Fe^{2+}).

Element	F1	F2	F3	F4	F5	F6	F7	F8	F9
Na	190.2	---	108.5	286.1	190.7	144.5	38.4	62.8	76.2
Mg	155.2	---	159.4	45.1	1735.4	1900.6	9.4	2509.3	211.3
Al	1.4	---	6.1E-01	147.0	5.7E-01	3.5E-01	42.1	2065.5	745.7
P	5.8	---	2.0	9.8	1.3E-01	1.1	2.0	24.1	8.7
K	96.0	---	62.0	29.3	50.3	116.2	44.2	1.8	294.5
Ca	1176.2	---	1261.1	45.0	2242.2	4230.0	57.3	4612.0	667.7
Ti	6.1E-03	---	5.7E-03	2.1	BDL	3.1E-03	2.7E-02	2.2E-02	3.2E-02
V	7.6E-03	---	9.1E-03	7.5E-02	BDL	BDL	6.8E-03	1.6E-01	3.1E-01
Cr	8.3E-03	---	1.6E-03	6.2E-03	BDL	1.3E-03	2.0E-03	1.3E-01	2.0E-02
Mn	2.0	---	1.2	4.9E-01	16.1	43.7	3.7E-02	71.3	9.3
Fe^{2+}	30.4	---	BDL	57.3	BDL	BDL	BDL	2374.9	2547.8
S.D.(Fe^{2+})	4.0	---	---	3.8	---	---	---	41.9	54.4
Fe^{3+}	1.5E-01	---	6.3E-02	5.5E-01	1.5E-01	7.0E-02	2.7	2010.5	968.6
Co	1.1E-02	---	2.6E-02	21.2	7.4E-02	3.7E-02	BDL	4.3	1.4
Ni	9.2E-02	---	2.9E-02	30.1	8.0E-02	8.4E-02	BDL	4.8	0.7
Cu	2.3E-01	---	1.6E-01	35.2	9.5E-03	7.8E-02	7.8E-02	6.1	8.7
Zn	1.9	---	5.3E-02	36.7	2.5E-01	6.5E-02	4.1E-02	4.6	3.4
As	6.4E-03	---	4.3E-03	1.9	BDL	BDL	3.2E-02	1.0E-01	1.4E-01
Se	7.9E-03	---	BDL	9.3E-01	5.3E-02	1.6E-02	1.6E-03	5.6E-01	4.6E-01
Rb	8.7E-03	---	1.4E-02	2.4E-01	7.4E-03	4.9E-02	9.5E-03	9.8E-03	1.7E-01
Sr	3.3	---	3.8E-02	6.2	4.1	17.3	0.3	7.7	---
Zr	1.0E-03	---	4.0E-02	---	---	0.0	0.0	BDL	
Mo	1.3E-02	---	7.5E-03	1.3E-01	1.7E-02	4.0E-03	0.0	9.6E-03	1.7E-01
Cd	2.2E-03	---	BDL	1.6E-01	BDL	BDL	BDL	9.6E-03	1.6E-02
Cs	3.0E-03	---	BDL	---	---	0.0	BDL	7.0E-03	---
Ba	3.5E-01	---	3.0E-02	3.8E-01	1.2E-01	2.8E-01	1.2E-01	7.6E-02	7.7E-01
Hf	BDL	---	BDL	---	---	0.0	BDL	BDL	---
W	BDL	---	BDL	---	---	0.0	BDL	BDL	---
Ag	---	---	---	---	---	---	---	---	---
Hg	BDL	---	2.7E-03	---	---	4.0E-03	BDL	1.5E-03	---
Pb	3.17E-02	---	2.4E-02	---	---	2.2E-02	2.2E-02	4.6E-02	---
U	BDL	---	BDL	---	---	BDL	BDL	4.1E-03	---
pH	7.0	6.2	7.1	7.5	7.2	6.9	6.3	3.3	3.5
Std. Dev.	0.0	0.0	0.0	0.1	0.1	0.0	0.1	0.1	0.1
Eh (mV)	368.4	340.1	363.2	317.6	394.8	322.2	385.8	520.9	451.0
Std. Dev.	1.6	8.9	1.8	7.0	25.2	4.4	24.3	3.3	4.3
H_2O_2 (µM)	BDL	BDL	BDL	BDL	BDL	BDL	BDL	275.8	286.0
Std. Dev.	---	---	---	---	---	---	---	38.8	4.6

Table E4. ICP-MS elemental analysis of mineral leachates (100 mg/ml) from the Road Cut clay site and pH, Eh and H_2O_2 measurements from 100 mg/ml mineral suspensions. All element values are reported at micro-molar (µM) concentrations. Elements < 1nM are listed as below detection limit (BDL). The standard deviation for ICP-MS analysis was < 7.0 %. Ferrous iron concentrations were measured using 1, 10 phenanthroline with standard deviation values reported as S.D. (Fe^{2+}).

Element	C1	C2	C3	C4	C5	C6	C7	C8	C 9
Na	212.7	1397.2	53.0	45.6	66.8	---	56.3	---	111.0
Mg	45.9	162.0	497.5	384.2	20.4	---	6.6	---	390.5
Al	2.6	3.3	32.9	503.9	10.9	---	6.9	---	63.4
P	1.2	1.6	0.7	4.2E-01	2.7	---	0.1	---	1.3
K	186.9	247.8	374.7	424.4	12.6	---	170.3	---	90.5
Ca	598.0	193.5	4775.4	4209.7	61.6	---	281.2	---	1693.1
Ti	6.0E-03	4.2E-03	1.1E-02	0.0	7.0E-03	---	5.9E-03	---	4.8E-03
V	7.3E-03	BDL	BDL	BDL	BDL	---	1.7E-01	---	2.2E-03
Cr	2.2E-03	3.1E-03	3.0E-03	1.7E-03	8.0E-03	---	2.1E-03	---	1.3E-02
Mn	2.1E-01	1.8	12.8	14.5	0.5	---	2.1E-02	---	22.4
Fe^{2+}	BDL	BDL	BDL	215.3	45.6	---	BDL	---	101.9
S.D.(Fe^{2+})	---	---	---	14.7	7.0	---	---	---	5.2
Fe^{3+}	2.5E-01	1.1E-2	6.3E-02	99.1	53.4	---	3.2E-01	---	146.9
Co	2.3E-03	1.2	34.1	2.7	48.7	---	1.3E-03	---	5.1E-01
Ni	9.7E-03	3.6E-02	1.0	7.9E-01	3.8E-02	---	3.4E-03	---	4.8E-01
Cu	1.0E-01	3.2E-01	6.7E-01	6.3E-01	1.6E-01	---	3.5E-01	---	1.1
Zn	1.2E-01	5.9E-01	5.3E+01	3.8	5.6E-01	---	3.3E-02	---	2.9
As	1.7E-02	1.8E-03	1.2E-01	1.7E-01	1.2	---	7.5E-03	---	8.8E-02
Se	1.1E-03	8.2E-03	2.9E-02	2.5E-02	2.0E-02	---	BDL	---	3.6E-02
Rb	2.3E-02	3.1E-02	9.4E-02	8.9E-02	9.8E-03	---	1.3E-02	---	3.0E-02
Sr	2.1	8.5E-01	3.2E+01	35.9	6.4E-03	---	1.5	---	8.6
Zr	BDL	BDL	BDL	BDL	3.0E-01	---	BDL	---	BDL
Mo	2.1E-02	BDL	4.1E-03	2.9E-03	BDL	---	2.2E-02	---	BDL
Cd	BDL	BDL	9.6E-03	1.0E-02	2.1E-03	---	BDL	---	1.1E-02
Cs	BDL	BDL	1.0E-03	BDL	2.1E-03	---	BDL	---	1.7E-03
Ba	5.3E-01	1.6E-01	4.9E-01	4.8E-01	2.0E-03	---	3.6E-02	---	3.2E-01
Hf	BDL	BDL	4.3E-03	BDL	2.6E-01	---	BDL	---	BDL
W	3.5E-01	4.4E-03	BDL	8.4E-02	5.3E-03	---	6.0	---	2.2E-02
Ag	---	---	---	---	---	---	---	---	---
Hg	1.2E-02	1.3E-03	BDL	3.2E-03	2.0E-03	---	1.9E-01	---	1.0E-03
Pb	2.6E-02	4.1E-02	2.2E-01	1.4E-01	4.6E-02	---	4.4E-02	---	3.8E-02
U	BDL	BDL	3.9E-03	3.0E-03	BDL	---	BDL	---	BDL
pH	6.8	7.5	5.3	4.6	5.9	6.6	7.3	6.9	5.2
Std. Dev.	0.0	0.1	0.0	0.1	0.1	0.0	0.1	0.0	0.1
Eh (mV)	375.3	356.6	367.5	448.3	375.0	375.5	378.1	365.7	394.2
Std. Dev.	7.1	5.1	2.1	6.7	5.7	27.8	0.4	3.2	9.0
H_2O_2 (µM)	BDL	BDL	BDL	217.5	BDL	---	BDL	---	74.7
Std. Dev.	---	---	---	0.9	---	---	---	---	9.1

APPENDIX F

EQUILIBRIUM CONSTANTS

Table F1. Reactions and equilibrium constants (log K) used for calculating pH-Eh speciation diagrams.

Reaction	logK
$Fe^{2+} \leftrightarrows e^- + Fe^{3+}_{(aq)}$	13.02
$Fe^{2+} + SO_4^{2-} \leftrightarrows e^- + FeSO_4^{+}{}_{(aq)}$	8.98
$Fe^{2+} + 2H_2O \leftrightarrows e^- + Fe^{3+} + FeOOH_{(solid)}$	14.02
$Fe^{2+} + 2HS^- \leftrightarrows 2H^+ + 2e^- + FeS_{2(solid)}$	-18.48
$Fe^{2+} + HS^- \leftrightarrows H^+ + FeS_{(solid)}$	-4.65
$HS^- + 4H_2O \leftrightarrows 9H^+ + 8e^- + SO_4^{2-}{}_{(aq)}$	33.69
$HS^- + 4H_2O \leftrightarrows 8H^+ + 8e^- + HSO_4^{-}{}_{(aq)}$	31.71
$HS^- \leftrightarrows H^+ + 2e^- + S_{(solid)}$	-2.145
$H^+ + HS^- \leftrightarrows H_2S_{(gas)}$	-6.99
$Al^{3+} + SO_4^{2-} \leftrightarrows AlSO_4^{+}{}_{(aq)}$	3.5
$Al^{3+} + SO_4^{2-} + H_2O \leftrightarrows H^+ + AlOHSO_{4(solid)}$	3.23
$Al^{3+} + 3H_2O \leftrightarrows 3H^+ + Al(OH)_{3\ (solid)}$	-8.11

APPENDIX G

MIC AND MBC ELEMENTAL ANALYSIS

Table G1. Elemental analyses of mineral leachates (sample P4). All values are reported at micro-molar (µM) concentrations. Elements <1nM are listed as below detection limit (BDL).

Element	3 mg/ml	20 mg/ml	75 mg/ml	100 mg/ml
Na	6.7	7.7	23.6	34.2
Mg	22.2	137.7	485.8	749.2
Al	86.6	750.5	2884.4	4599.8
P	0.8	12.4	122.6	233.3
K	1.9	1.2	0.3	0.7
Ca	113.3	733.1	2413.4	3933.7
Ti	2.4E-03	1.0E-02	0.1	0.2
V	4.8E-03	0.2	0.8	1.3
Cr	1.5E-02	0.1	0.5	0.8
Mn	0.8	5.5	19.5	30.0
Fe^{2+}	191.7	1452.1	4693.4	5885.2
Fe^{3+}	51.7	618.0	3625.3	5456.3
Co	0.2	1.2	4.2	6.5
Ni	0.2	1.6	5.4	8.3
Cu	0.4	2.2	7.6	11.8
Zn	0.2	1.0	3.7	5.8
As	3.8E-03	0.1	0.7	1.4
Se	1.7E-02	0.2	0.5	0.8
Rb	1.1E-02	1.9E-02	0.1	3.8E-02
Sr	0.6	3.8	11.9	18.0
Zr	1.3E-03	1.7E-03	3.3E-03	5.0E-03
Mo	5.6E-03	2.0E-02	0.1	0.1
Cd	BDL	2.2E-03	5.5E-03	8.0E-03
Cs	4.7E-03	9.1E-03	2.6E-02	2.1E-02
Ba	0.1	2.9E-02	2.0E-02	1.6E-02
Hf	BDL	BDL	BDL	BDL
W	3.7E-03	2.0E-03	1.9E-03	1.6E-03
Ag	BDL	BDL	BDL	BDL
Hg	BDL	BDL	BDL	BDL
Pb	BDL	BDL	BDL	BDL
U	BDL	BDL	1.5E-03	2.3E-03

Note: relative standard deviations were <7.0 %

Table G2. Leachate and synthetic metal mixture MIC, MBC and pH values for *E. coli* measured in MSA and LB media. pH was measured directly after addition of leachates or metal mixtures to bacteria in media. Added metal content was determined along with soluble metal content in media alone after 1h

			MSA-Media								
			Added (mM)			Soluble (mM)			% Soluble		
Leachate	MIC/MBC	pH	Fe^{2+}	Fe^{3+}	Al^{3+}	Fe^{2+}	Fe^{3+}	Al^{3+}	Fe^{2+}	Fe^{3+}	Al^{3+}
3 mg/ml	MIC	4.9	0.162	0.082	0.084	0.137	0.016	0.038	84.6	19.5	45.2
20mg/ml	MBC	3.4	1.45	0.62	0.79	1.42	0.074	0.65	97.9	11.9	82.3
Metal Mixture	MIC	5.1	0.160	0.063	0.087	0.124	BDL	0.023	77.5	0.0	26.4
Metal Mixture	MBC	3.9	1.10	0.55	0.78	0.93	BDL	0.43	84.5	0.0	55.1
			LB-Media								
20 mg/ml	MIC	4.6	1.45	0.62	0.79	1.34	0.012	0.084	92.4	1.9	10.6
75 mg/ml	MBC	3.5	4.70	3.63	3.05	2.23	0.063	1.74	47.5	1.7	57.0
Metal Mixture	MIC	5.0	1.92	1.25	1.38	1.60	0.055	0.11	83.3	4.4	8.0
Metal Mixture	MBC	3.6	3.91	2.62	3.22	3.82	0.155	0.67	97.6	5.9	20.8

Note: relative standard deviation values for pH and elemental analysis were < 1.0 % and 10.0 %

Table G3. Individual metal MIC, MBC and pH values for *E. coli* measured in MSA and LB media. pH was measured directly after addition of metals to bacteria in media. Added metal content was determined along with soluble metal content in media alone after 1h.

		MSA-Media				LB-Media			
	MIC/MBC	pH	Added	Soluble	% Soluble	pH	Added	Soluble	% Soluble
Fe^{2+}	MIC	5.9	2	1.7	85.0	5.9	5	1.8	36.0
	MBC	5.6	8	7.4	92.5	5.7	8	3.8	47.5
Fe^{3+}	MIC	4.3	0.5	0.01	2.0	4.5	3	0.15	5.0
	MBC	3.5	1	0.12	12.0	3.6	5	0.39	7.8
Al^{3+}	MIC	4.7	0.5	0.22	44.0	4.7	3	1.5	50.0
	MBC	3.9	7	3.3	47.1	3.8	11	9.8	89.0
Ca^{2+}	MIC	6.4	500	---	---	6.6	500	---	---
	MBC	6.1	1000	---	---	6.4	1500	---	---

Note: relative standard deviations for pH were <1%; elemental analysis <8.0%.

APPENDIX H

STXM MAPS

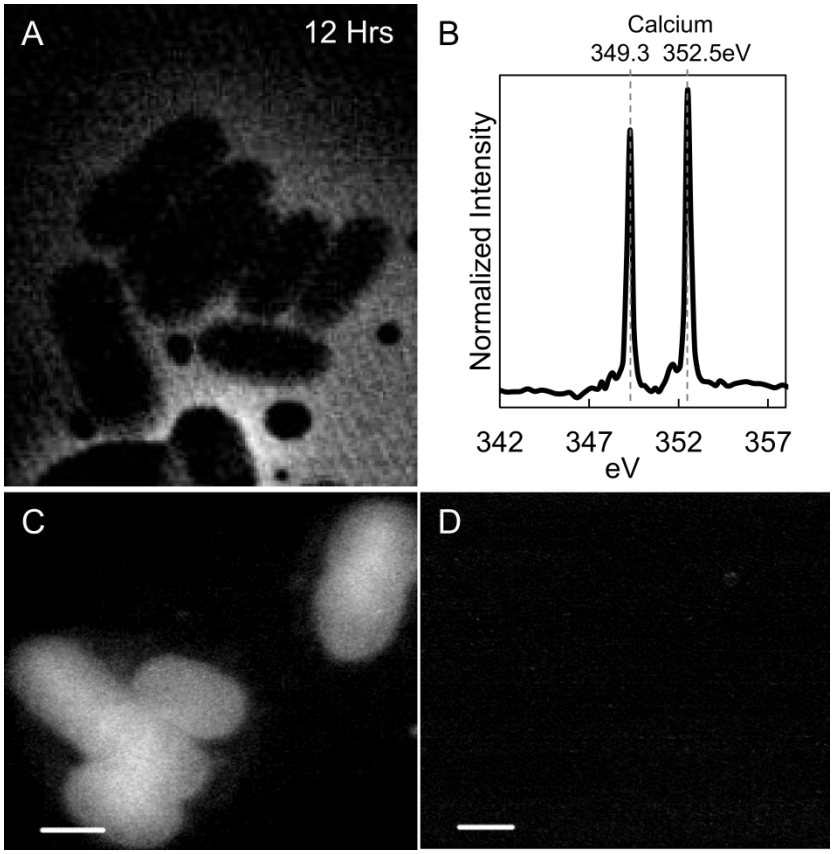

STXM Ca and Fe maps. (A) STXM calcium maps of *E. coli* reacting with a 100mg/ml mineral suspension showing the majority of Ca present in the leachates remains in solution and not adsorbed to bacterial cells. (B) Corresponding Ca NEXAFS spectrum. (C) STXM protein maps (280-288.2 eV) of *E. coli* cells reacted with a 100mg/ml mineral suspension (12h) and washed with Ox-EDTA to remove adsorbed metals. (D) Fe maps (700-708 eV) of the same cells showing no signal. Scale bars represent 0.5µm.